UNIVERSITÀ DEGLI STUDI DI MILANO

EX SITU DOPING OF SILICON NANOSTRUCTURES

Arduca Elisa,
PhD Thesis

Coordinator: Prof. Marco Bersanelli

Supervisor: Prof.sa Cristina Lenardi

Co-supervisor: Dr. Michele Perego

A.A. 2016-2017

What I like about experience is that it is such an honest thing. You may take any number of wrong turnings; but keep your eyes open and you will not be allowed to go very far before the warning signs appear. You may have deceived yourself, but experience is not trying to deceive you. The universe rings true wherever you fairly test it

C. S. Lewis

To my mother, my husband and my sons

Table of Contents

Synopsis

Over the last decades semiconducting nanostructures with reduced dimensionality have attracted considerable scientific interest due to their peculiar properties, arising from the interplay between quantum confinement and surface related effects. In fact, if at least one of the dimensions of these nanostructures is smaller than twice the Bohr radius of the exciton in the bulk material, quantum confinement occurs, causing a different electronic and optical behavior of the nanostructures compared to bulk materials. Moreover, the reduced size of these nanostructures induces a remarkable increase of the surface area to volume ratio (S/V). Consequently surface related defects may significantly alter the electronic behavior of these nanostructures [1]. Silicon nanostructures are particularly appealing for application in several fields like microelectronics, optoelectronics, photovoltaics, plasmonics and thermoelectric [2]–[5]. During the last century, impurity doping of Si was used to tailor the electronic properties of bulk silicon, employing p/n junctions as common building blocks of Si-based electronic devices [6]. The exploitation of Si nanostructures as basic elements for the fabrication of complex optoelectronic and microelectronic devices requires the capability to effectively control their electronic properties by means of doping as in the case of bulk semiconductors.

In this regard, Silicon Nanocrystals (Si NCs) represent a paradigmatic system because the attainable results are in the extreme case of nanoscaling, from bulk to 0D system. Therefore they are extremely useful for the understanding of other silicon systems with reduced dimensionality like nanowires, fins or nanosheet [7][8][9][10]. Synthesis of Si NCs, both embedded in dielectric matrix and freestanding, has been studied achieving excellent results [11]. In this regards, the problems of impurity incorporation and doping of Si NCs is actually very far from being understood and some important issues still need to be clarified from the experimental and theoretical point of view. Actually both p-type (B) and n-type (P, As) impurities have been successfully introduced in very small Si NCs by means of different experimental approaches [12][13][14]. Nevertheless very few data are available about the thermodynamic stability of the impurity atoms in the Si NCs [15]. A clear understanding of nanoscale doping processes at nanoscale is not yet available. The key questions are: is dopant incorporation at the nanoscale allowed by thermodynamics stability, or is it a metastable condition that can be achieved only by kinetic or non-equilibrium effect [5,13]? Can we

measure the energy barriers describing atomic transport, i.e. the atomistic parameters provided also by calculations, thus linking experiments and theory?

Usually, doping of Si NCs in a SiO_2 matrix was performed by introducing the dopant in the matrix before NCs formation and subsequently inducing dopant incorporation and Si NCs formation simultaneously.[58][70][72][128][129], [186], [187] This approach indicated that inclusion of electrically active impurities in Si NCs is kinetically possible [18], [21]–[23]. However, these results do not provide any information on the energetics of atomic transport at the NCs since the experiments were conducted out of equilibrium condition. Moreover, the presence of impurities during Si NCs synthesis significantly affects the growth kinetics leading to size variations of the resulting nanoparticles [23]. These effects partially account for discrepancies in the experimental evidences reported in the literature [14], [23]–[27]. From a theoretical point of view, seminal works by Chelikowsky's group showed evidences of B and P segregation at the surface of H-terminated Si NCs and proposed the occurrence of a self-purification mechanism in NCs with d < 2 nm.[28]–[30] Recently several authors demonstrated that oxygen terminated Si NCs design a different picture: if the SiO_2 matrix is taken into account, incorporated P has a minimum of binding energy in the inner part or in the sub-interface region of the Si nanoclusters, suggesting the possibility to stably incorporate impurities within Si NCs[31]–[34].

In this thesis work, we developed an alternative experimental approach to tackle these fundamental issues. The main idea behind our approach is the decoupling of Si NCs synthesis from the dopant incorporation. The incorporation of Phosphorous (P) atoms is promoted in Si NCs after their formation, by delivering a controlled amount of dopant atoms from a spatially separated diffusion source. In this way, the energetics of trapping/detrapping of P in the NCs are measured at equilibrium and modelled as a function of the annealing temperature and time, avoiding kinetic effects due to NCs formation.

The present manuscript is organized in three chapters according to the following scheme:

Chapter 1, *Introduction*: in this chapter, a review of literature results about doping of Si NCs is reported. The chapter is organized in two main sections: the first section focuses on the problem of intentional introduction of impurities into Si NCs comparing the different theoretical and experimental results available in the literature. The second section of the chapter faces the problem of the modulation of electrical properties in doped Si NCs, trying to correlate the experimental data on impurity incorporation with effective doping of the silicon nanostructures.

Chapter 2, *Experimental*: In this chapter, all the experimental techniques and processes that were used to perform this research activity are described in details. This chapter is organized in two main section, the first section focuses on the processes that were used for the synthesis of the Si NCs and of the P δ-layers that were used as a source of impurity dopants. The second part describes the analytical techniques used for the characterization of the samples, providing some fundamental information about their working principles in view of their application to our specific problems.

Chapter 3, *Result and Discussion*: In this chapter all the results achieved during this thesis work are presented in an organic and comprehensive picture. In the first section, three different approaches that allow the formation of P δ-layer in SiO_2 are presented. In the second part, a

study is presented about the evolution of structural characteristics of a single plane of Si NCs embedded in SiO_2. Structural parameters are determined by transmission electron microscopy (TEM) and atom probe tomography (APT) showing an excellent control on the size and areal density by properly tuning processing parameters during the synthesis. In the third section, we focused on P doping of Si NCs embedded in SiO_2. The experimental results are interpreted on the basis of a model describing the trapping-detrapping process. An interesting and original picture of the energetics of P atom impurities in Si NCs is provided.

The review of literature and the experimental results were the subject of several publications on international peer review journals. Here is the list of the papers I have co-authored during my PhD activities:

- Doping of silicon nanocrystals, *Material Science in Semiconductor Processing*, (2016) IN PRESS - ACCEPTED FOR PUBBLICATION
- Modeling of phosphorus diffusion in silicon oxide and incorporation in silicon nanocrystals, *Journal of Materials Chemistry C* 4, 3531-3539 (2016)
- Evolution of shape, size, and areal density of a single plane of Si nanocrystals embedded in SiO2 matrix studied by atom probe tomography, *RSC Adv.*, 6, 3617 (2016)
- Synthesis and characterization of P δ-layer in SiO2 by monolayer doping, *Nanotechnology 27*, 075606 (2016)
- Thermodynamic stability of high phosphorus concentration in silicon nanostructures, *Nanoscale*, 7, 14469-14475 (2015)
- Quantification of phosphorus diffusion and incorporation in silicon nanocrystals embedded in silicon oxide, *Surface and Interface Analysis* 46, 393-396 (2014).

1 – Introduction

In the last decades silicon nanocrystals (Si NCs), i.e. Silicon particles having diameter (d) smaller than 100 nm and composed of atoms in either a single- or poly-crystalline arrangement, were the subject of an intense research activity, owing to their optical and electronic properties [35][36][37]. In Figure 1.0.1 (a) High Resolution TEM (HRTEM) images of a small Si-NC with spherical and non-crystalline morphology is reported [38]. Furthermore, Si NCs represent a paradigmatic system because the attainable results are in the extreme case of nanoscaling, from bulk to 0D system. Therefore they are extremely useful for the understanding of other silicon systems with reduced dimensionality like nanowires, fins or nanosheet [7][8][9][10]. Several studies are available in the literature on the synthesis of Si NCs embedded in dielectric matrix and freestanding Si NCs [11]. Si NCs embedded in dielectric matrix have been synthesized by ion implantation [39][40][41], chemical vapor deposition (CVD) [42][43][44], e-beam deposition [45][46], sputtering [47]–[49] and reactive ion etching [50]. As an example, in Figure 1.0.1 (b) the 3D atom map of a Si NCs layer inside a SiO_2 matrix obtained by APT is reported [51]. Most of these approaches are based on processes that are already employed by microelectronic industries in order to facilitate the integration of these nanostructures in functional microelectronic devices [52][53][54][55]. Conversely freestanding Si NCs have been synthesized by crumbling porous Si [33][34] or by gas-phase approaches, which usually concern the decomposition of a Si precursor by means of thermal heating [58], laser ablation [59] or plasma [60][61][62]. Freestanding Si NCs open the route to the control of surface chemistry and are extremely interesting for the development of thermoelectric devices [63][64], single electron transport device [65][66], solar cell [67], cold electron emitting device [68] and optical device [69].

In the case of very small Si NCs, quantum confinement phenomena play an important role in the definition of their electrical and optical properties. Since Bohr radius of an exciton in silicon is about 5 nm, quantum confinement phenomena have been observed for Si NCs with diameter smaller than 10 nm as widely reported in the literature [17][71][72][73][74]. The most striking effect is related to the progressive increase of the band gap [11][39][18][49][60]. An example is shown in Figure 1.0.1 (c) [18] in which the band gap increases from 1.2 eV (band gap of silicon bulk) up to 1.6 eV when decreasing the average size of the nanostructures. Actually, according to circumstances, the band gap variation induced by quantum confinement effects is in direct competition with band gap modifications

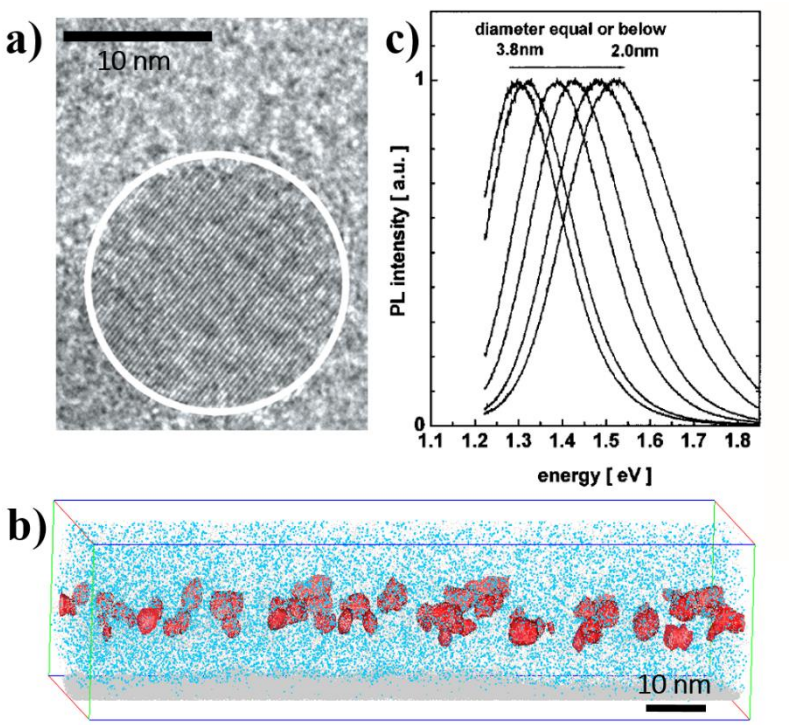

Figure 1.10.1 *a) HRTEM of a small Si-NC with spherical and monocrystalline morphology, reprinted by Dogan et al* [38]; *b) 3D atom map of Si NCs layer inside SiO_2 matrix obtained by APT* [51]; *c) Normalized photoluminescence spectra showing a blue shift correlated with the crystal size, reprinted by Zacharias et al* [75]

determined by the presence of surface induced defects [1], the oxidation degree of the NCs [76] or the different surface passivation [77]. On one hand, surface related effects may appear as localized states within the band gap of Si NCs, further modifying the electronic behavior of Si NCs with respect to bulk silicon. In particular in a recent work Seguini *et al.* [1] investigated the band alignment of Si NCs embedded in a SiO_2 matrix as a function of the average diameter of the Si NCs. Three different regimes were identified by progressively shrinking Si NCs diameter; primarily quantum confinement affects the conduction band that is shifted towards high energy values, then surface effects pin the conduction states, and finally quantum confinement modifies the valence band with a shift towards low energy values [1]. On the other hand Guerra *et al.* [76] demonstrated that the quantum confinement dominates in the H-terminated Si NCs irrespective of their sizes. Conversely in the cases of OH-terminated Si NC and of Si NCs embedded in a SiO_2 matrix the effect of oxidation seems to override the effects of quantum confinement when the diameter decreases below 2 nm. Furthermore Konig et al. [77] demonstrated that for Si NCs core size up to 1330 Si atoms, the nature of the interface bonds can significantly influence the electronic structure of Si NCs, in direct competition with quantum confinement. Finally, it is very important to remind that this band gap evolution can be eventually associated to the transition from indirect to direct band gap

as the Si NCs size decrease. Delerue *et al.* [78] predicted this behavior for Si crystallite sizes lower than 2.5 nm in terms of enhanced efficiency of the radiative recombination rate. Recently Hapala *et al.* [79] introduced a general method which allows reconstruction of electronic band structure of Si NCs from ordinary real-space electronic structure calculations. They concluded that the band-structure concept can be properly applied to silicon nanocrystals with diameter larger than 2 nm, suggesting that for smaller NCs the concept of indirect band gap has no meaning.

In addition to this very complex picture, the problems of impurities incorporation and doping in Si NCs is actually very far from being understood and some important issues still need to be clarified from the experimental and theoretical point of view. Actually both p-type (B) and n-type (P, As) impurities have been successfully introduced in very small Si NCs by means of different experimental approaches [12][13][14]. Nevertheless very few data are available about the thermodynamic stability of the impurity atoms in the Si NCs [15]. This uncertainty is related to the intrinsic limitations of the experimental approaches for the synthesis and for the analysis of these Si NCs, as well as to difficulties in modeling this nanostructured system [15]. Moreover, the effect of impurities on the electronic properties of Si NCs has not been elucidated yet. In particular it is not clear if the incorporation of impurities in Si NCs corresponds to effective doping of the Si NCs, i.e. to the generation of free charge carriers [80][81].

This chapter presents an overview of the recent progress in the field, focusing on the latest results related to doping of Si NCs. I take the major part of this chapter from the review "Doping of Silicon Nanocrystals", which I have co-authored with M. Perego in 2016 for *Material Science in Semiconductor Processing*[82]. This chapter is organized in two main sections: the first section (1.1) focuses on the problem of intentional introduction of impurities into Si NCs comparing the different theoretical and experimental results available in the literature. The second section (1.2) of the chapter faces the problem of the modulation of electrical properties in doped Si NCs, trying to correlate the experimental data on impurity incorporation with effective doping of the silicon nanostructures. In this respect, it is interesting to note that the scientific community working in the field commonly refers to Si NCs with impurities incorporated as "doped Si NCs". From this point of view this corresponds to an improper use of the term "doping", since the incorporation of different species into a nanostructure is fundamental and not experimentally trivial, but it is definitively not sufficient to assume the nanostructures have been effectively doped. In fact, in order to consider the incorporated species as a dopant their electrical activity has to be assessed. Complying with the terminology used by the scientific community, in this thesis I use the term "dopants" to indicate impurity atoms that are incorporated into Si NCs, irrespective of their electrical activation. Similarly, I qualify as "doped" the Si NCs incorporating impurity atoms, focusing on the structural aspects of the problem, assuming the issue of dopant activation is consecutive to the effective incorporation of the impurities into the semiconducting nanostructures.

1.1 Impurity incorporation into Si NCs

Among all the possible dopants for silicon, P and B represent by far the most common choice for n-type and p-type doping respectively, due to their good ionization efficiency at room temperature. Substitutional P and B atoms introduce very shallow energy levels in the band gap of crystalline silicon, resulting in the presence of free charge carriers in the conduction and valence bands of the semiconductor [6]. Indeed, in bulk silicon, P and B atoms are stably

incorporated substituting Si atoms in the crystalline network [6]. Actually in the case of Si NCs the description of the system is much more complex. First, it is necessary to take into account the enormous surface area of Si NCs. The NC surface may act as a trap for the impurity incorporation so that impurities may reside at the surface and not in the Si NCs core. Moreover, it is important to note that notion like "surface" and "core" are tricky to define for very small structures.

According to several theoretical predictions, a change in dopant positioning within Si NCs significantly affects the electrical activity of dopant atoms [34][83][84][85][86][87]. Experimentally it turns out that optical properties of Si NCs are severely affected by dopant incorporation within the Si NCs [13], [21], [83], [88]. Moreover, the optical activity of B and P impurities may also be closely related to dopant location. Actually, it is hard to experimentally determine precise location of dopants inside Si NC. For this reason theoretical efforts focused on detailed modelling of dopant location inside NCs [87][34]. Further difficulties in the understanding of dopant incorporation at the nanoscale arise from the fact that theoretical models usually refer to thermodynamic equilibrium conditions, whereas, in most of the experimental works, impurity incorporation is commonly performed during Si NC formation. [19][21][14][89][90][23][91] This latter circumstance makes difficult to experimentally decouple thermodynamic equilibrium properties from kinetic effects. For this reason, the comparison between theoretical and experimental results is not straightforward. Moreover theoretical investigations were often performed on very small Si NCs, with diameter well below the values that are commonly attainable with standard synthesis techniques [10][92][93]. Over the years the mismatch has been reduced by progressively increasing the size of the Si NCs in the numerical simulations [33][94][86][95]. Finally it is important to highlight that Si NC surface plays an important role in determining kinetics and thermal stability of the incorporated impurities [10][34][33][96]. Consequently, the comparison among theoretical and experimental results has to distinguish between freestanding Si NCs and Si NCs embedded in a dielectric matrix. This section provides an overall picture of the main theoretical and experimental results on the incorporation of dopants in small Si NCs, trying to discriminate the different phenomena associated to dopant incorporation depending on the size of the Si NCs and on their surface characteristics.

1.1.1 Theoretical Description

In the case of freestanding Si NCs with H-terminated surfaces, theoretical studies demonstrated that both B and P atoms thermodynamically prefer to reside at the surface of the silicon nanostructures in order to reduce the stress in the silicon network nearby the substitutional dopant atom and to saturate Si dangling bonds. [33] [86] [85] [97] Consequently, for this specific system, the doping of the nanocrystal core region is expected to be very difficult. [93][98][99][92][71] In particular Pi *et al.* studied the formation energies of substitutional P and B impurity atoms in doped H-terminated Si NCs with diameter d = 2.2 nm. [86] A variety of bonding configurations of B impurity atoms both inside Si NCs and at the NCs surface were investigated. Figure 1.1.1 (a) reports the formation energy of substitutional B atoms as a function of the distance from the center of the Si NC. The thermodynamic stability of the doped Si NCs progressively increases when B moves from the center to the surface of the Si NC [86]. Interestingly in most of the considered configurations a B atom at NCs surface is three-coordinated. As a consequence B atoms trapped at the Si NC surface do not act as acceptors, in agreement with results reported by Polissky *et al.* in the case of Si NCs

inside a porous Si matrix [100]. Similarly P impurity atoms are found to be most likely incorporated at the Si NC surface, as shown in Figure 1.1.1 (b) [85]. All the bonding configurations at NC surface correspond to three-coordinated P atoms, that are electrically inactive [85][97]. Nevertheless, the incorporation of P impurity atoms effectively disables the formation of dangling bonds at the surface, suppressing defect-induced non-radiative events [99]. Similarly, an increase of PL at low B-concentrations was reported by Veettil *et al.* and correlated to dangling bond passivation by boron impurity atoms. [101]

For this specific couple of dopants, the relationship between H-terminated Si NCs size and formation energy of substitutional P and B impurity atoms has been investigated in details. Theoretical predictions indicate that: smaller the Si NCs, larger the energy is needed for the formation of substitutional P and B atoms [93]. On the basis of these results, a sort of self-purification mechanism was proposed for very small Si NCs [30][102][103][28][104]. The basic idea is that, as dopant atoms induce significant stress inside the crystalline core of Si NCs, expelling impurities toward surface results in a reduction of the total energy of the system. In fact, stress induced by dopants at the surface can be accommodated by modification of surface geometry. Chan *et al.* using a real-space first-principles pseudo-potential method investigated impurity incorporation in H-terminated Si NCs with diameter up to 6 nm. They found a critical Si NCs size (~2nm) below which the dopant atom is expected to be ejected toward the surface [104]. The details of this self-purification mechanism have been the subject of an intense scientific debate [105], and a clear understanding of the relative role of kinetics and energetics is still incomplete. The possibility of using intrinsic defects to circumvent this self-purification mechanism and possibly stabilize extrinsic dopant atoms incorporated within small Si NCs was studied as well. [92] For very small B-doped Si NCs composed of 145 Si atoms, it was demonstrated that, if a vacancy can be introduced at the center of Si NCs, a B atom would preferentially stay in close proximity of the vacancy, becoming stable even when incorporated in the Si NCs core [92].

For B and P co-doped Si NCs with H-terminated surfaces, a clear theoretically prediction of dopants location is not available. Apparently dopant atom location depends on the doping level, i.e. on the ratio between number of dopant atoms and number of Si atoms within the Si NCs. Ma *et al.* reported that the incorporation of B and P inside the NC core only occurs for heavily doped NCs, since, at low concentrations, B and P atoms are most likely located at the NC surface. They demonstrated that, in the case of light co-doping of a Si NC with diameter 2.2 nm, B and P atoms are located at the NC surface, where there is the possibility of steric relaxation of dopants. Furthermore the formation energy of light co-doped Si NCs was found to be between those of B and P doped Si NCs, with limited dependence on the distance between dopants [84]. Ossicini *et al.* reported that, in case of very heavy co-doping, B and P atoms tend to occupy the nearest neighboring sites in the subsurface layer of Si NCs. Moreover they found that co-doping is always energetically favored with respect to B and P single-doping [106][94].

It is worth to note that freestanding Si NCs with hydrogen or halogen terminated surfaces were experimentally synthetized by different groups but they quickly oxidize when exposed to air, even at room temperature [107][108]. Moreover, Si NCs embedded in a dielectric matrix were widely investigated for their interesting electronic and optical properties. Their surfaces are characterized by peculiar bonding configurations with the elements of the surrounding matrix. Obviously, the chemical composition of the Si NC surface significantly

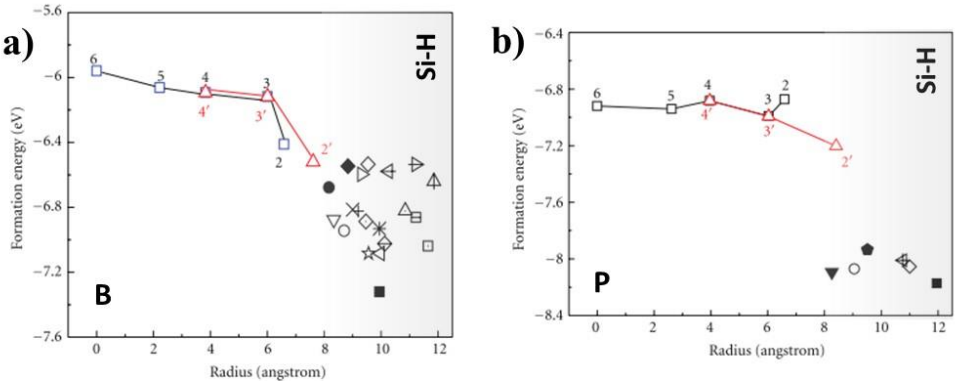

Figure 1.1.1 - a) Formation energy of B impurities in H-terminated Si NCs for a variety of configuration as a function of the distance from the Si NCs core. Internal substitutional B atoms from subsurface to the NC center (2(2')→3(3')→4(4')→5→6) are shown. Picture adapted from [86]*; b) same as previously for P. Picture adapted from and Cheng at al* [85]

affects the dopant-surface interaction and therefore it is important to theoretically understand how oxidation influences the formation energy of dopant impurities. Comparison between fully H-passivated Si NCs ($Si_{147}H_{100}$) and partially H passivated one ($Si_{147}H_{99}$) suggested a different energetics of the impurity atoms in the Si NCs depending on their surface passivation. In particular for the latter case it was demonstrated that P atoms preferentially locate at surface sites while B atoms reside in the core of the Si NCs [95]. From a general point of view, for substitutional group III and group V elements, it is shown that the presence of a surface oxygen layer drastically changes the radial dependence of the dopant formation energy. In the Si NCs with silanol surface groups (Si-OH), the formation energy of dopant impurities displays variation of few electron volts, featuring, for most dopant species, a lower energy in the region below the surface and a higher energy at surface sites [34]. In the case of P-doped small Si NCs (87 atoms), it was demonstrated that the presence of silanol surface groups causes P segregation to an outer shell close to the surface, where P is not directly linked to H or OH. Moreover, it suppress the formation of tri-coordinated surface defects [97]. In the case of B and P co-doping of small Si NCs (87 Si atoms) with silanol surface groups, it was revealed that the formation of a P-B bond is energetically favoured, with B positioned at the NCs surface and P at the inner nearby. [10] Ni *et al.* [32] studied P doping of a Si NC (d = 1.4 nm) covered by a 0.25 nm thick SiO_2 layer. According to their simulations, P atoms are preferentially incorporated into the sub-interface i.e. the layer close to the Si/SiO_2 interface. Moreover, for Si NCs with dangling bonds at the Si/SiO_2 interface, they showed that P atoms tend to passivate the dangling bonds and consequently they preferentially reside at the Si/SiO_2 interface. These theoretical results suggest that the presence of dangling bonds and SiO_2 shell at the Si NCs surface reduces the binding energy of P in Si NCs.

In particular the case of P^+ doped 1.5 nm Si NCs covered by a 2 nm-thick amorphous SiO_2 shell was studied in terms of energy formation of impurity atoms within the Si NCs. [33] Figure 1.1.2 (d) shows a pictorial view of an undoped Si NC obtained from molecular dynamics simulation. Unlike H- or OH-terminated Si NCs, in SiO_2 covered Si NCs P^+ ions are found to be more stable in the Si NCs core than at the surface, as shown in Figure 1.1.2 (b). [33] In fact, in

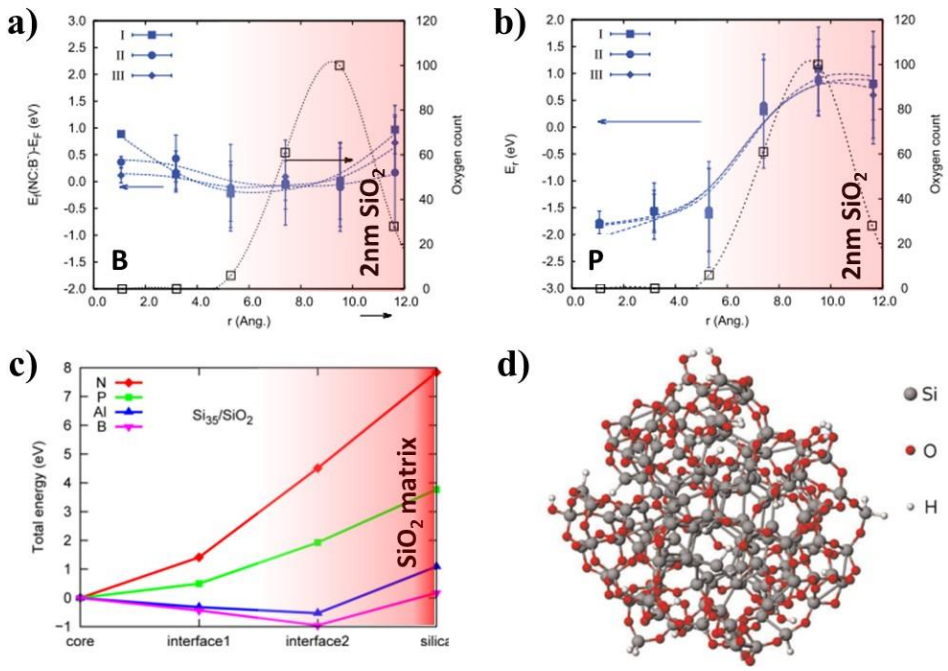

Figure 1.1.2 - a) Relative energy of the 2 nm SiO_2-covered Si NCs doped with B as a function of the distance from the center. Three models for the structure of the nanocrystal were constructed as results of molecular dynamics simulations of 1800 Kanneals during 2.0 ps (I), 2.3 ps (II), and 2.6 ps (III). Open squares represent the distribution of oxygen (coincident for I, II,and III). Picture adapted from Carvalho et al. [96]*; b) same as previously for P. Picture adapted from Carvalho et al.* [96]*; c) Total energy of the 35 Si atom NC embedded in the SiO_2 structure and doped with N, P, Al, or B atoms. The impurities are introduced as substitutional of a Si atom in the NC center (core), at the interface bonded to one or two oxygens (interface1, interface2), or in the SiO_2 far from the NC (silica). For a better comprehensibility each line has been shifted so that the structure with the dopant in the NC center has zero energy. Picture adapted from Guerra et al.* [10]*; d) example of structure of the undoped 2 nm SiO_2-covered nanoparticle, obtained from molecular dynamics simulations, as printed in* [33]

the SiO_2 covered Si NCs the lattice defects at the interface between the Si core and the SiO_2 shell help to release the strain in the Si core and, therefore, chemical bonding effects predominate. The preference of P for the Si core is thus driven by the lower energy necessary to form a P^+-Si bond at the expense of a Si –Si bond, as compared to the energy necessary to form a P^+-O bond at the expense of a Si-O bond. Conversely, in the case of B-doped 1.5 nm diameter Si NCs surrounded by an outer shell of SiO_2 with a thickness of about 0.5 nm, the calculation of the formation energies suggests that B is equally stable in the Si core and in the SiO_2 shell, showing preference for interface sites, as depicted in Figure 1.1.2 (a) [96]. Actually

the cost of replacing Si-Si bonds by a B-Si bond is approximately the same as the cost of replacing a Si-O bond. Moreover, it is shown that the energy formation is closely related to the bond length: the shorter B-Si bonds, the more stable the structure. Since closer to the interface B-Si bonds are on average shorter than in the bulk, this may explain why interface sites are favorite.

Recently theoretical works addressed the subject of doped Si NCs embedded in a solid matrix [10][109]. In the case of very small Si NCs that are composed by 35 atoms, the data indicated that for n-type doping (P and N) the impurity atoms tend to settle the NC core, while for p-type doping (Al and B) the interfacial sites are favored. The energetics of the system as a function of the dopant position shows that SiO_2 forms a very large diffusion barrier for P and N, and a much reduced one for B and Al. Total energy for impurity formation is reported in Figure 1.1.2 (c) [10][109]. According to these data, the preferential location of the impurity seems to be strongly correlated with their electronegativity [10].

1.1.2 Experimental Results

Several works reported doping of Si NCs with B and P, for free-standing Si NCs as well as for Si NCs embedded in a solid matrix. A lot of experimental approaches were implemented to achieve this goal. Clear information about the effective positioning of dopant atoms within the Si NCs are difficult to obtain and data available in the literature on this specific topic are scarce and conflicting. This section provides an overall picture of the main experimental results about dopant incorporation in Si NCs. Literature data are critically reviewed focusing on the problem of thermodynamic stability of dopant atoms. The section is organized in two parts that provide information about the doping of freestanding and embedded Si NCs respectively.

1.1.2.1 Freestanding Si NCs

Many different techniques were implemented for the synthesis of free-standing Si NCs like, for instance, solid-gas reaction, thermal decomposition of silane, laser pyrolysis of silane, laser ablation of solid silicon targets, non thermal plasma synthesis or solution routes. [11] In particular the plasma based methods were proved to be very efficient in producing high quality Si NCs with limited defects' number and a very high control over their size distribution. [110] To date, the plasma-based methods have also been demonstrated to be extremely efficient in the synthesis of doped Si NCs. In recent papers, Ni *et al.* reviewed the literature related to the synthesis of doped Si NCs by plasma routes [111], while Pereira published an interesting review about the doping of semiconductor nanoparticles synthetized in gas-phase plasmas. [110]

Actually free-standing B and P doped Si NCs are readily produced by adding B and P precursor during the plasma process for the synthesis of intrinsic Si NCs [60], [62], [112]. In this case impurity incorporation is performed during NC formation. The most widely used dopant precursors are diborane (B_2H_6) and phosphine (PH_3) [99][113][114][115][116]. Recently it was shown that also organic dopant precursors, like TMP or $P(OCH_3)_3$, could be efficiently employed for the doping of Si NCs, providing a safe and economical solution to the problem [117]. Varying the ratio of silane to dopant precursor, it is possible to effectively control dopant concentration within the Si NCs over a fairly wide range of values [114][99]. For these systems, dopant levels ranging from 10^{18} to 10^{22} cm^{-3} were typically reported both for P [118][99][119] and B [119][64][120]. These values correspond to a dopant concentration

around 1 at.%. Actually very high concentrations of 20 at.% for P and 30 at.% for B were obtained, leading to the so-called hyperdoped freestanding Si NCs [113]. It is worth to note that these dopant concentrations correspond to total values, without any distinction between dopant atoms trapped at the Si NC surface and incorporated in the Si NC core.

In order to understand dopant location, several experimental approaches were implemented using different techniques that provide information about the local environment of the incorporated dopant atoms. Pereira *et al.* used electron paramagnetic resonance (EPR) to demonstrate the presence of P in substitutional location for P-doped Si NCs (4 nm < d < 50 nm) grown in a low pressure, flow-through microwave plasma reactor [121][118]. Using electrically detected magnetic resonance (EDMR), the presence of P atoms in substitutional location was observed also in P-doped Si NCs (5 nm < d < 10 nm) produced using a very high frequency plasma deposition system. [122] The combination of X-ray Photoelectron spectroscopy (XPS) and EPR data indicated that P atoms can be introduced into substitutional sites within Si NCs grown in a high frequency non-thermal plasma system using organic dopant precursor. [117] Pi *et al.* compared the concentration of B and P in ~3.6 nm Si NCs before and after removal of surface oxide by HF treatment [83]. Effective reduction of dopant concentration in Si NCs upon HF etching was observed as shown in Figure 1.1.3 (a). Experimental data suggest that B atoms are preferentially located in the Si NC core, while P atoms reside at the NCs surface. The different distribution of B and P atoms in plasma-synthetized Si NCs was detected also by Stegner *et al.* [99] and Zhou *et al.* [113] in quite similar but independent experiments. In particular, Stegner *et al.* measured P concentration in Si NCs before and after etching of the SiO_2 outer shell by secondary ion mass spectrometry (SIMS). Experimental data are reported in Figure 1.1.3 (b). Interestingly Pi *et al.* reported a percentage of P in the thin SiO_2 outer shell of Si NCs, that is ~80%. This value is significantly lower than the one (~95%) observed by Stegner *et al.*. The reason for this difference is unclear. Perhaps it could be related to the higher temperature experienced by the P doped Si NCs during growth in microwave plasma reactors when compared to RF plasma reactors. This could enhance the diffusion of P atoms towards the surface. The difference could also originate from a longer plasma residence time in the case of Si NCs grown in microwave reactors [110]. Rowe *et al.* observed a similar P distribution within heavily doped ~10 nm Si NCs synthetized in a RF capacitively coupled non-thermal plasma system. Scanning TEM (STEM) imaging with energy-dispersive X-ray spectroscopy (EDX) measurements suggested that P is either incorporated into the Si NCs and/or condensed at the Si NC surfaces. The presence of surface $Si–P_x–H_y$ vibrations in localized surface plasmon resonance (LSPR) analysis indicated the occurrence of significant P segregation at the Si NC surface. P concentration inside Si NCs was measured before and after wet chemical etching of native oxide shell surrounding Si NCs. Experimental data suggest that 60–75% of P is condensed on the NC surface, as shown in Figure 1.1.3 (c). [22]

As discussed in section 1.1.1 , theoretical simulations predict that, in the case of Si NCs covered by an amorphous SiO_2 shell, P atoms are more stably incorporated in the Si NC core [33], while B atoms appear to be equally stable in the Si core and in the SiO_2 shell, showing a clear preference for interface sites [96]. The theoretical picture is based on the assumption of thermal equilibrium that does not apply for doping of Si NCs during their synthesis in plasma. Indeed, impurity incorporation during NC formation makes hard to experimentally decouple equilibrium properties from kinetic effects. In their study on hyperdoped Si NCs, Zou *et al.* [113] suggested that doping in non-thermal plasma systems is mainly controlled by

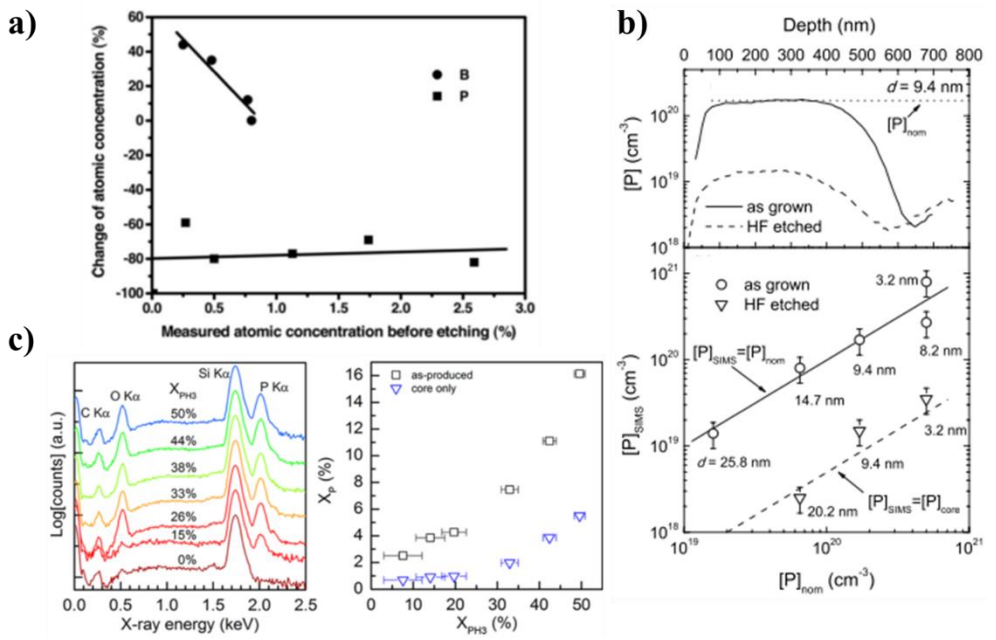

Figure 1.1.3 - a) change of dopant concentration after HF etching of 3.6 nm size Si NCs synthetized by nonthermal plasma, as printed by Pi et al. [83]*; b) top: SIMS profiles of thin films of Si-NCs with a mean diameter of 9.4 nm synthetized by low pressure microwave plasma. $[P]_{nom}$, calculated as the fraction of phosphine in the total flow of precursor gases (SiH_4 and PH_3) multiplied by the atomic density of Si, corresponds to $[P]_{nom}=1.7\ 10^{20}\ cm^{-3}$, the solid curve shows the profile of the as-deposited film, the dashed curve was measured after HF etching. Bottom: Measured P concentration, $[P]_{SIMS}$, extracted from the plateau regions of the SIMS profiles, versus $[P]_{nom}$ before (circles) and after etching in HF (triangles). The data points are labeled with the mean Si NC diameter of the measured samples. The solid line correspond to $[P]_{SIMS}=[P]_{nom}$ and the dashed line shows $[P]_{SIMS}=[P]_{nom}/20$. Figure reprinted from Stegner et al.* [99] *; c) Left: Semilog plot of SEM-EDX spectra of as-produced Si NCs synthetized by RF capacitively coupled nonthermal plasma for varying fractional PH_3 flow rate (X_{PH3}). C, O, Si, and P Kα lines are identified at 0.277, 0.525, 1.74, and 2.01 keV respectively. Oxygen and carbon contaminations are estimated at less than 3 at% and are the result of air exposure during sample transfer. Spectra are offset vertically for clarity. Right: estimated atomic P concentration X_P from SEM-EDX spectra for as produced samples (squares) and for samples after surface P had been removed to probe the Si NC core (inverted triangles). Picture reproduced from Rowe et al.* [22]

kinetics. They designed a simplified kinetics model in which the resulting dopant concentration is basically determined by the frequency of collision between impurities and Si NC. The collision may lead to the adsorption of B and P atoms on the Si NCs surface and the

adsorbed B or P atoms could then be trapped during the subsequent growth of Si NCs. Collision frequency is shown to strongly depend on impurity mass, so that collision frequency for B is larger than that for P. Consequently B atom concentration can reach 30 at.%, while P is limited to 20 at.%. Actually this model was specifically designed for Si NCs with B or P to concentration that are well beyond the solubility limit (1 at.% for B and 0.3 at,% for P [123]) of these impurities in bulk silicon. Interestingly very high dopant concentrations were observed also in freestanding Si NCs obtained by solution synthetic methods. In solution routes, suitable precursors are reacted in an inert atmosphere to reduce the possibility of oxidation [74]. Reduction of a mixture of $SiCl_4$ and PCl_3 with Mg results in P-doping at about 6% atomic concentration in Si NCs (5-12 nm), that is much higher than solubility limit in bulk silicon. [124]

In conclusion, experimental results on doped freestanding Si NCs undoubtedly demonstrate that B and P impurity incorporation into Si NCs is kinetically possible. Unfortunately, for freestanding Si NCs, data available in the literature were obtained by means of doping strategies that do not allow decoupling impurity incorporation from Si NC formation. Consequently, these experimental results do not provide information about thermodynamic stability of dopants in Si NCs.

1.1.2.2 Embedded Si NCs

Actually Si NCs can be easily synthesized within a dielectric matrix using a two-step process involving the formation of a silicon supersaturated film, followed by annealing at high temperature in an inert atmosphere. During the thermal treatment, the silicon supersaturated film, which can be an oxide, nitride or carbide, undergoes a phase separation, resulting in the nucleation of Si NCs embedded in an amorphous dielectric matrix. [11][36] Several approaches were proposed to form these silicon supersaturated films within a SiO_2 matrix, including sputtering [90][125][75], plasma-enhanced chemical vapor deposition [126], ion implantation [23][127] and reactive ion etching [128]. In this system, doping of Si NCs is usually performed by introducing dopant impurities in the matrix before NCs formation. The subsequent high temperature thermal treatment induces dopant incorporation and Si NCs formation simultaneously. This approach does not allow experimentally decoupling equilibrium properties of the system from kinetic effects. For this reason, more recently, significant efforts were performed to develop alternative approaches that allow doping Si NCs after their formation. Consequently, this subsection is organized in two parts. In the first part, I systematically review the results about successful doping of Si NCs that were achieved by experimental approaches in which doping and synthesis occur together. In the second part, I focus on the experimental results that were achieved by decoupling synthesis and doping steps.

Doping during Synthesis

In 1996, for the first time, Fujii *et al.* reported on the effective introduction of B atoms into Si NCs dispersed in a ~2µm thick borosilicate glass. Samples were prepared by cosputtering of Si, SiO_2 and B_2O_3 targets and subsequent annealing at high temperature [90]. The formation of Si NCs in the dielectric matrix was demonstrated by HRTEM, while the doping of B atoms into Si nanocrystals was confirmed by Raman spectroscopy. In this method, the size of NCs could be controlled varying the effective silicon concentration in the matrix, i.e. the number of Si targets during cosputtering, and/or by changing the annealing temperature. Similarly,

overall B concentration in the oxide film is finely tuned by adjusting the number of B_2O_3 targets during cosputtering. The authors reported that Si NC photoluminescence (PL) is drastically quenched by increasing B concentration, as shown in Figure 1.1.4 (a). The decrease in PL efficiency is explained assuming B atoms are incorporated within the Si NCs in substitutional sites. Indeed, substitutional B atoms introduce free carriers (holes) that led to non-radiative Auger recombination effect, which efficiently quench natural PL emission in Si NCs [129]. In a subsequent work on B doped Si NCs synthetized by this cosputtering method, Xie *et al.* suggested the concurrent presence of B atoms in substitutional sites within Si NCs and in the oxide film and/or interface between Si NCs and the surrounding matrix [130]. Figure 1.1.5 shows the high resolution XPS spectra of the B 1s core level corresponding to a change of the total B concentration in the oxide films from 0.59 at.% to 5.43 at.%. The presence of a B-O component in the XPS spectra suggests the existence of B atoms in the SiO_2 matrix and/or at the Si NCs/SiO_2 interface. The B-B/B-Si component indicates that B atoms exist in substitutional sites inside Si NCs. According to these data the amount of B atoms trapped into the Si NCs ranges from 0.25 at.% for the sample with the lowest B concentration to 2.32 at.% for the sample with the highest B concentration. No evidence of self-purification phenomena is observed irrespective of the very small size ($2 < d < 15$ nm) of the Si NCs.

The same cosputtering method was used to synthesize P doped Si NCs dispersed in a phosphosilicate glass. [131] Figure 1.1.4 (b) shows an initial increase of PL efficiency in lightly doped Si NCs [131][19], followed by a sudden decrease of PL emission when further increasing P concentration. [132][133] Fujii *et al.* explained the PL enhancement observed at low P concentration, as a consequence of the passivation of interface defects such as dangling bonds by P atom impurities [131]. At high P concentration P atoms introduce free carriers that, leading to Auger effect, induce a significant decrease of PL efficiency [19]. It is worth to

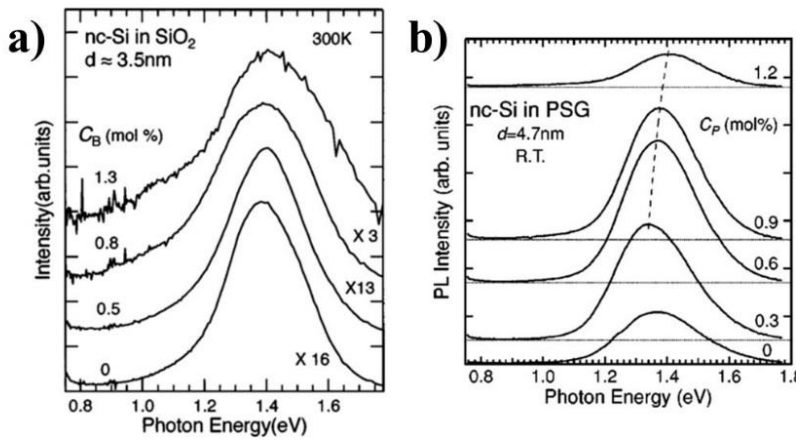

Figure 1.1.4 *- a) PL spectra of B doped 3.5 nm size Si NCs synthetized by cosputteruing method. C_B is the concentration (mol %) of B_2O_3 in the matrix region estimated from IR absorption spectra. Picture reproduced from Fujii et al.* [129]*; b) Photoluminescence from P doped 4.7 nm size Si NCs dispersed in PSG thin films. The average concentration of P_2O_5 in the films C_P (mol%) was determined by electron probe microanalysis. Picture as printed in Mimura et al.* [132]

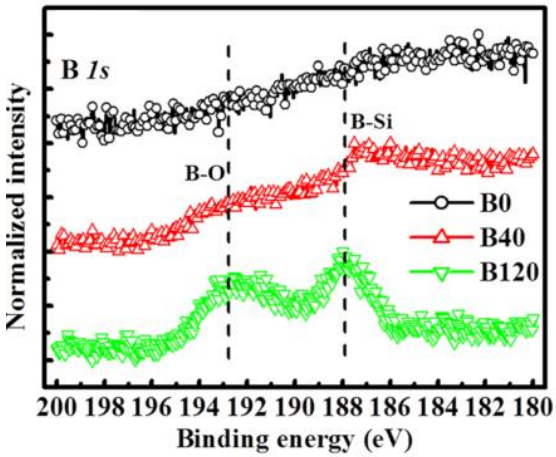

Figure 1.1.5 *- XPS high resolution spectra of B 1s core level region for different B concentrations: 0 at.% (B0), 0.59 at.% (B40) and 5.43 at.% (B120). Si NCs were synthetized by cosputtering method and their diameter ranges from 2 to 15 nm. B concentration is estimated by quantified XPS analysis. Figure as printed in Xie et al.* [130]

note that PL measurements do not provide any direct measurement of effective dopant location inside NCs. Indeed, the assumption that PL efficiency variations are linked to different impurity position within the Si NCs is based on knowledge acquired on free carriers in bulk Si. Nevertheless, this knowledge transfer from bulk to nanostructured silicon might be misleading because a delocalized carrier inside a NC remains physically confined by the NC. [85]

In a very recent work, Nomoto *et al.* studied several types of Si NCs doped with B and/or P impurity atoms synthetized by cosputtering method. The distribution of B and/or P atoms in the Si NCs was investigated by APT and proximity histogram (proxigram) analysis. Proxigram analysis revealed that, for P doped Si NCs, P concentration increases rapidly when moving from the region located approximately 1 nm outside the NC interface toward the core of the Si NC, suggesting P segregation inside NCs and near the surface. On the contrary, in the B doped samples, B concentration slightly decreases when moving from the Si NC interface toward the core of the Si NC. Moreover, they observed that co-doping effectively promotes segregation of the B and P atoms near the interface and within the NC regions. APT cluster analysis revealed the presence of B-P clusters in the co-doped Si NCs. Finally, they confirmed that B and P atoms are successfully incorporated even in very small Si NCs with diameter ranging from 2 to 4 nm. [134]

Alternatively doped Si NCs embedded in a SiO_2 matrix were synthesized by means of a superlattice approach. [135][80] Phase separation and thermal crystallization in SiO_x/SiO_2 superlattice result in the formation of 2-dimensional layers of Si NCs separated by thin SiO_2 layers [75][73]. P doping is commonly achieved by selectively adding a diluted phosphine gas (PH_3) during the superlattice deposition process. This technique permits to add dopants either to the Si rich layer or to the SiO_2 separation layer. Eventually dopants can be systematically

introduced in both layers. This flexibility of the process allows a careful adjustment of the total dopant concentration within the original multilayer structure. Recently Gutsch *et al.* demonstrated that for Si NCs with average size from 3nm to 4 nm, P concentration can be finely tuned from 1.15 at.% to 1.75 at.%. Moreover, they observed that PL peak maximum exhibits a blue-shift as doping concentration increase, while PL intensity progressively decreases. Moreover, a significant reduction of PL intensity is observed after hydrogen passivation. These general trends are attributed to the preferential doping of larger Si NCS, which results in the effective removal of their PL contribution due to Auger recombination inducing PL quenching [135]. On a similar system, Gutsch *et al*. highlighted the low doping efficiency of substitutional P atoms as compared to the large amount of P usually detected in Si NCs. They proposed that P atoms may not necessary occupy substitutional lattice sites but they are rather incorporated as interstitial or P vacancy pairs [80]. Subsequently, based on experimental results about electronic transport in P doped Si NCs, Konig *et al.* suggested that P atoms predominantly reside in interstitial sites [81]. More recently, Gnaser *et al.* prepared a multilayer structure with P doped Si NCs (2.9 nm < d < 4.5 nm) embedded in a SiO_2 matrix. The precise localization and the proper amount of P atoms inside the samples were accurately and quantitatively derived by 3D APT analysis. Figure. 1.1.6 (a) shows the results of the APT analysis. A significant P enrichment at the Si NCs/SiO_2 interface is detected (top) and P concentration inside Si NCs is observed to strongly decrease as Si NCs size decreases (bottom) [14]. The authors suggested that this trend could be considered as an experimental confirmation of the occurrence of a self-purification mechanism in very small Si NCs. Actually, the link between the preferential doping of large Si NCs and the self-purification mechanism is not trivial since doping of the Si NCs was achieved out of equilibrium during Si NC synthesis. As a matter of fact, the preferential doping of larger NCs could be related to the probability of P atoms to be trapped in Si NCs if they can bind to their surface for a residence time comparable to the reciprocal growth rate, which is obviously higher for larger NCs.

Actually, efficient incorporation of P atoms in Si NCs with diameter of 2 nm was demonstrated in a quite similar system by Perego *et al.*, [16][17] suggesting that preferential doping of large Si NCs reported by Gnaser *et al.* is strongly dependent on the specific experimental approach that is used for dopant introduction. In more details, Perego *et al.* prepared a SiO/SiO_2 superlattice structure by e-beam evaporation and introduced an ultrathin (thickness < 0.5 nm) P-SiO_2 layer close to each SiO layer. [16][17] This approach allows delivering a controlled amount of P atoms in the Si-rich region and to incorporate them in the Si NCs during the subsequent high temperature thermal treatment. In order to obtain information on diffusion and segregation phenomena in superlattice structure, the samples were annealed at different temperatures ranging from 900° C to 1000° C. TEM images demonstrated that Si NCs average diameter is equal or smaller than 2nm. Time-of-flight SIMS (ToF-SIMS) results indicated a segregation of P atoms in the Si NCs region during thermal treatment. The incorporation of P impurities within Si NCs was supported by XPS chemical analysis. Figure 1.1.6 (b) shows the high-resolution XPS spectra of the P 2*p* core level region in the as deposited and annealed samples. Data highlight an increase of the signal related to P-Si bonding with increasing annealing temperature, while the opposite trend is observed for the signals related to P-O bonding, indicating that P atoms are definitely incorporated within the Si NCs. P incorporation in Si NCs was explained considering that P diffusion in SiO_2 is much lower than in Si, and, consequently, P diffusion towards the Si-rich region is strongly favored as revealed by ToF-SIMS analysis. Moreover, P atoms in a SiO_x matrix were shown to preferentially form P–Si or P–P bonds. [136] Accordingly for P atoms it is energetically favorable to diffuse in the Si-rich

region, forming stable P–Si bonding. Si nanocluster nucleation and growth occurs during the very first stages of the thermal treatment. Long annealing times are usually required to crystallize the amorphous Si nanostructures. In this picture the P atoms are expected to segregate in the SiO_x layers and to be trapped in the Si nanocluster region during the first stages of the thermal treatment. Although no information is available on P diffusivity in Si nanostructures, the authors assumed that the probability for a P atom to leave the Si-rich region where Si nanocrystal formation occurs is limited by the low diffusivity of P in the SiO_2 surrounding matrix. This fact increases the probability for the P atom to be trapped in the Si nanocrystals under formation. [16][17]

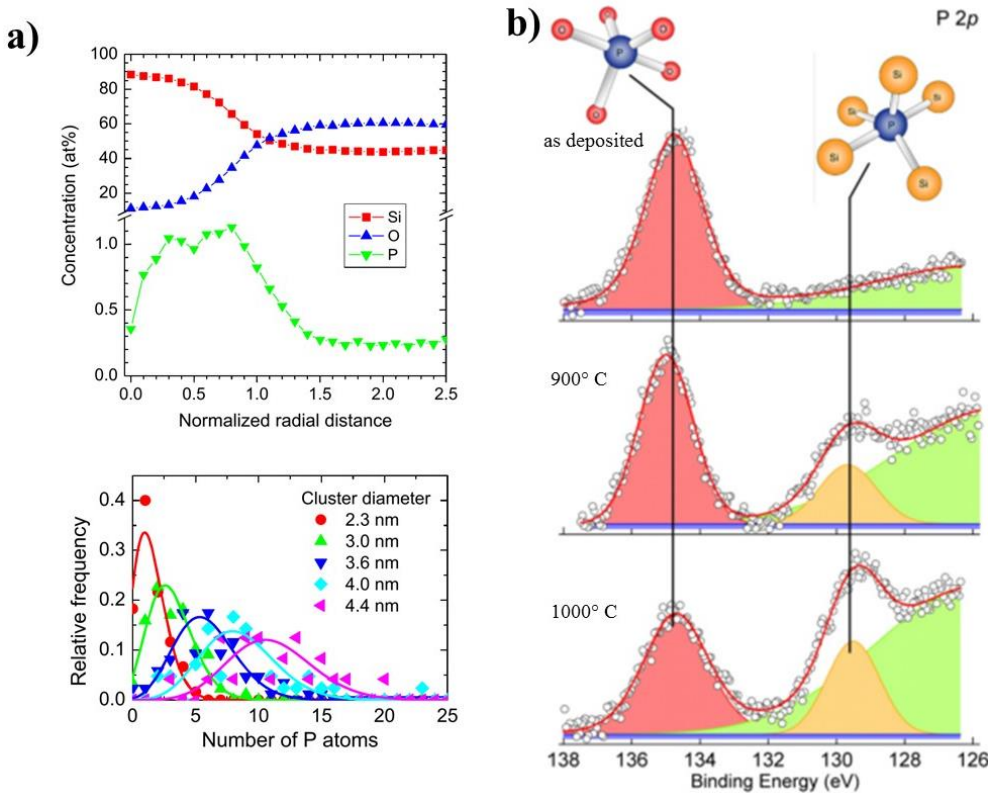

Figure 1.1.6 *- a) Top: APT cluster concentration radial profile for the elements Si, O, and P for Si NCs arranged in a superlattices. The extension of all clusters is normalized to a distance between 0 and 1. Data with abscissa-values of <1.0 would correspond to the interior of the Si NCs. Bottom: Poisson distribution fits (solid lines) for the number of P atoms within Si NCs of different size derived from the APT cluster analysis. Figures adapted from Gnaser et al.* [14]*; b) High resolution XPS spectra of the P 2p region for the as-deposited, 900 ◦C and 1000 ◦C annealed samples. Si NCs with average diameter equal or smaller than 2nm are arranged in a superlattices. Figure reproduced from Perego et al.* [216]

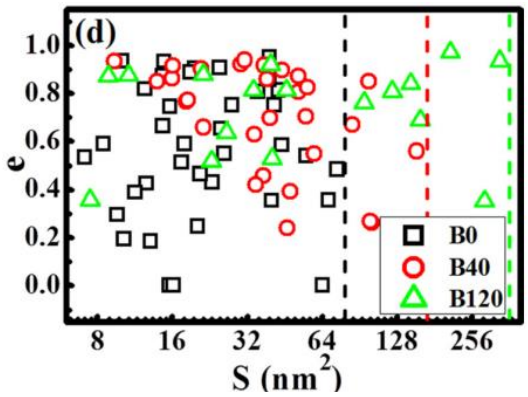

Figure 1.1.7 - Statistical analysis on the shape (eccentricity, e) and size (cross-sectional area, S) of Si-NCs from HRTEM images for different B concentration: 0 at.% (B0), 0.59 at.% (B40) and 5.43 at.% (B120).. Figure reproduced from Xie et al. [130]

Interestingly, Khelifi *et al.* [23] demonstrated that co-implantation, with overlapping projected ranges of Si and P or As, in a 200 nm thick SiO_2 film followed by thermal annealing is an efficient way to form doped Si NCs embedded in SiO_2 with average diameter around 2 nm. Once again APT is used to directly image the spatial distribution of the various species at the atomic scale, evidencing that the P and As are efficiently introduced inside Si NCs. Their APT data do not show any evidence of P accumulation at Si NCs/SiO_2 interface, in contrast with data reported by Gnaser *et al*. [14] and by Nomoto *et al*. [134]. It has to be considered that Khelifi *et al*. concluded their assumption by the occurrence of P and OP molecules in the APT mass spectrum, while both Gnaser *et al.* and Nomoto *et al.* analyzed their data by means of the proxigram method. Moreover, the dopant incorporation within Si NCs was promoted following different experimental approaches. For all these reasons a direct comparison among these experimental results is anything but straightforward.

In conclusion, these experimental results demonstrated that dopant incorporation into Si NCs is kinetically possible. However, the presence of impurities during the Si NCs synthesis significantly affect the growth kinetics of Si NCs. This is corroborated by the observation of size variation of the resulting Si NCs as a function of the nature and/or concentration of dopant impurities, as shown in Figure 1.1.7. [23][130] Some authors claimed to have experimentally demonstrated self-purification mechanism due to the observed preferential P doping of larger Si NCs (4.5 nm size) with respect to the smaller ones (2.9 nm size) [14]. Conversely, other authors demonstrated that very small NCs (2nm size) can be effectively P doped during their growth [16]. As a matter of fact, the absence of thermodynamic equilibrium during the realization of these experiments does not allow elucidates the intimate mechanism of dopant incorporation within Si NCs and to finally confirm the real occurrence of self-purification phenomena in very small Si NCs.

Doping after synthesis

To overcome these experimental limitations, an alternative doping strategy was developed by introducing dopant impurities into the Si NCs after the synthesis of Si NCs. The most popular approach consists in the doping of Si NCs by means of P^+ ion implantation. Many

literature works focused on Si NCs embedded in thick SiO_2 films (0.1 µm - 0.6µm). P ions are implanted at different energies with doses ranging from 10^{13} cm^{-2} to 10^{17} cm^{-2}. Implantation is commonly followed by thermal annealing at high temperature in order to reduce implantation defects and restore the original Si NC structure [137][138][139]. Kovalev *et al.* [137] observed that upon annealing P atoms redistribute between the SiO_2 matrix and Si NCs. Kachurin *et al.* [89] studied the effects of implantation of P ions on the PL emission of Si NCs as a function of the different implantation doses (from 10^{13} cm^{-2} to 10^{16} cm^{-2}) and annealing temperatures (600–1100 °C). Quenching of PL emission was observed immediately after ion implantation, due to the defects in Si NCs induced by ion implantation. The annealing temperature that is necessary for the recovery of PL emission was observed to increase with P implanted doses. Moreover, the PL intensity exhibited a clear dependence on the dose of implanted P ions, indicating that P atoms are trapped into the Si NCs. Similarly, Tchebotareva *et al.* [139] demonstrated that doping with P atoms at concentration up to 3 10^{19} cm^{-3} leads to a PL enhancement, followed by a progressive decrease in the PL intensity when further increasing P concentration. On the basis of previous data reported by Fujii *et al.* [131], PL enhancement is assumed to be associated with P surface passivation, while the decrease in the PL intensity is attributed to Auger recombination due to incorporation of P impurities in Si NCs. [132] It is important to note that, in these experiments, even if the introduction of dopant in Si NCs is performed after the synthesis of the nanostructures, the implantation damage alters the initial equilibrium, resulting in some cases in the complete amorphization of Si NCs. Consequently, the incorporation of P atoms does not really occur at thermodynamic equilibrium since the dopant redistribution within the sample is accompanied by Si NCs recrystallization.

An alternative experimental approach was recently proposed in couple of papers published by my research group, Perego *et al.* [15] and Mastromatteo *et al.* [140][141]. In our experiments the incorporation of P atoms in Si NCs was promoted after their formation, by delivering a controlled amount of dopant atoms from a spatially separated diffusion source. As discussed in Chapter 3, our results represented the first evidence that P doping of Si NCs in SiO_2 is thermodynamically favored. This experimental approach disclosed opportunities for fundamental studies concerning the physics of doped Si NCs, providing a pathway to clarify the energetics of the doping process at the nanoscale.

1.2 Electrical activity

Impurity doping of bulk Si was widely used to tune the electronic properties of silicon by introducing free carriers that significantly modify its intrinsic conductivity. Doping of Si NCs is performed to achieve the same goal, i.e. control the electrical and optical responses of these nanostructures by the controlled introduction of free carriers. Actually, a clear understanding of the evolution of the effective carrier density in Si NCs as a function of impurity concentration is still lacking. In particular, experimental data collected so far suggest that the capability of dopants to provide free carriers in Si NCs strictly depends on the synthesis method that was used to realize the nanostructures. In this section I briefly summarize the available experimental results about dopants activation within small Si NCs. Theoretical studies on electron and hole transport induced by substitutional B or P doping in Si NCs embedded in a SiO_2 matrix were systematically reviewed by Pi. [87] For further information about theoretical investigation on dopant activation in Si NCs I suggest to look at the recent

work of Garcia-Catello *et al.* [109] Once again the experimental results are revised considering the two cases of freestanding and embedded Si NCs respectively.

1.2.1 Freestanding Si NCs

Zhou *et al.* [113] studied B and P hyper-doped Si NCs (diameter ≈14 nm) synthesized in a non-thermal plasma system. They demonstrated that both B and P atoms may be effective dopants for Si NCs. P hyper-doping was found to induced a significant enhancement of the oxidation of Si NCs, corroborating the hypothesis that P atoms are effectively acting as donors. In fact, as the concentration of electrons in P hyper-doped Si NCs is larger than that of undoped Si NCs, more electrons may tunnel through the oxide to reach the surface, ionizing more O atoms and speeding up the oxidation kinetics. The electrical activity of B impurity atoms was investigated by looking at the Fano effect. [142] B hyperdoped (7 at.% - 31 at%) Si NCs were characterized by Raman spectroscopy. Figure 1.2.1 (a) shows the Raman spectra obtained using two different excitation wavelengths. With the increase of the excitation wavelength the Raman peak at $517\,cm^{-1}$ was broadened toward high wavenumbers. An anti-resonance dip also appeared on the low-wavenumber side of the $517\,cm^{-1}$ peak. These features are both characteristic signatures of the Fano effect, indicating that there are B atoms that act as acceptors in these Si NCs. In a subsequent work on similar samples with hyperdoped Si NCs, Zhou *et al.* [143] found that when the doping levels of B and P are similar, the LSPR energy of B-doped Si NCs is higher than that of P-doped Si NCs because B atoms are more efficiently activated than P atoms in Si NCs.

In the case of P doped Si NCs synthetized in a plasma system, EPR data proved that donor electrons are present [121][144]. As depicted in Figure 1.2.1 (b), a clear resonance centered at g = 1.998 and two further lines denoted hf(^{3}1P) were observed. These features are a clear fingerprint of substitutional and isolated P atoms trapped in the Si NC core. [99]. In the films containing P doped Si NCs, [118][121] it was observed that an increase of the doping concentration in the Si NCs resulted in an increase of the film conductivity and in a concomitant decrease of the temperature dependence of the conductivity. Using electrically detected magnetic resonance (EDMR), it was demonstrated that at low temperature both Si-dangling bonds of the surface and isolated substitutional P states participate in charge transport, demonstrating that charge transport involves electronic states of NC cores and does not take place solely through surface states [118].

All these results proved that the donor electrons that are present in the Si NCs effectively contribute to charge transport enhancement in Si NCs. Nevertheless, a complete picture about the effective impact of doping on charge transport in Si NC films is not yet available because effects like charge trapping in defect states, percolation of charges, and dopant ionization in NCs at room temperature may obscure the effect due to doping of the individual NCs. An example of influence on charge transport due to defect is reported by Lechner *et al.* [91]. They demonstrated that both P and B doping becomes effective dopants only when the concentration of dopant atoms overcomes the concentration of defect traps. Moreover, Pereira *et al.* [145] observed that, in films of Si NCs with a native oxide shell synthetized by plasma, no significant enhancement of conductivity is detectable even for very high ($5\ 10^{20}$

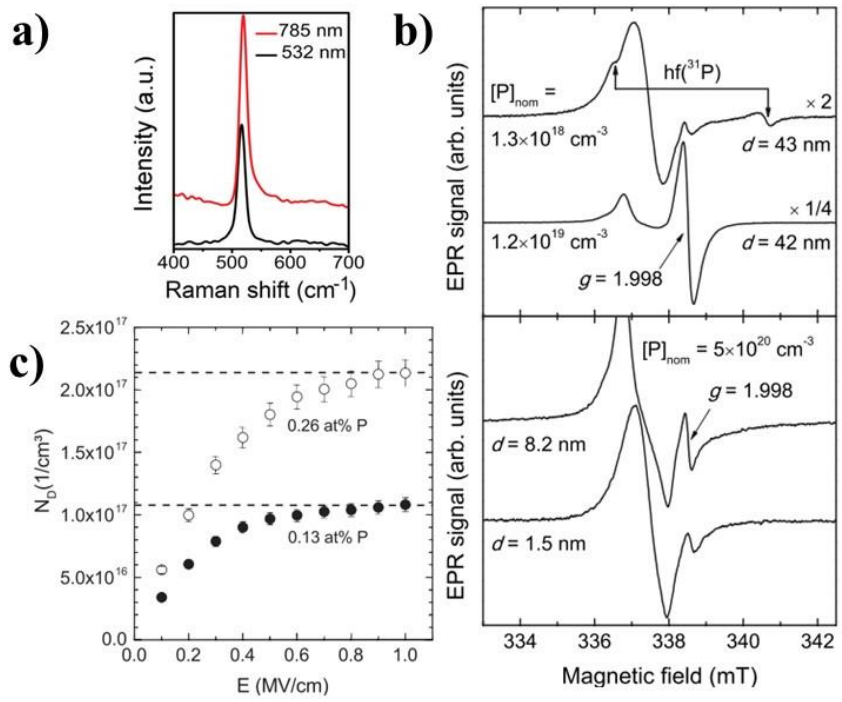

Figure 1.2.1 - a) Raman spectra of ≈14 nm Si NCs hyperdoped with B at the concentration of 7% by means of thermal plasma. Data were obtained with lasers operating at the excitation wavelengths of 532 and 785 nm. Picture reproduced from Zhou et al. [113]*; b) Top: EPR spectra of Si NCs with a mean diameter of 42 and 43 nm grown in a low-pressure microwave plasma reactor, with different P nominal concentration. Bottom: EPR spectra of doped Si-NCs with mean diameters of 8.2 and 1.5 nm grown in a low-pressure microwave plasma reactor at constant P nominal concentration. Pictures as printed in Stegner et al.* [99]*; c) free carrier density calculation from transient current analysis for sample with different total P concentration involved in the synthesis process is plotted as a function of bias voltage. 4 nm size Si NCs are arranged in superlattices and synthetized by PECVD method. Figure as printed in Gutsch et al.* [80]

cm^{-3}) P concentration. Thus, in surface-oxidized Si NCs, charge transport is not limited by the amount of available charges. This indicates that in films of surface-oxidized Si NPs inter-NP charge transfer involves the participation of oxide-related electronic states, whereas in H-terminated Si NP films direct inter-NP charge transfer plays a major role in the overall charge conduction. In recent reviews both Ni [111] and Pereira [110] summarize results about electronic properties of doped Si NCs synthetized by plasma providing an exhaustive description of the experimental results.

1.2.2 Embedded Si NCs

In the case of P doped Si NCs superlattices embedded in a SiO_2 matrix synthetized by PECVD method, transient current analysis demonstrated that the effective concentration of electron available for current transport within the P doped NC conduction band corresponds to only 0.12% of the total P concentration. [80] This result was suggested to be a consequence of the incorporation of P dopants in the NCs as interstitial impurities rather than as substitutional donors. [80][81] In fact, on the basis of density functional theory calculations, interstitial P dopants in Si NCs are expected to introduce deep trap states which cannot donate electrons but provide efficient carrier recombination [81]. Nevertheless, doubling the P concentration yields twice the amount of carriers [80]. Figure 1.2.1 (c) reports free carrier density derived from transient current analysis as a function of bias voltage. Analysis was performed on samples with different total P concentration. In a very recent work Almeida *et al.,* [144] studied P doping of 5 nm Si NCs synthetized by cosputtering method using EPR spectroscopy. Fig. 1.2.2 shows the EPR spectra and the corresponding numerical fitting curve. Data indicate that most P dopants are incorporated at substitutional sites of the NCs lattice and thus effectively act as donor. Moreover, they observed that the donor electron density decreases by several orders of magnitude when the NCs are treated in HF to remove the native SiO_2 matrix and subsequently exposed to air. They interpreted this observation as charge compensation of P donors in the NCs by traps associated to molecules adsorbed to NC surface. Interestingly the process can be completely reverted by desorbing the molecule from Si NC surface in vacuum. The extreme difference in terms of dopant activation for the P doped Si NCs embedded in SiO_2 matrix synthetized by PECVD method and those synthetized by cosputtering method, suggests that, as the doping efficiency depends on dopants locations,

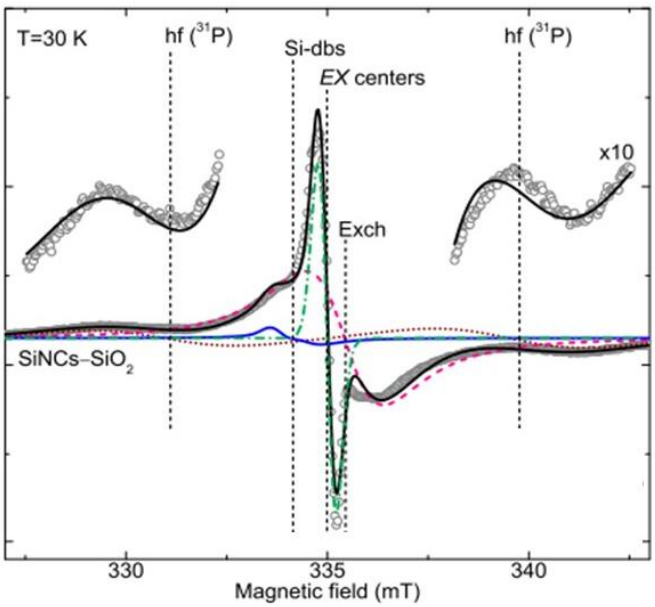

Figure 1.2.2 *- EPR spectra of 5 nm size Si NCs embedded in SiO_2 matrix synthetized by cosputtering method and its numerical fit. Picture as printed in Almeida et al.* [144]

the synthesis method can affect the donor electron distribution within the Si NCs. Unfortunately, no experimental techniques are able to provide a direct measurement of the P distribution within the Si NCs. All the informations are usually obtained by indirect measurements and interpretation models whose validity has not been completely assessed yet.

1.3 Conclusions

In this chapter I provide an extensive review of the most recent experimental and theoretical results about doping of Si NCs. Introduction of dopant impurities in very small Si NCs have been achieved using several approaches. However the effective positioning and thermodynamic stability of the dopant impurities within the Si NCs are not clear and represent the subject of an intense research activity. Recent experimental results about Si NCs embedded in a dielectric matrix suggest that P impurities are incorporated within the core and/or in the region below the Si NCs/SiO_2 interface. The effective activation of these impurities i.e. the availability of free charges in the Si NCs is questionable. Actually, a complete theoretical and experimental description of the energetics of these systems is still missing.

2 – Experimental

2.1 Synthesis and processing

This section is divided in two parts. The first one regards the synthesis of Si NCs, the second one focused on the synthesis of dopant layers to be used as dopant sources.

2.1.1 Silicon NCs embedded in SiO_2

Si NCs can be synthesized within a dielectric matrix using a two-step process involving the formation of a silicon supersaturated film, followed by annealing at high temperature in an inert atmosphere. During the thermal treatment, the silicon supersaturated film, which can be an oxide, nitride or carbide, undergoes a phase separation, resulting in the nucleation of Si NCs embedded in an amorphous dielectric matrix [11][36]. Several approaches were proposed to form silicon supersaturated films within a SiO_2 matrix [39]–[49]. In our experiments we synthetized Si NCs by means of high temperature thermal treatment of a SiO_2/SiO/SiO_2 multilayer [80][135], deposited by electron-beam deposition. The thermal treatment was performed in tubular furnace.

2.1.1.1 Electron-beam evaporator

Electron-beam evaporator is a physical vapor deposition (PVD) technique where an intense electron beam strike source material and vaporize it within a vacuum environment [146]. Schematic setup of e-beam evaporator is depicted in Figure 2.1.1. Usually in this system, high voltage electrical supplies heat a tungsten filament until it is incandescent. The filament then spontaneously and randomly emits electrons. An anode plate collects the electrons and forms them into a beam which is accelerated through high voltage potential (about 5 kV). Magnetic fields, usually created by a permanent magnet, deflect the beam until it impacts on the material in the crucible. If the electron beam has sufficient energy, the material in the crucible is evaporated. The evaporated atoms travel thrown the vacuum chamber, at thermal energy (less than 1 eV), and can be used to coat a substrate positioned above the evaporating material. Since thermal energy is so low, the pressure in the chamber must be low enough to ensure that the electron mean free path is longer than the distance between the electron beam source and the target substrate. The mean free path is the average distance that an atom or molecule can travel in a vacuum chamber before it collides with another particle

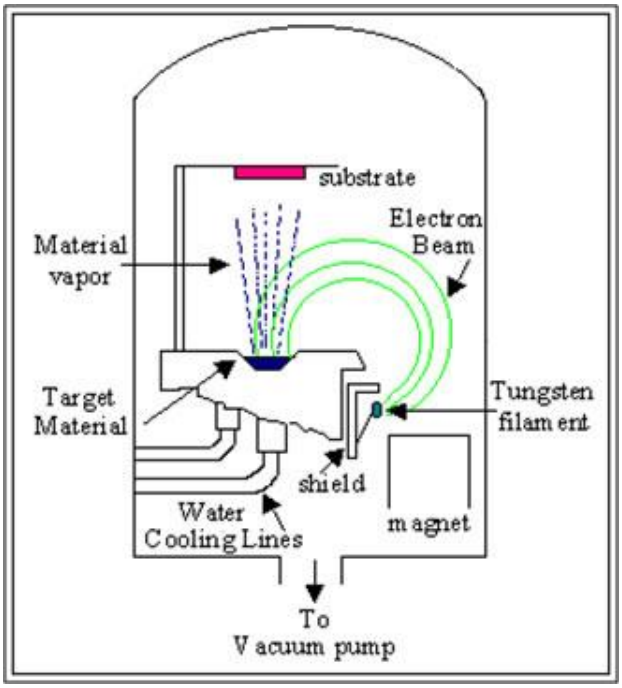

Figure 2.1.1 – Schematic setup of an electron beam evaporator

thereby disturbing its direction to some degree. This is typically around 4.0 x 10^{-4} mbar or lower. Usually, the thickness of the films deposited on the target is monitored during the deposition by a microbalance system that measures the resonant frequency of oscillation of a crystal. This frequency changes as the thickness of the film deposited on the crystal changes. To compensate for differences between the source-to-substrate and source-to-crystal distances, a calibration or "tooling factor" is introduced. In this way, the film thickness of material deposited on the substrate is directly calculated from the thickness of the film on the crystal of the microbalance.

The laboratory is equipped with two electron-beam evaporators: a four-crucible e-beam gun working in high vacuum (base pressure 3×10^{-7} mbar), Kurt J. Lesker, and a conventional evaporator placed in clean room, Edwards EB3.

2.1.1.2 Furnace

Si NCs nucleation and growth was promoted by high temperature annealing in a conventional LTF-Lenton tubular furnace [147]. This furnace has a maximum operating temperature of 1200°C. Heating is provided by a resistance wire element wound on to the ceramic work tube which is an integral part of the furnace. Low thermal mass insulation is used throughout for rapid response rates and maximum thermal efficiency and stability. A rugged metal sheathed thermocouple is protected from accidental damage and allows full use of the work tube bore. Furnace reach the target temperatures with an heating rump of 5° C /min. An example of the behavior of temperature during a cycle is reported in Figure 2.1.2.

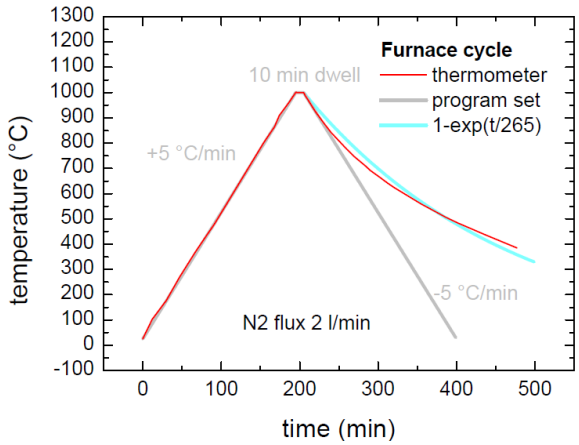

Figure 2.1.2 *-Example of the behavior of temperature during a cycle (1000° C, 10 min) in tubular furnace*

2.1.2 Doping source

The process used to synthetize the dopant δ-layer by dopant-terminated homopolymers involves the use of different tools, like Spectroscopic Ellipsometry, Rapid Thermal Process and O_2 plasma. Spectroscopic Ellipsometry was used to measure the thickness of the dopant-terminated polymeric layer bonded over the substrate. Rapid Thermal Process induced the grafting of dopant-terminated polymers over SiO_2 surface. O_2 plasma was used to clean the surface from residual polymeric fraction after dopant δ-layer formation.

2.1.2.1 Spectroscopic Ellipsometry

Spectroscopic Ellipsometry (SE) is an optical technique used for the investigation of the thickness and the optical properties of thin films [148]. It is worth to say that it is nondestructive and contactless. Thanks to the analysis of the change of polarization of light reflected on a sample, SE can yield information about layers that are thinner than the wavelength of the probing light itself. SE can probe the complex refractive index, which gives access to fundamental physical parameters and it is related to a variety of sample properties. It is commonly used to characterize film thickness for single layer or complex multilayers ranging from a few nm to several μm [149].

In SE light is emitted by a lamp and linearly polarized by a polarizer. It can pass through an optional compensator (retarder, quarter wave plate) and then falls onto a sample. After reflection the radiation passes an optional compensator and a second polarizer, which is called an analyzer, and falls into the detector. The schematic setup of an SE experiment is depicted in Figure 2.1.3. SE is a specular optical technique in the sense that the angle of incidence is equal to the angle of reflection. The plane picked out by the incident and the reflected beam is named plane of incidence. Light which is polarized parallel (perpendicular) to this plane is named p-(s-)polarized. The polarization change of the light is determined only by the sample's properties such as thickness and optical constants. Polarization state of the

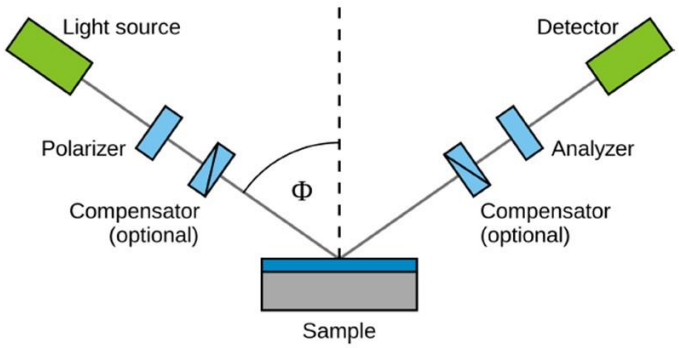

Figure 2.1.3 – *Schematic setup of a Spectroscopic Ellipsometry*

light incident upon the sample may be decomposed into the s and a p component. The amplitudes of these components, after reflection and normalized to their initial value, are denoted by R_s and R_p, respectively. SE actually measures the ratio of R_s and R_p, which is described by the fundamental equation of SE:

$$\rho = \frac{R_p}{R_s} = \tan\varphi \, e^{i\Delta}$$

$\tan\varphi$ and Δ are the amplitude ratio and the phase shift (difference) upon reflection, respectively. Since SE is measuring the ratio of two values rather than their absolute values, it is very robust, accurate and reproducible.

SE is indeed an indirect method; in general the measured φ and Δ cannot be converted directly into the optical constants of the sample and a model analysis must be performed. Thus a layer model must be established, which considers the optical constants and thickness parameters of all individual layers of the sample including the correct layer sequence. By using an iterative procedure (least-squares minimization) unknown optical constants and/or thickness parameters are varied, φ and Δ values are calculated. Among the different models which can be used to achieve thickness information, the Cauchy layer is the most indicated for the measure of transparent thin film, such as polymer films.

All the measures were carried out by M-2000U spectroscopic ellipsometer (J.A. Wolam Co. Inc.) using a Xe lamp at 70° incident angle.

2.1.2.2 Rapid Thermal Process

During Rapid Thermal Process (RTP), radiant energy sources are used, often tungsten-halogen lamps, to heat the sample at very high temperature for a short period (up to a couple of hundred degrees per second). This technique involves a non-equilibrium process. In fact, differently from what happens in a furnace, the components inside the chamber have different temperature: the tungsten-halogen lamps used are much hotter than the sample, and the chamber walls are usually much cooler than the sample.

All thermal treatments have been carried on by using a Jipelec "JetFIrst100" RTP machine. The system includes a cold wall reaction chamber with maximum 4" wafer capability and 30 kW power multi-zone halogen lamp furnace. It can work between 20° C and 1250 °C and can raise the chamber temperature up to 100 °C/s. Furthermore gas inlets are provided for O_2, N_2 and H_2(%5)-N_2 mixture. Chamber valves ensure the capability of working between 1 and 1000 mbar.

2.1.2.3 O_2 Plasma

Plasma cleaning involves the removal of impurities and contaminants from surfaces using an energetic plasma created from gaseous species. Gases such as argon and oxygen, as well as mixtures such as air and hydrogen/nitrogen are used. The plasma is created by using high frequency voltages (typically kHz to MHz) to ionize the low-pressure gas (typically around 1/1000 atmospheric pressure). In plasma, gas atoms are excited to higher energy states and also ionized. As the atoms and molecules "relax" to their normal, lower energy states, they release a photon of light, these results in the characteristic "glow" or light associated with plasma. Different gases give different colors. For example, oxygen plasma emits a light blue color.

A plasma's activated species include atoms, molecules, ions, electrons, free radicals, metastable, and photons in the short wave ultraviolet (vacuum UV, or VUV for short) range. This "soup", which incidentally is around room temperature, then interacts with any surface placed in the plasma. If the gas used is oxygen as in our case, the plasma is an effective, economical, environmentally safe method for critical cleaning. The VUV energy is very effective in the breaking of most organic bonds (i.e., C-H, C-C, C=C, C-O, and C-N) of surface contaminants. This helps to break apart high molecular weight contaminants. A second cleaning action is carried out by the oxygen species created in the plasma (O, O^+, O^-, O_2^+, O_2^- ionized ozone, metastable excited oxygen, and free electrons). These species react with organic contaminants to form H_2O, CO, CO_2, and lower molecular weight hydrocarbons. These compounds have relatively high vapor pressures (means they escapes to space easily) and are evacuated from the chamber during processing. The resulting surface is ultra-clean.

2.2 Characterization

Sample characterization required the development of a characterization protocol integrating multiple techniques. In particular, TEM and APT were used to obtain structural information about Si NCs, like their average size and density. ToF-SIMS was used to study dopant diffusion and incorporation in Si NCs. Rutherford Backscattering Spectrometry (RBS) analysis determined the total P doses inside the sample, allowing ToF-SIMS Profiles quantification. Finally, XPS provided information about chemical environment of P atoms in Si NCs.

2.2.1 Transmission electron Microscopy

TEM is a microscopy technique in which a stationary, coherent beam of electrons is transmitted through an ultra-thin specimen [150]. An image is formed from the interaction of the electrons transmitted through the specimen. The main strength of TEM is its extremely high resolution due to the very small wavelength of electrons. For an accelerator voltage of V = 100 keV, the wavelength of electrons is about 0.004 nm giving a resolution s ≈ 0.25 nm.

Electrons from an electron gun are accelerated to high voltages (from 100 to 400 keV) and focused on the sample by condenser lenses. The sample is placed on a copper grid. The sample must be sufficiently thin (100-200 nm) to be transparent to electrons. The transmitted and forward scattered electrons form a diffraction pattern in the back focal plane and a magnified image in the image plane. With additional lenses either the image or the diffraction pattern is projected onto a fluorescent screen for viewing or for electronic recording. There are three primary imaging modes: bright field, dark field and high resolution microscopy. The most common mode of operation for a TEM is the bright field imaging mode. In this mode the contrast formation is formed directly by occlusion and absorption of electrons in the sample. Thicker regions of the sample, or regions with a higher atomic number will appear dark, whilst regions with no sample in the beam path will appear bright – hence the term "bright field". Since the image contrast is related to scattering and diffraction of electron in the sample, it is possible to form an image using a specific diffracted beam, this mode of operation is named dark field. High resolution images are obtained combining the transmitted and a number of diffracted beams to form an interference image in the image plane of the objectives lens. HRTEM is used to obtain structural information on the atomic size level. The absorption of a small fraction of the electrons induces sample heating that could lead to a modification of the sample during the measurement.

Sample preparation is a weak point of TEM because the sample must be very thin. TEM specimens are required to be at most hundreds of nanometers thick, as unlike neutron or X-Ray radiation the electron beam interacts readily with the sample, an effect that increases roughly with atomic number squared. High quality samples will have a thickness that is comparable to the mean free path of the electrons that travel through the samples, which may be only a few tens of nanometers. Preparation of TEM specimens is specific to the material under analysis and the desired information to obtain from the specimen. In HRTEM the thickness of a silicon sample should be less than 10 nm operating at 200 keV. Many techniques have been used for the preparation of the required thin sections, like mechanical lapping polishing, ion milling and focused ion beam (FIB).

For the imaging of samples used for the study of structural characterization of Si NCs, EFTEM observation was performed on a field emission microscope (Tecnai^{TM} F20, FEI) operating at 200 kV and equipped with an imaging filter (Gatan TRIDIEM). For the imaging of the samples used for the study of *ex situ* doping of Si NCs, TEM measurements were performed using a sub-Angstrom (Cs)-probe-corrected JEOL ARM200CF at a primary beam energy of 200 keV. It is a probe corrected TEM/STEM microscope equipped with a cold-FEG gun and a fully loaded GIF Quantum ER as spectrometer. In both case, EFTEM images were formed from electrons that lose energy around 17 eV (±2 eV), which corresponds to silicon plasmon oscillation energy of Si.

2.2.2 Atom Probe Tomography

APT is a microscopy technique that provides 3D atom-by-atom imaging of materials with a uniquely powerful combination of spatial and chemical resolution. Its spatial resolution is outstanding ($\Delta x \approx \Delta y \approx 0.2$ nm and $\Delta z \approx 0.1$ nm)[151]. Moreover, detection sensitivity results to be very high, as element concentrations down to a few ppm can be detected irrespective of elemental mass. The technique is based on field evaporation of ions from a very sharp needle-shaped sample. By applying either ultra-fast high voltage or laser pulses to a positively biased tip-shaped specimen, surface atoms are field-evaporated layer by layer. The field-

evaporated atoms are ionized and accelerated towards a position sensitive detector that records their time of flight (for chemical analysis) and impact positions (for determination of the original position within the sample). A three-dimensional elemental map can be reconstructed from the collected data, applying an inverse projection of the detector coordinates to the tip surface. Depth-scaling is done taking into account the sequence and volumes of detected atoms. A schematic drawing of APT technique is reported in Figure 2.2.1

Controlling the sample size and its shape is essential for understanding and manipulating the ionic trajectories from specimen surface to detector. The main constrain for APT sample preparation are:

- the specimen must be sharp enough to allow field evaporation (radii on the order of 100 nm)
- it must be robust enough to allow for significant evaporation events to occur
- user-defined features of interest must be present in the near-apex region to ensure that such features are included in the collected data.

Two methods of specimen preparation are prevalent for APT: electropolishing and focused ion beam (FIB) milling.

APT analysis was performed using a laser-assisted local electrode atom probe (LEAP4000X HR, Cameca)[152][153]. A pulsed laser with a 355 nm wavelength was irradiated upon the needle specimen with a repetition rate of 200 kHz and a laser-pulse energy of 90 pJ. The base temperature of the needle specimen during the measurement was 50 K. An Integrated Visualization and Analysis Software (IVAS) protocol was employed to reconstruct the 3D atom map[154].

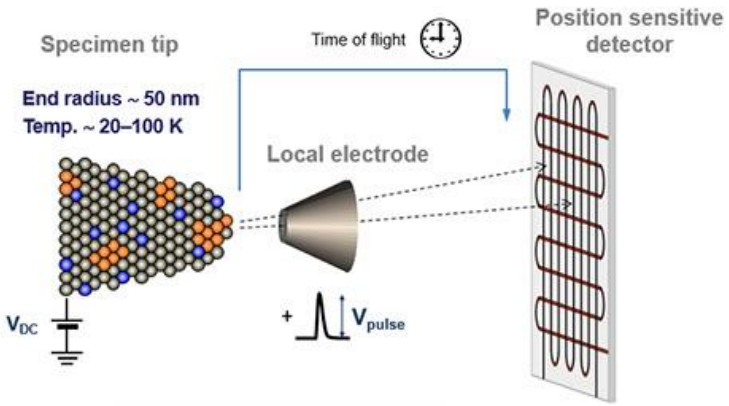

Figure 2.2.1 – Schematic drawing of Atom Probe Tomography

2.2.3 Time of Flight Secondary Ion Mass Spectrometry

SIMS is a technique used in materials science and surface science to analyze the composition of solid surfaces and thin films based on the ejection of charged atomic and molecular species from the surface of a condensed phase (liquid or solid) under heavy particle bombardment. The mass/charge ratio (e/m) of the ionized particles emitted from the surface is analyzed by different types of mass analyzers obtaining a mass spectrum. A schematic description of this technique is reported in Figure 2.2.2. The e/m spectrum supplies information on the chemical composition of the bombarded area.

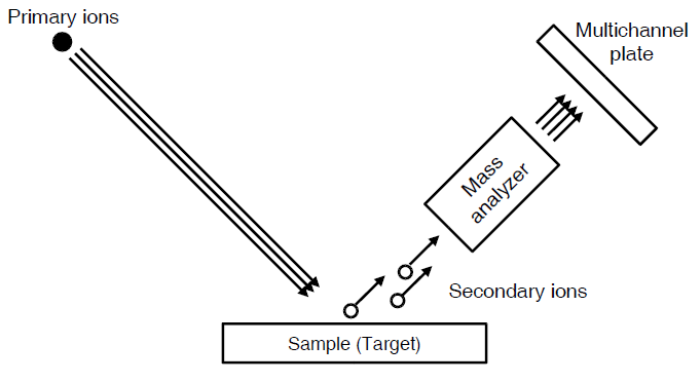

Figure 2.2.2 *– Schematic drawing of Secondary Ion Mass Spectrometry*

2.2.3.1 Basic concept

It is known that, when accelerated ions penetrate into a crystalline target sample, they undergo electronic and nuclear scattering events that could cause a collision cascade. As a matter of fact, during nuclear interactions sufficient energy may be transferred from the ions to the atoms of the sample inducing a displacement from their equilibrium position. These atoms can in turn displace other atoms and so on, creating a cascade of atomic collision. This phenomenon could induce a change of the lattice structure and sputtering. Sputtering takes place when atoms near the surface receive sufficient energy from the incident ion to be ejected from the sample. The flux of sputtered particles emitted from an ion-bombarded surface is characterized by the presence of atoms and polyatomic molecules and clusters. The escape depth of the sputtered atoms is generally a few monolayers. The sputter yield Y_m (the average number of atoms sputtered per incident primary ion) depends on the sample material, on its crystallographic orientation and on the nature, energy and incident angle of the primary ions. Selective or preferential sputtering can occur in multicomponent targets when the components have different sputter yields. The rate of sample etching is called the sputter rate (R) and is defined as the amount of material (Z) removed per sputter time (t):

$$R = \frac{Z}{t} \qquad (2.2.1)$$

Sputter rates depend on a number of parameters, such as the incident ion flux, background pressure of the sputtering species and gas phase composition.

Most of the emitted atoms are neutral but a small fraction (vary in a range of 10^{-2}% to 10% of the total) is ejected as positive or negative ions. As in SIMS only charged particles can be detected by the mass analyzer, it is necessary to introduce the concept of secondary ion yield $Y_m^{\pm}$ (the average number of ions sputtered per incident primary ion). Secondary ion yield is significantly lower than the total yield, but can be influenced strongly by the chemical environment of the sputtered species, it is the well-know matrix effect. Moreover, secondary ion yield can be influenced even more strongly by the type of primary ion. It is well known that the presence of highly electronegative (such as oxygen or nitrogen) or highly electropositive (i.e. cesium) elements onto the surface of interest can promote the emission of positive or negative secondary ions respectively [157][158]. For semiconductors, such as Ge and Si, and for carbon a strong emission of negatively charged clusters occurs. In samples composed of different atomic species, such as silicon oxide, various homonuclear ($Si_n^{\pm}$, $O_n^{\pm}$) and heteronuclear ($Si_nO_m^{\pm}$) cluster can be observed. These clusters were formed during the sputtering process and usually they are not representative of pre-existing cluster.

2.2.3.2 SIMS instruments

A conventional SIMS instrument is composed by an ion gun, an ultra high vacuum chamber and a mass analyzer. By applying a fine focused ion beam and by scanning it over a limited surface area information about the lateral surface distribution of the secondary ion emission can be obtained. The spatial resolution is determined by the spot size of the primary ion beam and resolution less than 1 µm are possible. An image of the chemical composition of the surface can be reconstructed. The removal of atoms and molecules from the surface results in an erosion process.

Regarding the erosion of the surface two different modes of analytical SIMS can be defined:

- Static SIMS: information on the composition of the uppermost monolayer can be collected virtually without modifying the surface composition and structure using very low primary ions current density. For an ion current density of 1 nA $\cdot cm^{-2}$ the lifetime of a monolayer is in the order of some hours.
- Dynamic SIMS: applying high primary ion current densities (up to some A $\cdot cm^{-2}$) the surface erosion continuously moves the actual surface into the bulk material providing information on the composition of originally deeper layers of the bombarded sample. By use of dynamic SIMS depth profiling of element concentration can be achieved with high sensitivity down to ppb range.

Depending on the analytical application different kinds of mass spectrometers can be used for mass separation like magnetic sector field, double focusing sector field, Quadrupole analyze and Time of Flight (ToF).

Time Of Flight SIMS instruments

When it becomes important to detect elements present in low concentration and to have a high lateral resolution, a maximum use of all secondary ions produced by ion bombardment is mandatory. It is worth to say that the instrument transmission factor of the quadrupole based SIMS instrument is only 10^{-4}. Fortunately, it is possible to increase the ion collection by

a three order of magnitude, using a ToF mass analyzer. The main idea of ToF mass spectrometer is that ions with the same energy but different masses need different flight times to pass a certain drift. The mass/charge ratio of each ion can be determined by measuring their flight time.

Compared with the other instruments mentioned above, a TOF mass analyzer presents some advantages:

- A high mass resolution ($m / \Delta m > 10000$)
- An unlimited mass range
- A very high transmission ($f > 0.1$) that is constant over the whole mass range
- A quasi simultaneous detection of all masses of the same sign of charge

The simplest TOF-SIMS instrument consists of a pulsed ion source and a reflectron TOF analyzer where an ion mirror is used to increase mass resolution. In the ion mirror the ions are decelerated by an electric field until they finally turn around and are accelerated again. The higher the initial energy the deeper they penetrate into the reflecting field increasing their flight time. In TOF-SIMS sample erosion is limited by the low duty cycle (10^{-4} - 10^{-5}) of the primary ion gun and is very slow. For this reason, TOF-SIMS originally has not been considered as an appropriate technique for depth profiling. To make use of the above mentioned ToF-SIMS features in depth profiling an additional sputter gun has been integrated into standard ToF-SIMS instrument [157]. Both the analysis and sputter ion gun are operated with the ToF-SIMS repetition rate (Figure 2.2.3). Sometimes charge compensation by means of electron flood gun is employed. The ion guns are synchronized so that the ion flight time into the analyzer is used by the sputter gun to erode the sample. If only a limited mass range or a limited mass resolution is required, it is possible to increase the data rate by improving the duty cycle.

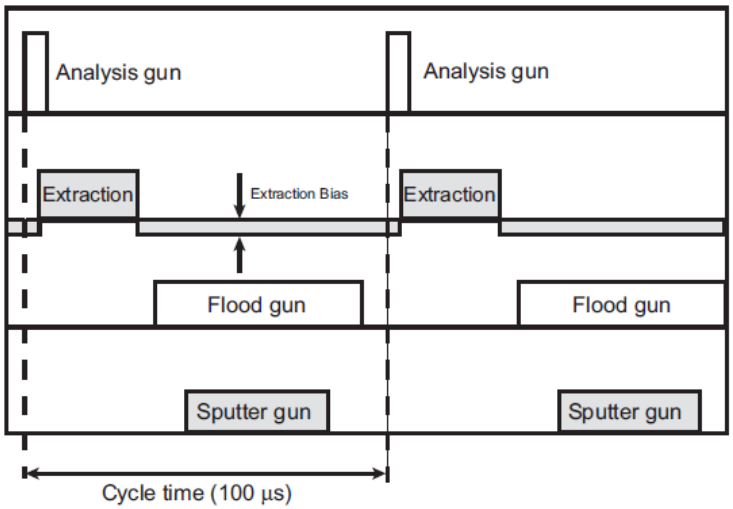

Figure 2.2.3 – *ToF-SIMS repetition rate*

Compared with the sputtering ion beam, the current density in the analyzing ion beam is very low (<1%). Therefore surface effects induced by the analyzing ion beam such as, for example, atomic mixing, can be neglected and the matrix composition as well the as depth resolution are controlled predominantly by the characteristics of the sputtering ion beam: the chemical nature or the mass of the bombarding species, their energy and the angle of incidence. In dual beam mode, these parameters can be optimized without any influence on the analyzing beam allowing an optimum depth resolution.

Another TOF feature that can be applied in depth profiling is the parallel data acquisition. For each pulse of the analytical ion beam an entire mass spectrum is acquired and all the secondary ion signals are recorded, with their *x, y* position, in one single file. This raw data file can be subsequently used to reconstruct:

- the depth profile for any peak in the spectrum.
- the complete spectrum in any depth of the sample.
- the lateral distribution for any peak at a selected depth.

By this means, the mass intervals to be followed as a function of depth can be selected after the measurement and no mass line of interest can be overlooked. Furthermore, the raw data acquisition is very useful for the analysis of the interfaces, because after the acquisition of a depth profile a spectrum of a selected depth interval can be reconstructed from the raw data [157][158].

In our experiments ION TOF TOF SIMS IV have been employed. We used Ga^+ accelerated at 25 keV and rastered over 50 x 50 μm^2 as analysis beam and Cs^+ accelerated at 0,5 / 1 keV and rastered over 200 x 200 / 250 x 250 / 500 x 500 μm^2 as sputtering beam. As our samples are basically SiO_2 matrix, i.e. insulator matrix, sometimes we compensated charging by means of electron flood gun in order to minimize charging effects.

2.2.3.3 Quantitative depth profiling

Quantitative depth profiling is unquestionably the major strength of SIMS. Universally quantification is understood to be the conversion of a secondary ion current $I(m)^{\pm}$ measured as a function of time t *t*, to a concentration $c(m)$ as a function of depth z.

Time to depth conversion

When the target has only one major component one may expect that the sputter velocity $\dot{z} = dz/dt$ is constant throughout the measurement. In this case a strictly linear relation holds between elapsed erosion time and eroded depth in the sample:

$$z(t) = \dot{z}t \qquad (2.2.2)$$

The value of $\dot{z}$ can be determined in many different ways: from the crater depth Z measured after a bombardment time Z as $\dot{z} = Z/T$, from the time to break through a homogeneous layer of known thickness Z or by any method or determining $\dot{z}$ or Z in situ.

If the composition of the sample under analysis varies strongly with depth the linear time to depth conversion can not be used because the erosion rate is expected to change with the bombarding time. In this case $\dot{z}(t)$ must be determined in situ and the depth scale is derived as:

$$z(t) = \int^t \dot{z}\,(t')dt' \qquad (2.2.3)$$

or $z(t)$ must be determined in situ by a suitable method.

Ion current to atoms concentration conversion

The basic SIMS equation described the secondary ion current $I(m)^{\pm}$ of a species m, is:

$$I(m)^{\pm} = I_p Y(m)^{\pm} \alpha\, c(m) \eta \qquad (2.2.4)$$

where I_p is the primary ion flux, $Y(m)^{\pm}$ is the sputter yield, α is the ionization probability, $c(m)$ is the concentration of m in the surface layer and η is the transmission of the analysis system. As $I(m)^{\pm}$ is proportional to $c(m)$, this equation demonstrates that it is possible to infer the concentration $c(m)$ from its measured secondary ion current $I(m)^{\pm}$. The simplest application of eq. (2.2.4) is to use reference sample $\boldsymbol{R}$ with a known and constant concentration level $c_R(m)$ of the impurity/matrix combination under examination. The concentration of the element m can be calculated as:

$$c(m) = c_R(m) \frac{I(m)^{\pm}}{I_R(m)^{\pm}} \qquad (2.2.5)$$

Where $I_R(m)^{\pm}$ is the secondary ion current of the species m in the reference samples. A better approach is to normalize the impurity signals $I(m)^{\pm}$ first to a matrix ion signal $I(M)^{\pm}$ whenever possible. In this way possible variations of $I(m)^{\pm}$ and, to some extent, of $Y(m)^{\pm}$ cannot affect the calibration anymore. This procedure yields the so-called relative sensitivity factor (RSF) which converts the impurity secondary ion intensity to atom density.

$$RSF = \frac{c_R(m)}{I_R(m)^{\pm}} I_R(M)^{\pm} \qquad (2.2.6)$$

It is also possible to determinate RSF measuring the total doses of D_m impurities inside the sample itself using other techniques like Rutherford Back Scattering or Nuclear Reaction Analysis. In this case, it results that:

$$RSF = \frac{D_m}{\int \overline{I_m^{\pm}(z)} dz} \qquad (2.2.7)$$

Were $\overline{I_m^{\pm}(z)}$ is the normalized ion current of a species m in function of depth z.

2.2.3.4 Si NCs detection

Recently, it has been demonstrated that the study of the evolution of Si_n^- ToF SIMS signals allows to characterize the formation and growth of Si NCs in SiO_2 [159]. Therefore, the Si_n^- signals were identified as a fingerprint of Si NCs allowing to reveal the presence and the location Si NCs s embedded in the SiO_2.

2.2.4 Rutherford Back Scattering Spectrometry

RBS is based on the bombardment of the sample with high energy light ions (typically ^4He ions with energy ranging between 1 and 3 MeV) and the measurement of the energy distribution of the backscattered ions, as schematized in Figure 2.2.4 a) [160]. RBS is nondestructive and is used to determine the masses of the elements present in a sample, their depth distribution

(in a region from 10 nm to a few microns from the surface), their areal density and the crystalline structure. In RBS, ions of mass $M1$, atomic number $Z1$ and energy $E0$ are incident on a solid composed of atoms of mass mass $M2$ and atomic number $Z2$ (Figure 2.2.4 b)). Most of the incident ions lose their energy through interactions with valence electrons and come to rest within the solid. A small fraction (around 10^{-6} of the number of incident ions) undergoes elastic collisions and is backscattered from the sample at various angles, leaving the sample with reduced energy $E1$.

Applying the energy and momentum conservation laws the kinetic factor $K = EO/E1$ can be determined. If $M1 \ll M2$ and if the scattering angle θ_s is close to 180°, then

$$K \approx 1 - \frac{2R(1-\cos\theta_s)}{(1+R)^2} \qquad (2.2.8)$$

Where $R = M1/M2$. This is the key RBS equation. As the kinematic factor can be determined by the measurement of the primary ion energy loss, the unknown mass $M2$ can then be calculated through the kinematic factor. The scattering angle should be as large as possible. It is obviously impossible to detect ions scattered by 180°, but angles from 100° to 170° are commonly used.

RBS spectrum is in the form of counts per channel versus channel number, with the channel number linearly related to the backscattered ion energy. The energy scale is at the same time a depth scale and a mass scale because He ions backscattered deeper in the sample have lower energy and because He ions backscattered from heavier elements have higher energy (i.e. higher channel). This implies some ambiguities in RBS spectra: a light mass at the surface of a sample generates a signal that may be indistinguishable from that of a heavier mass locate within the sample. Additional information about the sample under analysis have to be provided to resolve ambiguities.

In this work, RBS analyses have been performed at Laboratori Nazionali di Legnaro (LNL) in Italy by using 2-MeV $^4He^+$ beams delivered by the 2 MV AN2000 Van de Graaff accelerator. The Rutherford ^{31}P (α,el)^{31}P reaction was used with a scattering angle of 165°–170° in (100)

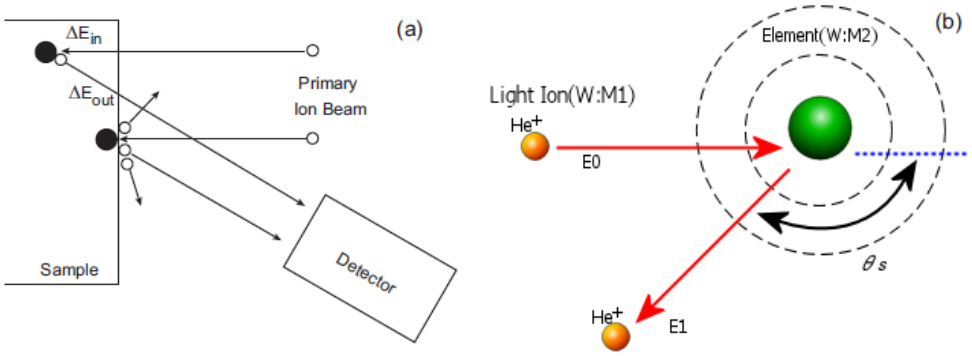

Figure 2.2.4 – a) schematic drawing of RBS principle b) RBS of light ions of mass $M1$, atomic number $Z1$ and incident energy $E0$ from atoms of mass $M2$ and atomic number $Z2$. After the collision the light ions is deflected with a scattering angle θ_s and with reduced energy $E1$

channeling conditions, in order to reduce the Si counts coming from the Si substrate. Total P dose estimations were done by fitting the RBS spectra using an appropriate simulation code considering trial P concentration profiles optimized with thickness constraints based on the P SIMS depth profiles. The P profile in all the samples is shallow enough to have reduced superposition of ^{31}P and ^{30}Si signals in the RBS spectra, allowing relative errors in the P dose estimation in the 6–8% range for most of the samples.

2.2.5 X-Ray Photoelectron Spectroscopy

XPS, also known as electron spectroscopy for chemical analysis (ESCA) is a surface-sensitive quantitative spectroscopic technique that measures the elemental composition, chemical state and electronic state of the elements that exist within a material [161]. In XPS, X-rays incident on a solid interact with core level electrons that can be emitted from any orbital (Figure 2.2.5). The energy of the emitted electrons are then analyzed. A schematic drawing of XPS tool is reported in Figure 2.2.6.

The three basic components of a XPS instrument are the X-ray source, the spectrometer for the electron emitted analysis and a high vacuum system.. The high vacuum requirement comes from the fact that electrons travelling from a sample surface towards the energy analyzer should encounter as few gas molecules as possible, otherwise they will be scattered and lost from the analysis. For the typical dimensions of a spectrometer, this imposes a vacuum requirement of $10^{-5} - 10^{-6}$ mbar, which is not stringent. A better working vacuum level is required in order to avoid the accumulation of contaminants on the sample surface that would modify analysis results. X-ray are generated by bombardment of an anode (magnesium or aluminum) with electrons of sufficient energy, usually they are accelerated through a potential of up to 15 kV. The XPS electrons are detected by one of several types of detector. The hemispherical sector analyzer consists of two concentric hemispheres with a voltage applied between them. A spectrum is generated by varying the voltage so that the trajectories of the electrons with different energies from the sample are brought to a focus at the analyzer exit slit. An electron multiplier is generally used to amplify the signal. Primary X-rays of 1-2 keV energy induce ejection of photoelectrons from the sample surface.

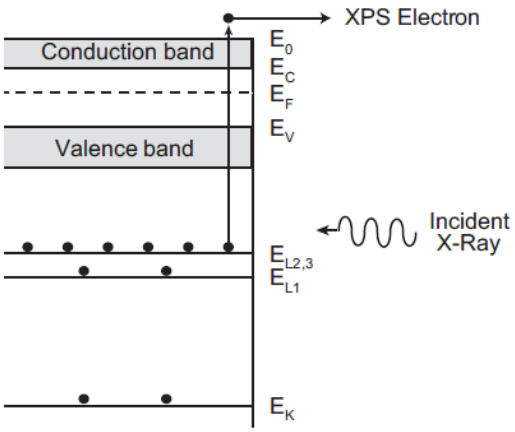

Figure 2.2.5- Scheme of photoelectron effect in XPS

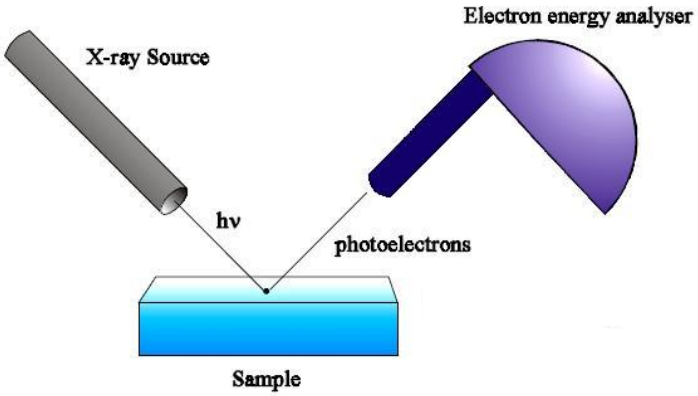

Figure 2.2.6 - Schematic drawing of XPS tool

The kinetic energy E_K of the ejected electron at the spectrometer is related to the binding energy E_B by:

$$E_K = h\nu - E_B - \phi \tag{2.2.9}$$

where $h\nu$ is the energy of the primary X-rays and ϕ the work function. The electron binding energy is influenced by its chemical surroundings making E_B suitable for determining chemical states. This leads to a major strength of XPS: the possibility to identify not only the element, but also its bonding state. Despite the deep penetration of X-rays in the sample XPS is a surface sensitivity method because the emitted photoelectrons originate from the upper 0.5-10 nm of the sample. The effective sampling depth depends on the electron inelastic mean free path $\lambda(E)$ and the on the take-off angle θ with respect to the sample surface. Named z the distance from the surface, the probability $P(z)$ that a photoelectron will escape from the sample without losing energy is regulated by the Lambert-Beer law:

$$P(z) = e^{-\frac{z}{\lambda(E)sen\theta}} \tag{2.2.10}$$

Those photoelectrons that lose energy in leaving the sample will not appear in the characteristic peak but will rather contribute to the background. Note that the electron mean free path depends on the photoelectron energy [162], [163]. The dependence of the photoelectron signal on the take-off angle is the basis of angle resolved XPS technique (ARXPS) that allows to perform depth profiling by sample tilting. Depth profiling is possible also by ion beam sputtering. However sputtering is destructive and can alter oxidation states of the compound being measured. [164][165].

In this work XPS measurements were performed on a PHI 5600 instrument equipped with a monochromatic Al Kα x-ray source (1486.6 eV) and a concentric hemispherical analyzer. The spectra were collected at a take-off angle of 45°-75° with a bandpass energy filter at 11.75 eV. The spectrometer was calibrated using polycrystalline gold, silver, and copper samples.

3 – Results and discussion

This chapter focuses on the main experimental results collected during my thesis work. It is organized in three main sections. The first section reports about the development of the doping technologies that allow obtaining P δ-layer embedded in a SiO_2 matrix. The main target of this part of the work is the optimization of the processing parameters of the different approaches we followed to synthetize the P δ-layer. Quantitative characterization of the dopant sources by ToF-SIMS depth profiles is reported.

The second section focuses on the structural characterization of the Si NCs. A single plane of Si NCs embedded in a SiO_2 matrix was synthetized by high temperature thermal treatment of a SiO_2/SiO/SiO_2 multilayer [80][135]. The main target of this experimental activity is the development of suitable characterization protocols in order to define structural characteristics of the Si NCs and identify the interface between the Si NCs and the surrounding matrix. In particular, we investigated the dependence of the shape, size, and areal density of Si NCs on the thickness of the initial SiO layer, using APT and validated the results by Energy Filtered TEM (EFTEM). This advanced characterization is necessary to define the effective position of dopant impurities and study their incorporation in the Si NCs.

Finally, the third section reports about the experimental results achieved by P *ex situ* doping of Si NCs. The incorporation of P atoms is promoted in Si NCs after their formation, by delivering a controlled amount of dopant atoms from a spatially separated diffusion source. A schematic description of this procedures is shown in Figure 3.0.1. In particular, a systematic study about the doping of Si NCs with 4 nm average size is presented. Experimental data allowed determining the energetics and scheme of P trapping and detrapping within these nanostructures. These results demonstrate that P doping of Si NCs in SiO_2 is thermodynamically favored and that P atoms impurities are stably incorporated within the nanostructures. Moreover, results on the effect of Si NCs size on P incorporation within these nanostructures are reported showing a progressive reduction of the energetic barrier that prevent release from Si NCs. An investigation of the band structure of Si NCs embedded in a SiO_2 matrix as a function of the average diameter of the Si NCs and of the P doses incorporated is present.

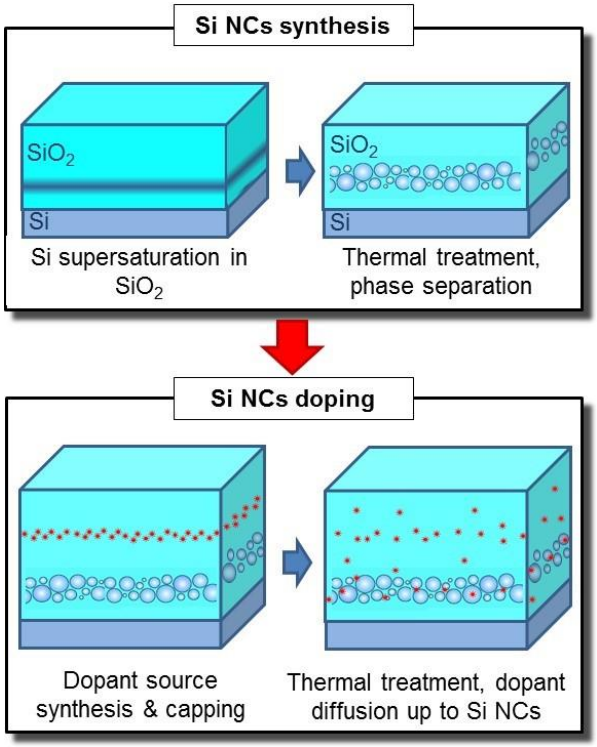

Figure 3.0.1 *– Schematic description of ex situ doping of Si NCs embedded in SiO_2. On the top, synthesis of Si NCs; on the bottom, synthesis of dopant source and dopant diffusion up to Si NCs region*

3.1 Doping sources

To obtain a spatially localized dopant source at a well-controlled distance from the layer of Si NCs embedded in SiO_2 matrix, three different approaches were investigated. To form a P δ-layer in SiO_2, we used an already existing technique, which is based on the evaporation of ultrathin P-SiO_2 films. This approach is described in the section 3.1.1. Afterwards we developed a protocol based on monolayer doping (MLD), that is commonly used for the synthesis of δ-layer of dopant atoms on Si substrate. We tested the validity of this approach on SiO_2 substrate and incorporated the resulted δ-layer of P-containing molecules in a SiO_2 matrix. The results of this experimental exercise are reported in section 3.1.2. Finally, we developed a completely new technique for the synthesis of dopant δ-layer by means of self-assembled monolayers of dopant-terminated polymers. Those results are presented in section 3.1.3.

3.1.1 P-SiO_2 ultrathin films

As already shown in literature, it is possible to create an ultrathin (below 0.5 nm) film of of P-SiO_2 by evaporation o P-SiO_2 in a conventional e-beam evaporation systems [16]. We synthetized P-SiO_2 starting from commercial spin-on dopant solutions purchased from Filmtronics Inc. Efficient removal of the solvent (ethyl alcohol) has been achieved by slow

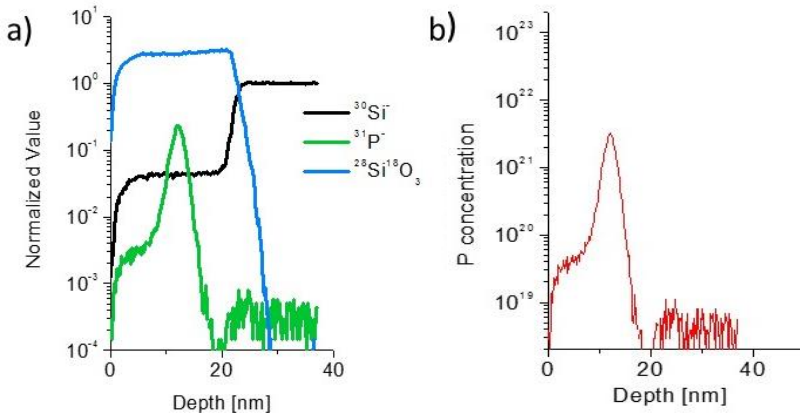

Figure 3.1.1 – a) ToF-SIMS depth profile of SiO_2(~10nm)/P-SiO_2/SiO_2(~10nm) stack deposited on a Si substrate; b) ToF SIMS calibrated P profile of the same sample

evaporation in a rotary evaporation system. The residual solid precipitates are white-transparent P-SiO_2 grains that can be used for e-beam evaporation. For evaporation we use Kurt J. Lesker evaporator. The pressure in the chamber before evaporation was 5 x 10^{-7} mbar. Rotation of the sample during evaporation was performed to enable a high homogeneity over the whole substrate [16]. Ultrathin P-SiO_2 films were deposited over the SiO_2 matrix by properly tuning the processing parameters and subsequently capped by a protective SiO_2 layer.

In Figure 3.1.1 a) ToF-SIMS depth profiles of SiO_2(~10nm)/P-SiO_2(~0.5nm)/SiO_2(~10nm) on Si substrate is reported. ToF-SIMS analyses were performed in a dual-beam ION-TOF IV system in negative mode using Cs^+ ions (0.5 keV, 40 nA, 200 × 200 μm^2 rastering) for sputtering and Ga+ ions (25 keV, 1 pA, 50 × 50 μm^2 rastering) for analysis. The signals intensities have been normalized to the mean value of the ^{30}Si intensity in the Si substrate. $^{31}P^-$ signal refers to P distribution inside the matrix, while SiO_3^- and $^{30}Si^-$ signals are reported to identify the SiO_2 matrix and the Si substrate respectively. The P profile is shallower, with a peak at a depth of 13 nm, with a sharp trailing edge. No P is present on the SiO_2 layer grown on the Si substrate. The long leading tail in the SiO_2 capping layer is an undesired P contamination resulting from a memory effect in the deposition chamber. The full width at half maximum (FWHM) of this peak is less than 2 nm. This value is comparable with ToF-SIMS depth resolution. In Figure 3.1.1 b) ToF SIMS calibrated P profiles of the samples of Figure 3.1.1 a) are reported. The calibration was obtained using standard procedure thanks to RBS measurement of total P doses.

3.1.2 Monolayer Doping

MLD approach consists in the formation of well-defined self-assembled monolayer of dopant-containing molecules bonded to the surface. Usually, the semiconductor surface functionalization takes the form of a thermally-initiated hydrosilylation reaction between a

labile C=C site of the dopant-containing molecule and a hydrogen-passivated semiconductor surface. Because of the self-limiting surface reactions, this process allows the formation of a monolayer of dopant-containing molecules with a regular distribution of the dopant atoms over the surface and a well-defined areal dopant dose [166]. Indeed, improvements in device performances were reported avoiding the conventional random dopant distribution within the semiconductors [167]. Moreover, MLD allows the achievement of damage-free conformal doping on non-planar nanostructures [168] [169] [170]. To date, the formation of monolayers containing different dopants on several semiconducting materials has been demonstrated [171]. Results have been collected both on traditional silicon [156][157] and germanium [162][164] substrates as well as on materials such as III–V compounds [176][177], opening the route to manufacturing application of this doping technique. The most processes for MLD involve wet procedure in which the dopant-containing molecules are used in solution with solvent like mesitylene [178]. Subsequent rapid thermal annealing (RTA) of the self-assembled monolayer of dopant-containing molecules, ensures the dissolution of the molecular structures and the concomitant diffusion of the dopant atoms into the substrate, allowing the formation of sub-5 nm ultra-shallow junctions [173] [172]. All the undesired contaminants coming from the dopant-containing molecules are proved to be localized in the first monolayers below the surface and consequently can be easily eliminated removing a thin sacrificial layer of the semiconducting matrix [179]. Figure 3.1.2 displays an example of a typical MLD process.

Ho *et al*. were the first to report the MLD process, they used allylboronic acid pinacol ester solute in mesitylene to passivate a H-terminated Si surface with a boron-containing molecules [166]. They applied the MLD process to silicon-on-insulator (SOI) substrates in order to fabricate field-effect transistors (FETs). In further work Ho *et al*. [172] report the formation of sub-5 nm ultrashallow junctions in 4 inch wafer-scale obtained by MLD of phosphorus and

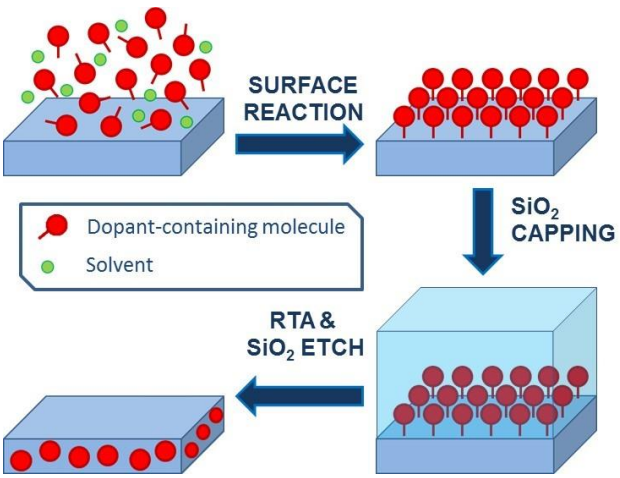

Figure 3.1.2- Schematic diagram of the monolayer doping process for Si substrates. The substrate is reacted with a dopant-containing molecules' solution to form a covalently bonded monolayer. A silicon dioxide capping layer is then formed followed by RTA for dopant diffusion. Finally, the capping layer is removed by HF etching

boron atoms. They found that the majority (∼70%) of the incorporated dopants are electrically active, therefore enabling a low sheet resistance for a given dopant areal dose. A lot of variations of MLD have been proposed. For instance MLD was combined with nano-imprint lithography to control the lateral positioning of dopant atoms over the Si substrate [168]. Hazut *et al.* introduced monolayer contact doping (MLCD) [180]. The main idea of MLCD was the formation of a dopant-containing monolayer on a "donor" substrate, which was then contacted with an "acceptor" substrate. Finally, both substrates were annealed together.

Nevertheless, an important limitation of MLD is the impossibility to finely control the dopant dose without losing the regular distribution of the dopant atoms over the surface. As described above, dopant dose in the monolayer depends entirely on the footprint of the used dopant-containing molecule [166]. To overcome this limitation, Ye *et al.* used a mixed-monolayers approach [181], grafting both dopant- and non dopant-containing molecules on the Si surface. P concentration ranging from 2.4 x 10^{19} atoms/cm^3 to 2.2 x 10^{18} atoms/cm^3 were achieved using this approach. The main drawback of this approach is the impossibility to guarantee uniform coverage of the substrate by the dopant containing molecules.

Furthermore, transferring of MLD process to the microelectronic industry is not straightforward. Actually, MLD requires wet process and long time for surface reaction to take places. These conditionscould be detrimental in view of the integration of MLD in a typical microelectronic process flow [166][172]. Moreover, conventional MLD requires the use of a non-manufacturing-friendly semiconducting substrates (hydrofluoric acid deglazed surfaces) [182]. In this respect, the implementation of MLD processes on manufacturing-friendly substrates becomes important in order to overcome this drawback. In the case of Si-based nanostructures surfaces, the development of a MLD process on SiO_2 is highly desirable, since SiO_2 is ubiquitous in semiconducting devices, at least in the form of native oxide on Si surfaces [180].

After P monolayer doping formation on SiO_2 substrate, samples were capped with SiO_2. In this way, P δ-layers embedded in a SiO_2 matrix and spatially separated from the Si substrates were synthetized. Using a multi-technique approach, the amount of dopants bounded to the surface as a function of the processing conditions has been quantified. Finally, P δ-layer was used as dopant source and the diffusivity of P atoms in the SiO_2 matrix was investigated.

We started from densified SiO_2 substrates prepared by e-beam deposition of 10 nm thick SiO_2 on Si. The entire process for MLD was promoted in clean room because of the reactivity of the molecules involved. MLD is obtained using diethyl 1-propylphosphonate (DPP, Alfa Aesar, purity 97%) as P-containing molecules and mesitylene (Alfa Aesar, purity 98+%) as a solvent. According to theoretical calculations, this P-containing molecule has an areal footprint of 0.12 nm^2. Assuming a fully formed monolayer, a maximal areal dose of 8.3 x 10^{14} atoms/cm^2 is expected. The samples were immersed in a solution of mesitylene and DPP (25:1) and subsequently thermal processed. Processing time (t_p) ranged from 15 min to 6 h, while processing temperature (T_p) was settled either at 100 °C (the boiling point of water) or at 165 °C (the boiling temperature of the solution). After the δ-layer formation the samples were loaded in e-beam deposition and capped by 10 nm thick SiO_2. ToF-SIMS analyses were performed in a dual-beam ION-TOF IV system in negative mode using Cs^+ ions (0.5 keV, 40 nA, 200 × 200 μm^2 rastering) for sputtering and Ga+ ions (25 keV, 1 pA, 50 × 50 μm^2 rastering) for

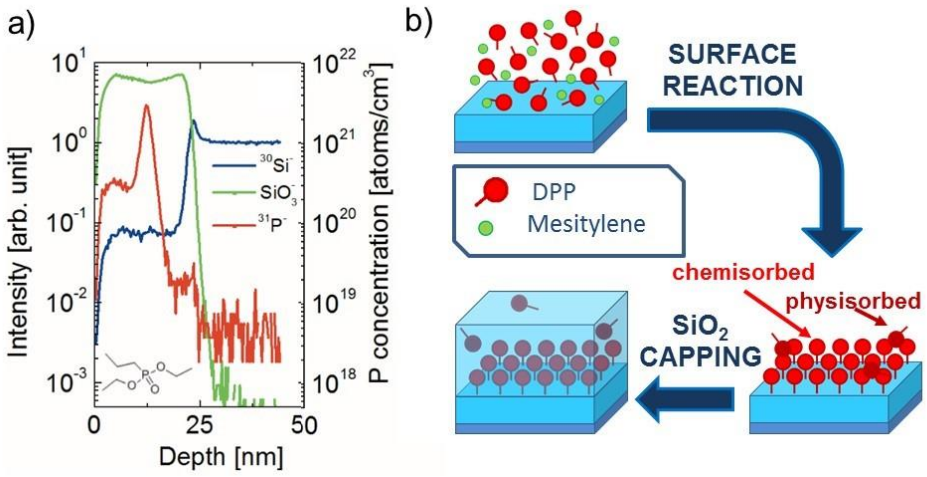

Figure 3.1.3 *– a) ToF-SIMS profile of a P δ-layer embedded in the SiO_2 matrix, showing the presence of a physisorbed contamination diffused in the SiO_2 capping layer. Sample was prepared by MLD process as described in b)*

analysis. Quantification of ToF-SIMS P depth profiles was obtained using standard procedure thanks to RBS measurement of total P doses.

In Figure 3.1.3 a) ToF-SIMS profile of a sample processed at 165 °C for 2 h is reported. A schematic description of this process is reported in Figure 3.1.3 b). Quantified $^{31}P^-$ signal (right axis) refers to P distribution inside the matrix, while normalized SiO_3^- and $^{30}Si^-$ signals (left axis) are reported to identify the SiO_2 matrix and the Si substrate respectively. $^{31}P^-$ signal has been quantified using an RSF determined thanks to RBS analysis of the samples, as described before. A very sharp $^{31}P^-$ peak is detected at about 10 nm from Si/SiO_2 interface with a long leading tail extending towards the SiO_2 surface. The full width at half maximum (FWHM) of this peak is less than 2 nm. This value is comparable with ToF-SIMS depth resolution for this analysis. P dose inside the δ-layer was estimated integrating the $^{31}P^-$ signal in a region extending 2.5 nm around the peak maximum and resulted to be 8 x 10^{14} atoms/cm^2. P contamination inside capping layer was quantified as well, and was found to correspond to a P dose around 2 x 10^{14} atoms/cm^2. The homogeneity of the total P dose was estimated by ToF-SIMS analyses performed in more than ten different points over the sample surface. The evaluation of the standard deviation for this set of analyses leads to an homogeneity of the total P doses worse than 20%, *i.e.* much larger than the expected instrumental error. It is worth to note that this inhomogeneity is strictly related to the variability of the long leading tail extending towards the SiO_2 surface. The contamination of the SiO_2 capping layer is tentatively attributed to physisorbed molecules weakly bonded to the surface after the δ-layer formation. During the SiO_2 capping layer deposition this physisorbed component diffused inside the deposited layer due to kinetic bumping with SiO_2 molecules, leading to the contamination of the entire capping layer. The variability of the P dose in the capping layer suggests that the physisorbed molecules are not distributed homogenously on the SiO_2 surface. In order improve the reproducibility of the process and to minimize the physisorbed

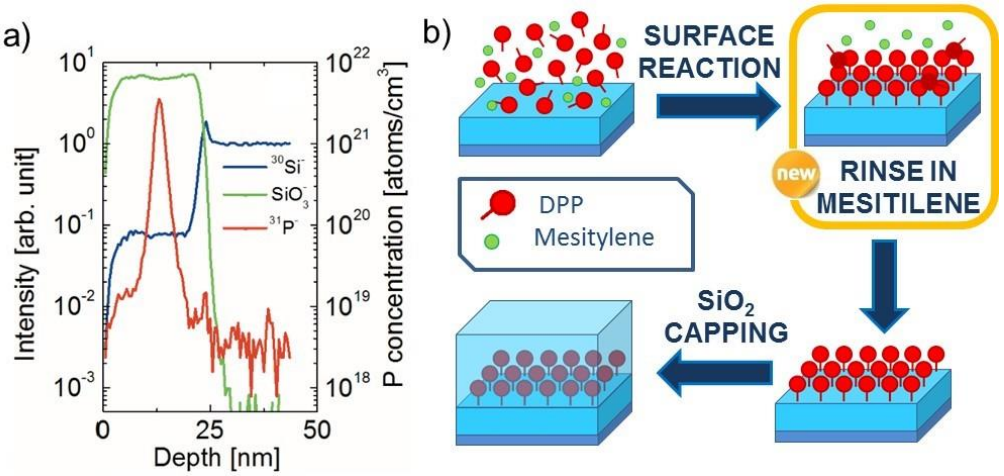

Figure 3.1.4 – a) ToF-SIMS profile of a P δ-layer embedded in the SiO_2 matrix, showing the absence of a physisorbed contamination in SiO_2 capping layer. Sample was prepared using a modified MLD process including rinse in mesytilene after surface reaction, as schematized in b)

component, a new step was introduced in the MLD process, corresponding to a rinse in pure mesitylene at 165 °C for 20 min. A schematic description of the new process is reported in Figure 3.1.4 b). This rinse effectively dissolved the physisorbed component, leading to a $^{31}P^-$ profile (Figure 3.1.4 a)) characterized by no evidence of P contamination in the SiO_2 capping layer. Interestingly the homogeneity in this sample was found to be better than 8%. The removal of the P contamination further corroborates the hypothesis that leading tail observed in ToF-SIMS profiles is related to the presence of physisorbed molecules.

The present results clearly highlight the importance of a proper cleaning procedure of the samples in order to finely tune the amount of P-containing molecules effectively bonded to the SiO_2 substrate. Accordingly, all the data presented hereafter were acquired on samples rinsed in warm solvent before the capping layer deposition.

In order to study the dynamic of the self-limiting reaction between the DPP molecules and the SiO_2 surface, we prepared different samples changing the processing parameters (T_p, t_p). In Figure 3.1.5 a) quantified $^{31}P^-$ depth profiles are reported for samples processed at T_p = 165 °C and t_p ranging from 15 min to 4 h. Maximum P concentration progressively increases with t_p, up to a maximum value corresponding to 3.5 x 10^{21} atoms/cm^3. The degradation of the P-containing molecules was observed at this T_p value for processing times longer than 4 h (not shown). The homogeneity of P dose inside the δ-layer was investigated for each sample repeating ToF-SIMS analysis on different sites, mapping the entire sample surface. Figure 3.1.5 b) reports all the measured P doses inside the δ-layer for each sample. For each t_p we calculated the average P dose. The horizontal shaded areas in Figure 3.1.5 b) correspond to the standard deviations for the different measures performed on the same sample. The homogeneity is always better than 10%, irrespective of the t_p values.

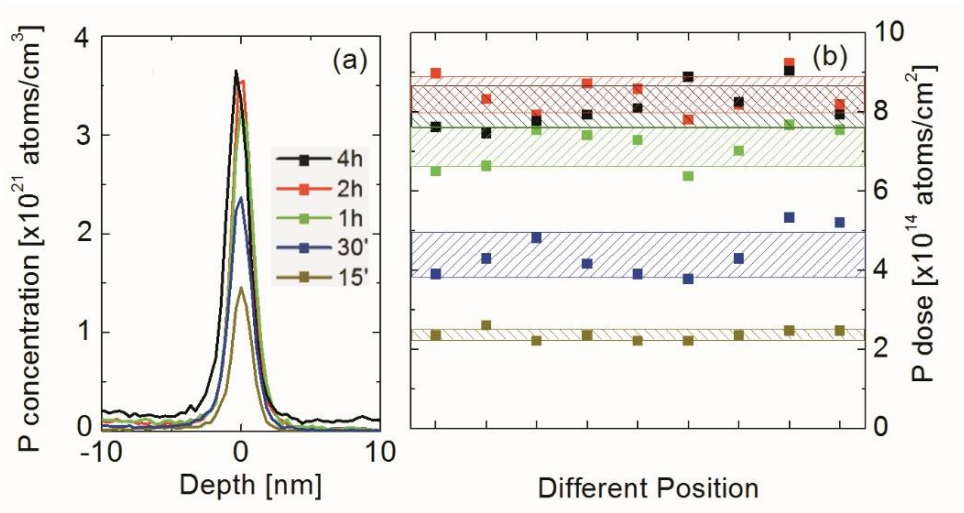

Figure 3.1.5 - ToF-SIMS quantified analysis on a set of samples processed at 165 °C for different time. a) ToF-SIMS quantified profiles of P δ-layer in SiO_2. b) P doses inside monolayer for different site on the samples. The horizontal shaded areas correspond to the standard deviations for the different measures performed on the same sample

Figure 3.1.6 reports the average P doses inside the δ-layer (blue points) as a function of t_p, for the samples treated at T_p = 165 °C. The error bars on each point correspond to the standard deviation from the average values. The maximal doses is reached after t_p = 2 h and corresponds to 8.4 x 10^{14} ± 5 x 10^{13} atoms/cm^2, in perfect agreement with the expected saturation values.[166] This saturation behavior provides a clear indication of a self-limiting reaction in which the saturation value is determined by the molecular footprint. The experimental data were fitted by the following exponential law, which corresponds to the solution of the diffusion-reaction equation describing the δ-layer formation on the substrate:

$$N(t_P) = N_{max}(\,1 - e^{-t_P/\tau}\,) \qquad (3.1.1)$$

where N(t_p) is the dose, t_p the processing time in hours, and τ is the characteristic time of the reaction. N_{max} is the saturation value that was fixed at 8.3 x 10^{14} atoms/cm^2 for this molecule according to theoretical calculations [166]. We obtained a τ value of 1.4 ± 0.1 h from the fitting procedure. The small values of the standard deviations suggest that it is possible to finely tune P dose inside the δ-layer by properly adjusting t_p. Nevertheless, it is worth to remind that when the effective P dose is lower than the saturation-value, the regularity of P distribution at the atomic scale can not be guaranteed.

A similar study was performed by processing the samples at T_p = 100 °C. In Figure 3.1.6 the average P doses inside the δ-layer (red points) are reported as a function of t_p, for the samples treated at T_p = 100 °C. Differently from the case T_p = 165 °C, P doses inside the δ-layer are constant for t_p values up to 6 h. The red line in Figure 3.1.6 corresponds to the fitting of this set of data by means of Eq. (3.1.1), considering N_{max} and τ as free parameters. From this fit

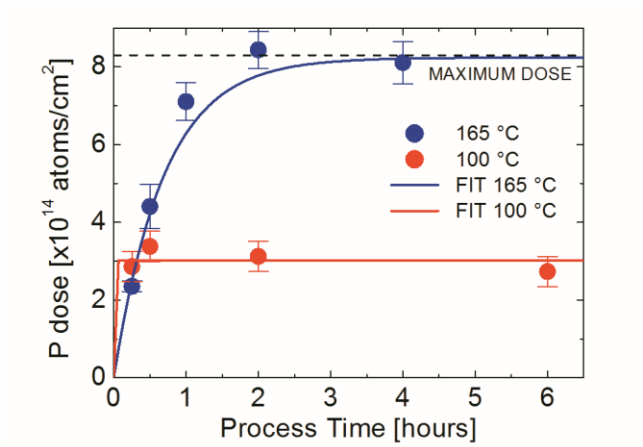

Figure 3.1.6 - P average doses in the monolayer as a function of process time for process at 165 °C a) and at 100 °C b)

we extracted a maximal dose value of 3.1 x 10^{14} atoms/cm^2 that is significantly lower than the value obtained at T_p = 165 °C. This difference could be related to the presence and/or the generation of reactive site on the SiO_2 substrate during the thermal processing. It is worth to say that the maximal P dose in the δ-layer depends both on the molecular footprint and on the availability of reactive sites on the surface. In case of the process at T_p = 165 °C, considering the molecular footprint, the full coverage of the surface is reached suggesting that at this T_p there are no limitations due to the number of active sites present on the surface. Conversely for T_p = 100 °C the maximal P dose indicate that a full coverage of the surface can not be reached irrespective of t_p. These data suggest that all the reactive sites available on the surface are saturated and that the reaction is essentially limited by the availably of reactive sites on the SiO_2 substrate.

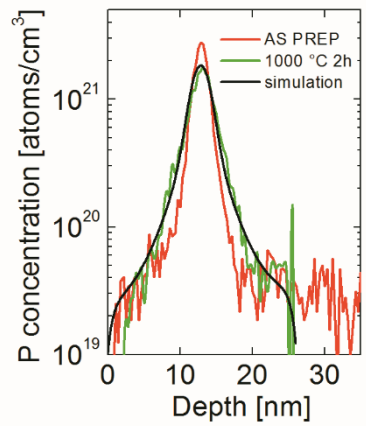

Figure 3.1.7 - ToF-SIMS P depth profiles of a sample as prepared (red) and after a thermal annealing in furnace at 1000 °C for 2 h (green) in N_2 atmosphere and simulation fitting of the latter profile (black)

Figure 3.1.7 reports ToF-SIMS profiles of a sample (T_p = 165 °C, t_p = 2 h) before (red) and after (green) thermal annealing in tubular furnace at 1000 °C for 2 h in N_2 atmosphere. Quantified $^{31}P^-$ signals provide clear evidence of P atom diffusion in the SiO_2 matrix. In order to extract P diffusivity value, ToF-SIMS profiles of these samples were simulated by 1D rate equation modelling of P diffusion in SiO_2, and optimized by means of chi-square minimization algorithm. Black line in Figure 3.1.7 corresponds to simulation fitting of the ToF-SIMS profile of the annealed sample. Black line reproduces very well the experimental data, suggesting that the monolayer doping P source can be treated as standard P source for diffusion in SiO_2. In order to optimize this simulation we have to assume that P diffusivity is constant inside SiO_2 and that it has a minimum in the P peak region. The lower P diffusivity values nearby the P δ-layer region takes into accounts the effusion capacity of P atoms from the source. P diffusivity inside SiO_2 results to be about 1.5 x 10^{17} cm^2/s, in perfect agreement with P diffusivity value in SiO_2 reported in the literature [15]. For more detail about the model for P diffusion refer to subsection 3.3.2.3.

In conclusion, we synthetized P δ-layers embedded in a SiO_2 matrix by MLD process. We proved the self-limiting behavior of the grafting process when processing the samples at T_p = 165 °C, provided that a rinse step in warm solvent is done before the capping layer deposition. We demonstrated that in this case the maximum P dose inside the δ-layer is strictly related to the footprint of the dopant-containing molecules. Conversely, when processing the samples at T_p = 100 °C, the maximum P dose inside the δ-layer seems to be limited by the availability of reactive sites on the SiO_2 substrate. The possibility to use these P δ-layers as diffusion sources was demonstrated as well.

3.1.3 P-terminated homopolymers

OH terminated homopolymers have been deeply studied in the literature [183]–[185] and their properties are well known. These homopolymers react with a substrate via a self-limited reaction, forming a polymeric brush layer grafted to the surface. The density of polymeric chains grafted to the surface (Σ) depends on the chain's footprint. Smaller chains have smaller footprint, so higher grafting density [184]. The value of Σ is directly related to the molecular weight (M_n) of the polymeric chain and to the thickness (H) of the grafted layer by the following expression:

$$\Sigma = \frac{H\,\rho N_a}{M_n} \qquad (3.1.2)$$

where ρ is the homopolymer density and N_a is Avogadro's number. The homopolymers used in this work differ from the ones studied in literature because of their termination. We used poly (methyl methacrylate) (PMMA) and polystyrene (PS) homopolymers terminated with six-diethylphosphate, i.e. with the P-containing molecules that was used for MLD experiments. Each polymeric chain was terminated with six-diethylphosphate molecule. The structure of the P-terminated PS homopolymers is reported in Figure 3.1.8. These molecules contain exactly one P atom each. P-terminated PS and P-terminated PMMA with different M_n were synthetized. For the P-terminated PS, M_n ranges from about 1.9 Kg/mol up to 25 Kg/mol, while for the P-terminated PMMA it is from 8.5 Kg/mol or 14.0 Kg/mol. Detailed information on the homopolymers characteristic is reported in Table 3.3.1. More detail about the synthesis and characterization of these molecules are reported in ref. [186]

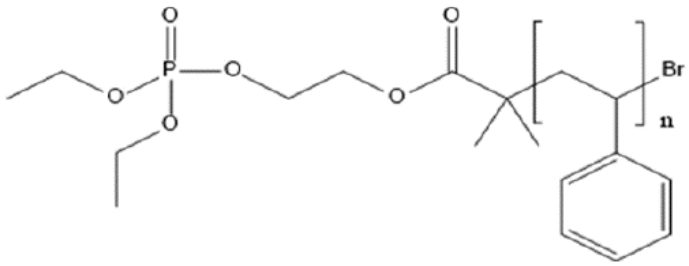

Figure 3.1.8 – *Structure of* P-terminated PS

.

Name	Monomer	M_n [g/mol]
MM17	PMMA	8500
MM6	PMMA	14000
FS13	PS	1853
FS12	PS	1953
FS14	PS	2783
FS5	PS	5383
FS6	PS	14273
FS2	PS	25433

Table 3.1.1 – *Composition and molecular weight, (M_n) of the P-terminated homopolymers that were used in this experimental work*

The process for synthesis of a P δ-layer using this P-terminated homopolymers involves essentially three steps: substrate surface preparation, homopolymers grafting and polymeric chain removal, the entire process was performed in clean room ambient. Process flow is schematized in Figure 3.1.9. We used different substrate: densified SiO_2 substrates prepared by e-beam deposition of 10 nm thick SiO_2 on Si (100) as well as Si (100) samples covered by native oxide.

Substrate surface preparation: The samples were treated with Piranha solution (H_2SO_4 and H_2O_2 in a 3:1 ratio) at 80 °C for 40 min. Piranha solution removes all organic impurities on the samples surface. Moreover, it increases the density of hydroxyl groups at the surface, promoting homopolymers grafting. In order to remove all the piranha residues, the samples were then rinsed in H_2O, dried in N_2 flow and then processed in an ultrasonic bath using 2-

propanol. After this stage the SiO_2 layer was measured by SE in order to have a reference value.

Homopolymers grafting: 9 mg P-terminated PMMA (PS) homopolymers were dissolved in 1 ml of toluene. The solution was then deposited on the samples covering the entire sample surface. Samples were individually spinned in a spincoater at 3000 rpm for 30 s. The thickness of the polymeric layer deposited on the substrate was measured by SE. Polymeric layer thickness varies between 25 nm and 32 nm, depending on the homopolymer M_n. In order to promote polymeric chains anchoring to the SiO_2 surface through the exposed OH groups, samples were thermally treated in RTP machine at 250 °C for 15 min in a N_2 ambient. Samples were processed in an ultrasonic bath in toluene to remove the ungrafted polymeric chains and dried in a N_2 flow. The final grafted polymeric layer thickness was measured by SE.

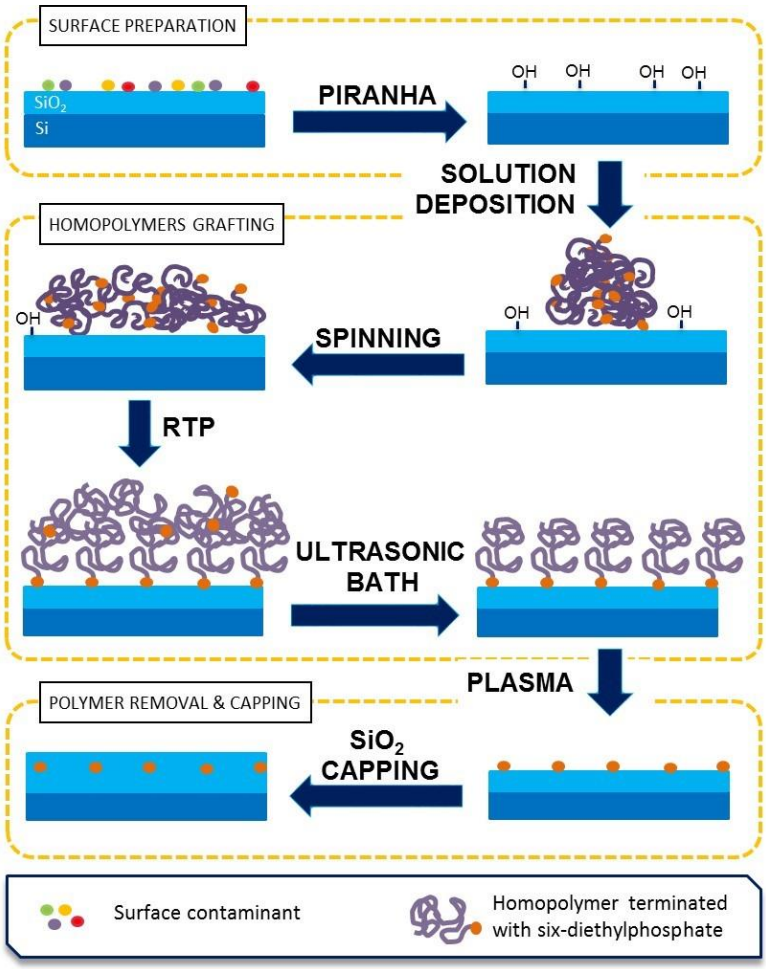

Figure 3.1.9 - Process flow for synthesis of monolayer using homopolymers terminated with six-diethylphosphate

Polymeric chain removal: Finally, to remove the polymeric chains and leave on the substrate only the P-containing molecules grafted on the SiO_2 surface, O_2 plasma hashing was performed. Treatments with different timing in 40 W plasma power were used, depending on the initial thickness of the polymeric layer.

SiO_2 capping layer evaporation: To protect samples from the impurities present in the atmosphere and to avoid P desorption from the surface, samples were then capped with a 10 nm thick SiO_2 layer deposited by means of e-beam evaporator system operating in vacuum.

Using a multi-technique approach, the amount of dopants bounded to the surface as a function of the M_n of the homopolymers were quantified. Densified SiO_2 substrates were prepared by e-beam deposition of 10 nm thick SiO_2 on Si (100) and subsequently annealed in furnace at 1050°C for 1h. P-terminated homopolymers were grafted on the SiO_2 surface forming a dense brush layer. Samples were capped with 10 nm thick SiO_2 film by e-beam deposition. ToF-SIMS analyses were performed in a dual-beam ION-TOF IV system in negative mode using Cs^+ ions (1 keV, 70 nA, 300 × 300 μm^2 rastering) for sputtering and Ga^+ ions (25 keV, 1 pA, 50 × 50 μm^2 rastering) for analysis. Quantification of ToF-SIMS $^{31}P^-$ depth profiles was performed using a standard calibration procedure. RSF^P_{Sio2} values were used to quantify P depth profiles.

Figure 3.1.10 reports P concentration depth profiles of different P δ-layers embedded in SiO_2 matrix synthetized by means of P-terminated PS homopolymers having different M_n. Very

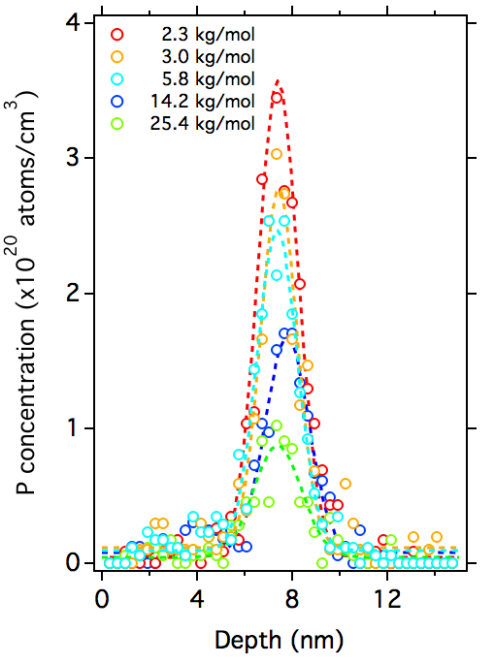

Figure 3.1.10 *- P concentration profiles of P δ-layer embedded in SiO_2 matrix synthetized by grafting P-terminated PS homopolymers with different molecular weights (M_n) on SiO_2 substrate. Decreasing M_n progressive increase of the amount of P in the δ-layer is observd*

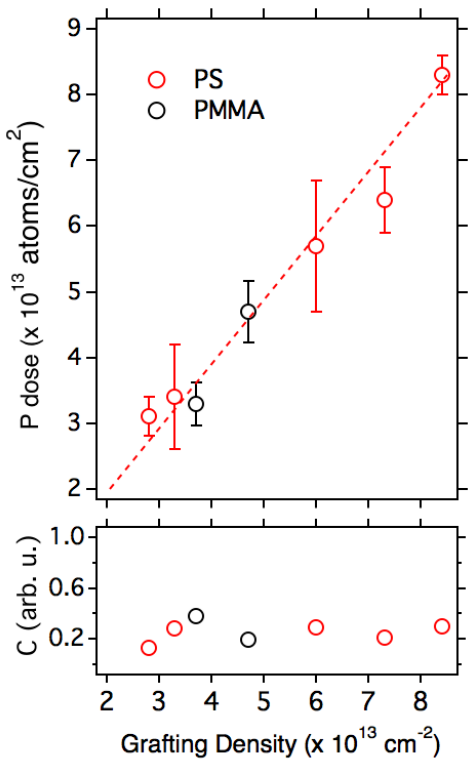

Figure 3.1.11 *– (Top) P dose in the δ-layers as a function of the surface grafting density Σ ; (Bottom) C normalized contamination in the δ-layers as a function of the surface grafting density Σ*

sharp $^{31}P^-$ peaks were detected at about 10 nm from the SiO_2/Si interface. All the peaks were fitted with a Gaussian curve. The full width at half maximum (FWHM) of these peaks is less than 2 nm. This value is comparable with ToF-SIMS depth resolution. This suggests that P atoms are effectively located in a δ-layer at a well-defined position from the SiO_2/Si interface. Maximum P concentration progressively increases as M_n decreases. A maximum P concentration of 3.5 x 10^{20} atoms/cm^3 was reached with M_n= 1850 g/mol. The homogeneity of P layer over the sample was checked by ToF-SIMS analysis in different area of the samples. The ToF-SIMS profiles were observed to be perfectly reproducible with variation of the $^{31}P^-$ intensity that is very limited. Variation in M_n corresponds to variation surface density Σ of the grafted polymeric chains (eq. 3.1.2), leading to a variation of the total P doses in the δ-layers.

P dose inside every δ-layers can be estimated integrating the quantified $^{31}P^-$ signal in a region extending 2.5 nm around the peak maximum. On the top of Figure 3.1.11 it is shown the total P dose in the δ-layers as a function of the surface grafting density Σ, both for P-terminated PMMA an P-terminated PS homopolymers. A maximum dose of 8.3 ± 3 x 10^{12} atoms/cm^2 was obtained with the P-terminated PS homopolymer with M_n= 1850g/mol. The maximum P doses value reached is about ten times smaller than the one obtain using traditional MLD techniques [172][187][179][181]. The experimental data sets for the P-terminated PMMA and

P-terminated PS show a good linear trend, demonstrating the possibility to tune the P dose in the δ-layer by changing the M_n of the grafting P-terminated homopolymers. To obtain information about carbon contamination in the δ-layer, $^{12}C^-$ ToF-SIMS depth profiles were acquired. $^{12}C^-$ profiles were integrated in a region extending 2.5 nm around the P peak maximum. The obtained values were normalized to a reference value, *i.e.* C contamination in δ-layer formed by MLD process. This reference value was calculated in sample synthetized by MLD, integrating $^{12}C^-$ profiles in a region extending 2.5 nm around the P peak maximum. Figure 3.1.11 (bottom) shows the C normalized contamination in the δ-layers as a function of the surface grafting density. Interestingly, the measured C dose in the δ-layer formed by homopolymers results to be constant, irrespective of the M_n values. Moreover, it appears to be lower than 50% of C contamination for MLD. The total C dose in a sample processed by MLD was measured by RBS. It results to be 11 ± 3 x 10^{15} atoms/cm^2. This value corresponds to C contamination usually present on SiO_2 surface due to adventitious carbon deposition on the sample during air exposure.

To obtain P doses higher than 8.3 ± 3 x 10^{12} atoms/cm^2, further reduction of the homopolymer M_n is not a viable solution, since the synthesis of PMMA and PS homopolymers with M_n < 1500 g/mol is difficult from a chemical point of view. An alternative strategy is the iteration of the P δ-layer synthesis process. As known in literature [184][188], the density of active OH sites on the silica surface after piranha activation is much higher than the grafted polymeric chain density Σ. Actually grafting density of 8 x 10^{14} atoms/cm^2 have been demonstrated by monolayer doping on non-treated silica surface [166][189]. This means that after the grafting of the polymeric layer there are still a lot of active sites ready to accept new chains. Further grafting of chains is prevented by steric repulsion with the already grafted ones [184]. In the process-flow for P δ-layer synthesis by homopolymers, the grafted polymeric chains are removed with O_2 plasma. This step exposes the remaining active OH sites that are present on the surface, suggesting the possibility to repeat the process for the δ-layer synthesis. Iterating the process several times, the number of grafted P molecules on the surface is expected to increase after each cycle. Figure 3.1.12 reports P concentration profiles for different iteration of the grafting process of P-terminated PS homopolymer with M_n=1850 g/mol on densified SiO_2 substrates. After each iteration, samples were treated with O_2 plasma for 5 min to remove carbon chains. Finally, samples were capped with 10 nm thick SiO_2 film by e-beam deposition. The P peak intensity progressively increases with the number of iteration. All the peaks have been fitted with a Gaussian curve. The full width at half maximum (FWHM) of these peaks is less than 2 nm. This value is comparable with ToF-SIMS depth resolution for this analysis. This result indicates that during each iteration the homopolymers correctly grafted to the SiO_2 surface.

On the top of Figure 3.1.13, it is shown the P dose in the δ-layers as a function of the number of grafting/plasma cycle for P-terminated PS homopolymers with M_n=1850 g/mol. The P dose linearly increases with respect to the number of cycle. After 5 iterations of the process, a maximum P dose of 3.1 x 10^{14} atoms/cm^2 was reached. The linear fit of the data highlights that P dose increased by the 80% with each cycle. This result indicates that a reduced number of polymeric chains grafted to the surface during the second and following cycles. This is probably caused by the presence of the already grafted molecules, which reduces the number of free OH sites on the surface and thus the probability for incoming homopolymers to graft. Moreover, incoming homopolymers could incorrectly graft to the already grafted P-containing molecules, instead than to the surface, and consequently be removed by the final

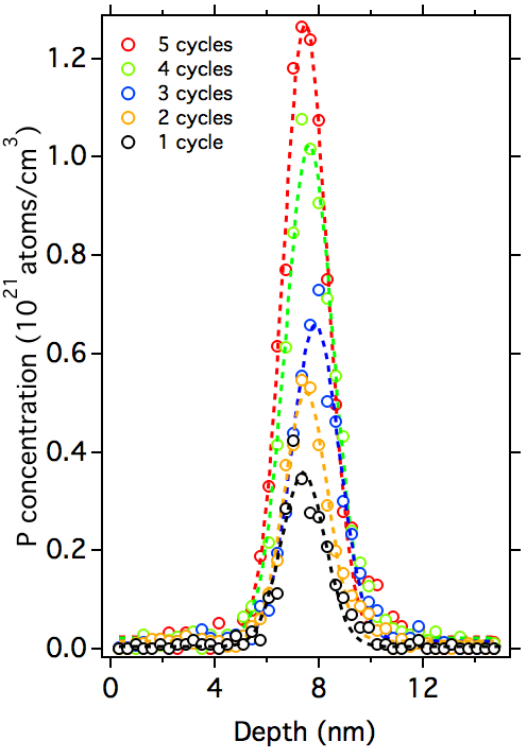

Figure 3.1.12 *- P concentration profiles for different iteration of the grafting process of P-terminated PS homopolymer with M_n=1850 g/mol. Densified SiO_2 substrates were prepared by e-beam deposition of 10 nm thick SiO_2 on Si (100). After P δ-layers formation the samples were capped by 10 nm thick SiO_2 layer by e-beam evaporator. Increasing grafting/plasma cycles progressive increase of the amount of P in the δ-layer is observed*

O_2 plasma hashing. After 5 cycles, no saturation of the process is observed, suggesting that this multi-cycle approach can be exploited even further. However, saturation is expected to occur due to the finite density of active OH sites on the surface. As a matter of fact, this multi-cycle process allows to finely control the P dose in the δ-layer, overcoming one of the main limitation of MLD approach. On the bottom of Figure 3.1.12, it is shown the C normalized contamination as a function of the grafting/plasma cycle. Again the samples exhibit a limited carbon contamination irrespective of the number of grafting/plasma cycles.

P diffusion from dopant source into the Si substrate was studied to investigate the release of dopant impurities from the P δ-layer. P δ-layers were synthetized by grafting P-terminated PS (M_n=1850 g/mol) on the native oxide of a Si (100) substrates. Diffusion was performed by spike annealing (5 s) in RTP. Quantified ToF-SIMS $^{31}P^-$ depth profiles for as deposited and annealed samples are reported in Figure 3.1.14. At annealing temperature lower than 1000 °C, the P atoms cannot diffuse through the thin oxide layer barrier and reach the Si substrate.

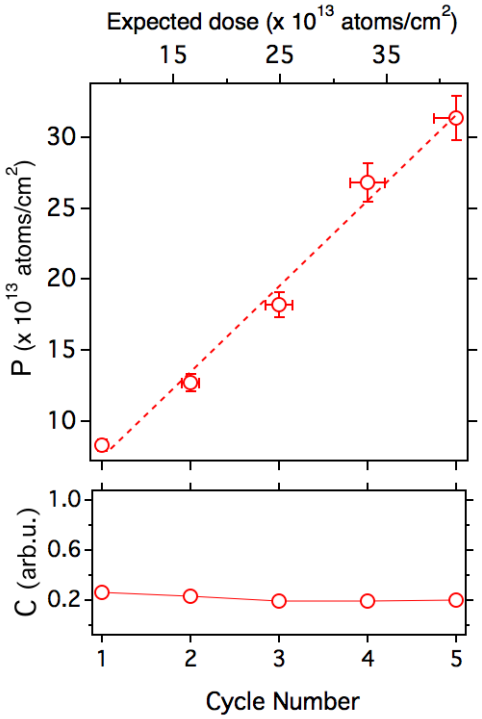

Figure 3.1.13 *– (Top): P dose in the δ-layers as a function of grafting/plasma cycle for P-terminated PS homopolymers with M_n=1850 g/mol; (Bottom): C normalized contamination in the δ-layers as a function of the surface grafting density*

According to literature data [15], P diffusivity in SiO_2 at 1000 °C is 1.5 x 10^{17} cm^2/s, which imply a diffusion length of less than 0.1 nm for a processing time of 5 s. P diffusion profiles were fitted with Gaussian curves fixing background at 1.7 x 10^{18} atoms/cm^3, allowing the estimation of P diffusivities in Si. Conversely, for annealing temperature above 1000 °C, ToF-SIMS depth profiles indicate a clear diffusion of P atoms from the δ-layer into the Si substrate. P diffusivities as a function of temperature were plotted in Figure 3.1.14. These data are in perfect agreement with data in the literature [190]. Considering that the δ-layer P source diffuses in both direction at the same time and assuming a symmetric diffusion in the SiO_2 layer, the maximum achievable injected dose is not higher than half of the starting dose, *i.e.* 4.1 x 10^{13} atoms/cm^2. Integrating P profiles in Si, it results that a maximum of 70% of the initial P dose was injected. This value is similar to those reported for MLD. In conclusion, the possibility to form shallow junctions in Si with total P dose > 2 x 10^{13} atoms/cm^2 was proved, demonstrating the viability of this technology for future nanoscale devices fabrication process.

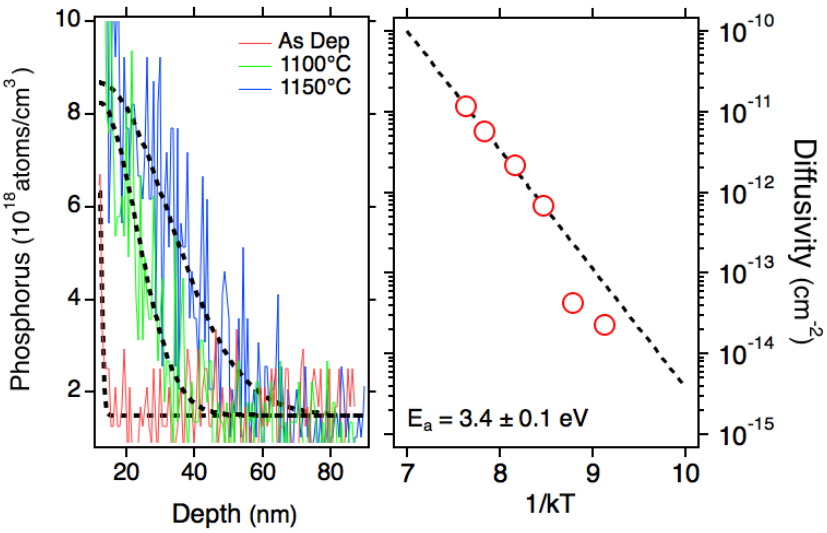

Figure 3.1.14 *– (Left) Quantified diffusion profiles of P into Si substrate for samples as deposited, treated at 1100 °C and at 1150°C, P diffusion profiles were fitted with Gaussian curves allowing the estimation of P diffusivities; (Right) P calculated diffusivities in Si in function of temperature were plotted*

3.2 Structural characterization of Si NCs embedded in SiO_2

Several approaches have been developed to synthesize Si NCs in a SiO_2 matrix by annealing Si rich SiO_2 films in order to promote phase separation and Si NCs formation within the oxide matrix [23][75][141]. In this regard, the approach that we have used in our experiments, i.e. the high temperature thermal treatment of a SiO_2/SiO/SiO_2 multilayer [80][135], is a very efficient method to synthesize a single plane of Si NCs embedded in a SiO_2 matrix. The depth positioning of the Si NCs can be finely tuned by adjusting the thickness of the SiO_2 layers. The average structural characteristics of the Si NCs can be controlled by properly modulating the thickness of the original SiO layer [1][75]. However, as mentioned before, a systematic and comprehensive investigation of the relationship between SiO layer thickness and structural characteristics of the Si NCs is still a challenge due to the intrinsic limitation of current analysis techniques [192]–[198]. Moreover, as efforts have been made in order to exactly define the position of impurities within the nanostructured [14][199], the definition of the effective shape and size of the Si NCs, as well as the correct identification of the interface between the Si NCs and the surrounding matrix becomes more and more important.

In the past studies, TEM techniques such as HRTEM and EFTEM were mainly employed to investigate the structural characteristics of Si NCs [192][193][194][195]. However, HRTEM can only detect the crystallized Bragg-oriented Si NCs. Based on a chemical selectivity, plasmon EFTEM imaging allows to detect both crystallized and amorphous Si NCs. Practically, only 2D maps of the projection of isolated Si NCs or nanoaggregates containing Si NCs are obtained from this method [192][196][197]. Plasmon tomography is necessary to obtain a 3D description, but probably due to instability under irradiation damage very few attempts are

reported in the literature [198]. Moreover, even if a 3D morphology reconstruction can be achieved, it cannot provide a fully quantitative concentration analysis [200].

The state-of-the-art laser-assisted APT which can reconstruct the 3D atom maps of materials is a powerful method to study semiconductors like Si with nearly atomic-scale resolution [179][201][202]. With APT not only the 3D structural characteristics but the inside concentration of Si NCs can be studied [203][204][205]. Moreover, the high sensitivity of the APT allows studying the presence and positioning of the impurities that can modify the electronic and optical properties of the Si NCs. Recently, APT has been employed to investigate dopant incorporation in Si NCs embedded in SiO_2 matrix where Si NCs multilayer samples were used [14][199]. In this respect, the definition of the effective shape and size of the Si NCs, as well as the correct identification of the interface between the Si NCs and the surrounding matrix are crucial to determine the positioning of the impurities within the nanostructured material. In this section we investigate the dependence of the shape, size, and areal density of Si NCs on the thickness of the initial SiO layer, using APT and validating APT results by EFTEM.

A single plane of Si NCs embedded in a SiO_2 matrix was synthesized by annealing a $SiO_2/SiO/SiO_2$ multilayer as shown in Figure 3.2.1 a) and b). The $SiO_2/SiO/SiO_2$ multilayer was deposited on a Si (100) substrate by electron beam deposition. The pressure in the chamber before evaporation was 5 x 10^{-7} mbar. Rotation of the sample during evaporation was performed to enable a high homogeneity over the whole substrate. Then, to trigger the formation of Si NCs, the samples were annealed in a conventional quartz furnace at 1050 ^{o}C for 30 min in N_2 flux. Three samples (marked as sample 1, 2, and 3) with different thicknesses of SiO layer (t_{SiO} = 4, 6, and 10 nm) were prepared.

EFTEM observation was performed on a field emission microscope (TecnaiTM F20, FEI) operating at 200 kV and equipped with an imaging filter (Gatan TRIDIEM). EFTEM images were formed from electrons that passed through the sample and lose energy around 17 eV (±2 eV), which corresponds to the plasmon energy of Si. They were obtained from TEM samples prepared for two complementary observation directions perpendicular to each other (cross-section and plan-view) using the standard procedure involving mechanical polishing and Ar^+ ion milling. For quantitative analysis, the grey-level images were treated to be transformed in black and white images.

In this work needle specimens for APT analysis were prepared by gallium (Ga) focused-ion-beam (FIB), with a FIB-SEM dual-beam system (Helios NanoLab600i, FEI). To allow the fabrication of needle specimens, an additional amorphous Si cap layer of 200 nm was formed on the top surface of sample by a focused ion beam direct deposition (FIBDD) technique, as shown in Figure 3.2.1 c) [23]. To increase the area of interest, the needle specimens were made from the cross-section of the sample as shown in Figure 3.2.1 c). which also avoided the needle fracture during the APT measurements. The samples were sharpened into needles using annular milling patterns with a 30 kV, 0.24 nA Ga^+ beam. To remove the damaged layer from the needle surface, a low ion energy beam (5 kV, 43 pA) was used at the final stage.

APT analysis was performed using a laser-assisted local electrode atom probe (LEAP4000X HR, Cameca). A pulsed laser with a 355 nm wavelength was irradiated upon the needle specimen with a repetition rate of 200 kHz and a laser-pulse energy of 90 pJ. The base temperature of

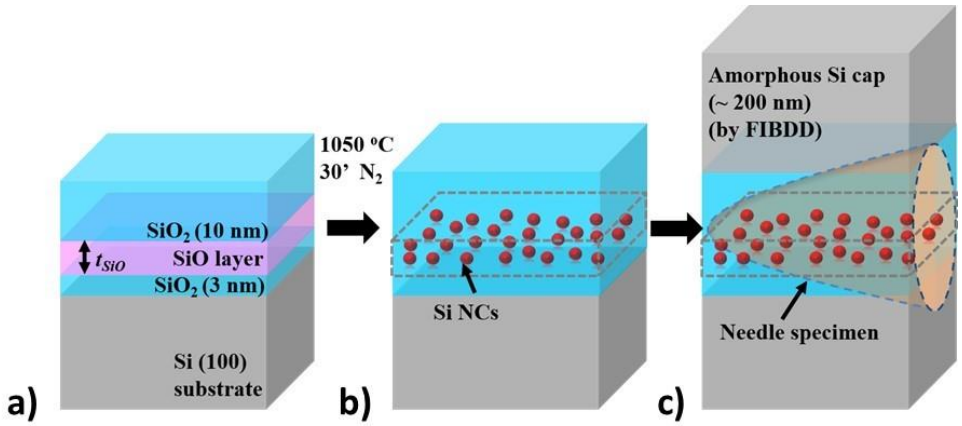

Figure 3.2.1 - Schematic illustration of sample synthesis. (a) SiO_2 / SiO / SiO_2 multilayer deposited on Si (100) substrate. (b) Si NCs monolayer formed after annealing. (c) An additional amorphous Si cap deposited on the top surface of sample and the direction of needle specimen preparation.

the needle specimen during the measurement was 50 K. An Integrated Visualization and Analysis Software (IVAS) protocol was employed to reconstruct the 3D atom map.

Cross-section and plan-view EFTEM images of the three samples are shown in Figure 3.2.2. From the cross-section images reported in Figure 3.2.2 a) - c), the projected Si NCs plane embedded in the SiO_2 matrix can be observed as a bright area over a dark background. In these projections, they form a thin layer whose thickness increases from 2.1 to 4 nm as the initial SiO layer thickness increases from 4 to 10 nm. These single planes of Si Ncs are located at 3 nm from the underlying Si substrate in all the samples irrespective of the SiO layer thickness. In the corresponding plan-view images reported in Figure 3.2.2 d) - f), the projection of the Si.

NCs is uniformly distributed in the plane they form. The Si NCs have a rounded shape with a proportion of elongated Si NCs that increases as the initial SiO thickness increases. To discuss quantitatively this evolution, the grey-level plan-view images were transformed into black and white ones, as printed in Figure 3.2.1 g) - i), from which the mean length, width, area, as well as diameter and areal density (number of Si NCs per unit surface) of the Si NCs were determined and gathered in Tables 3.2.1 and 3.2.2 respectively.

The shape of Si NCs can be represented by the length and width of Si NCs. In the plane, the length of the Si NCs can be described by the geodesic diameter, which is the largest path between two points at the border of the Si NCs. The width is the in-circle diameter, which is the largest diameter of the circle that can be drawn inside the Si NCs. The average values of these parameters evidence that, in the plane they form, the Si NCs become more and more elongated as the initial SiO thickness increases. This can be well seen looking at the "in-plane elongation parameter" (length/width), which varies from 1.6 to 2.0 going from the 4 to the

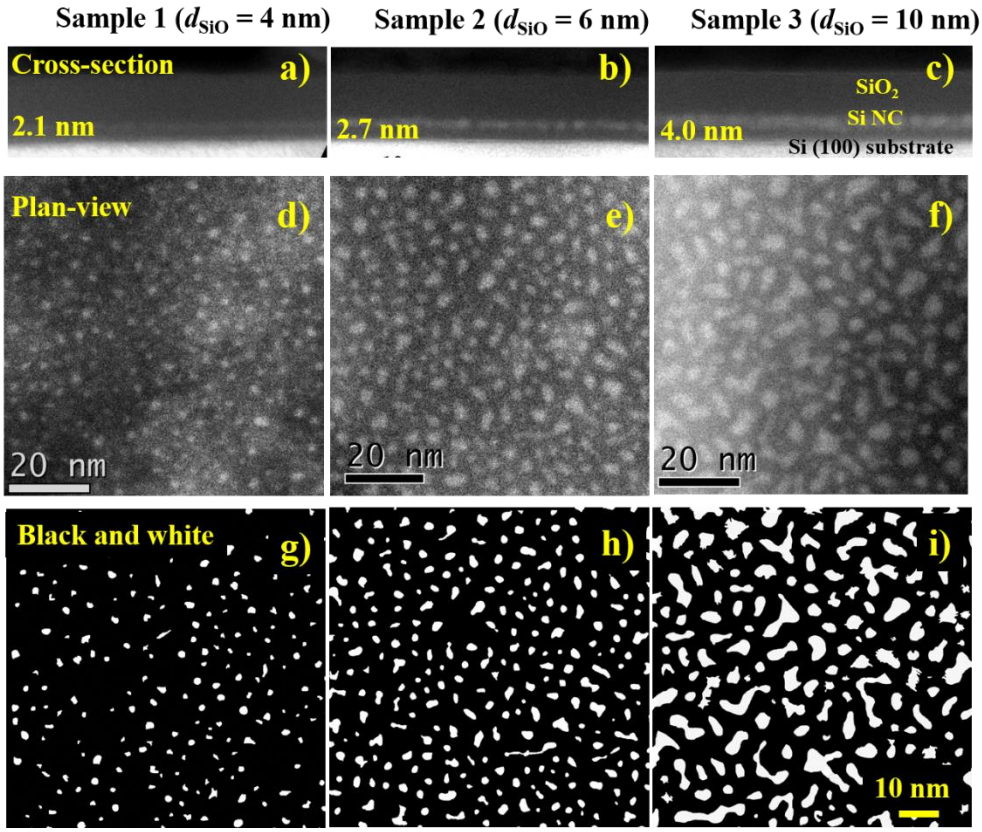

Figure 3.2.2 - Cross-section [a) - c)] and plan-view [d) - f)] EFTEM images of samples 1, 2, and 3. g) - i) Same plan-view images as d) - f) after the black and white transformation

10 nm thick initial SiO layer. In the same time, the "out-of-plane elongation parameter" (length/thickness) increases from 0.9 to 1.3. All the parameters vary rather linearly with the initial SiO layer thickness as seen in Figure 3.2.3. In particular, the width of the Si NCs is always

	Sample 1	Sample 2	Sample 3
Thickness (nm)	2.1 ± 0.5	2.7 ± 0.5	4.0 ± 0.5
Area (nm^2)	1.7 ± 0.9	4.2 ± 2.4	10.3 ± 8.1
Length (nm)	1.8 ± 0.6	3.1 ± 1.3	5.1 ± 2.8
Width (nm)	11 ± 0.3	1.7 ± 0.4	2.5 ± 0.8
Elongation (Length/width)	1.63	1.82	2.04

Table 3.2.1 - The structural characteristic parameters of Si NCs in samples 1, 2 and 3 obtained by EFTEM

Size and number density		Sample 1	Sample 2	Sample 3
Average diameter (nm)	APT	2.2 ± 0.8	3.1 ± 1.6	3.5 ± 1.6
	TEM	1.9 ± 0.5	2.8 ± 1.0	4.3 ± 2.9
Areal density (10^{12} NCs/cm^2)	APT	4.0 ± 0.4	4.2 ± 0.4	1.9 ± 0.3
	TEM	3.0 ± 0.6	3.4 ± 0.7	2.4 ± 0.5

Table 3.2.2 - The comparison of the APT and EFTEM results

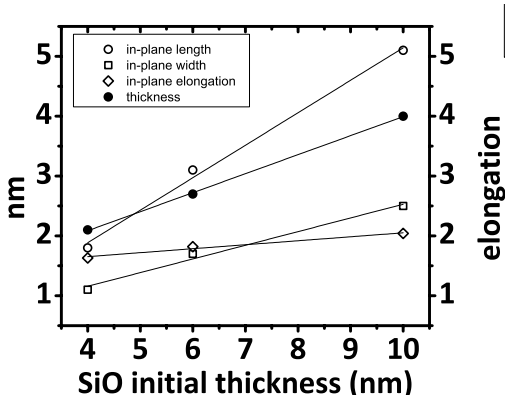

Figure 3.2.3 - Si NCs shape evolution with the increasing of SiO layer thickness

lower than their thickness and increases with a similar slope. On the contrary, the length increases faster than the width and becomes higher than the width of initial SiO thicknesses higher than 6 nm. This means, as a first approximation, that the Si NCs can be described as spheroids using width and thickness to define their equatorial and polar diameters. The experimental data indicate that the spheroids are rather prolate for the initial 4 nm SiO thickness and more and more oblate for thicker and thicker initial SiO layers.

The mean area of the Si NCs (total area occupied by the Si NCs divided by the number of Si NCs within a defined surface) increases from 1.7 to 10.3 nm^2 as the initial SiO thickness increases from 4 to 10 nm. The mean diameter is defined as the diameter of the sphere with a volume equivalent to the mean volume of the NCs which can be approximated from the cross-section and plan-view parameters (thickness and area). The diameter of Si NCs progressively increased from 1.9 to 4.3 nm with the increasing of the initial SiO thickness. In the same time, the areal density remains similar within the error bar for the two first samples but decreases by a factor of 1.5 for the sample with the 10 nm thick SiO layer.

As the EFTEM images only gave the information about the projection of Si NCs, the three samples were further studied by APT to get more insight into the 3D structural characteristics

of Si NCs. Figure 3.2.4 a) shows a 3D atom map of sample 2 where the Si NCs were represented by 70 at.% Si iso-concentration surfaces. The single Si NCs layer embedded in the SiO_2 matrix can be clearly observed in the 3D atom map. A similar structure can be evidenced in the 3D atom maps of samples 1 and 3 (not shown here). The Si NCs in samples 1, 2, and 3 were extracted from the SiO_2 matrix by 70 at.% Si iso-concentration surfaces as shown in Figure 3.2.4 b) - d). In addition to 2D EFTEM, these 3D representations bring essential information on the complex shape and arrangement of the Si NCs. The maps confirm that Si NCs have curved shapes with a large part of elongated ones particularly for sample 3. Details on the stretching of some Si NCs in sample 3 are illustrated in the 2D Si concentration map, as reported in Figure 3.2.4 e), where the formation of elongated Si NCs is caused by the connection of small Si NCs. From a qualitative point of view we observe that the size of Si NCs enlarged with increasing initial SiO layer thickness, and that the areal density decreased in sample 3, which is in agreement with EFTEM data.

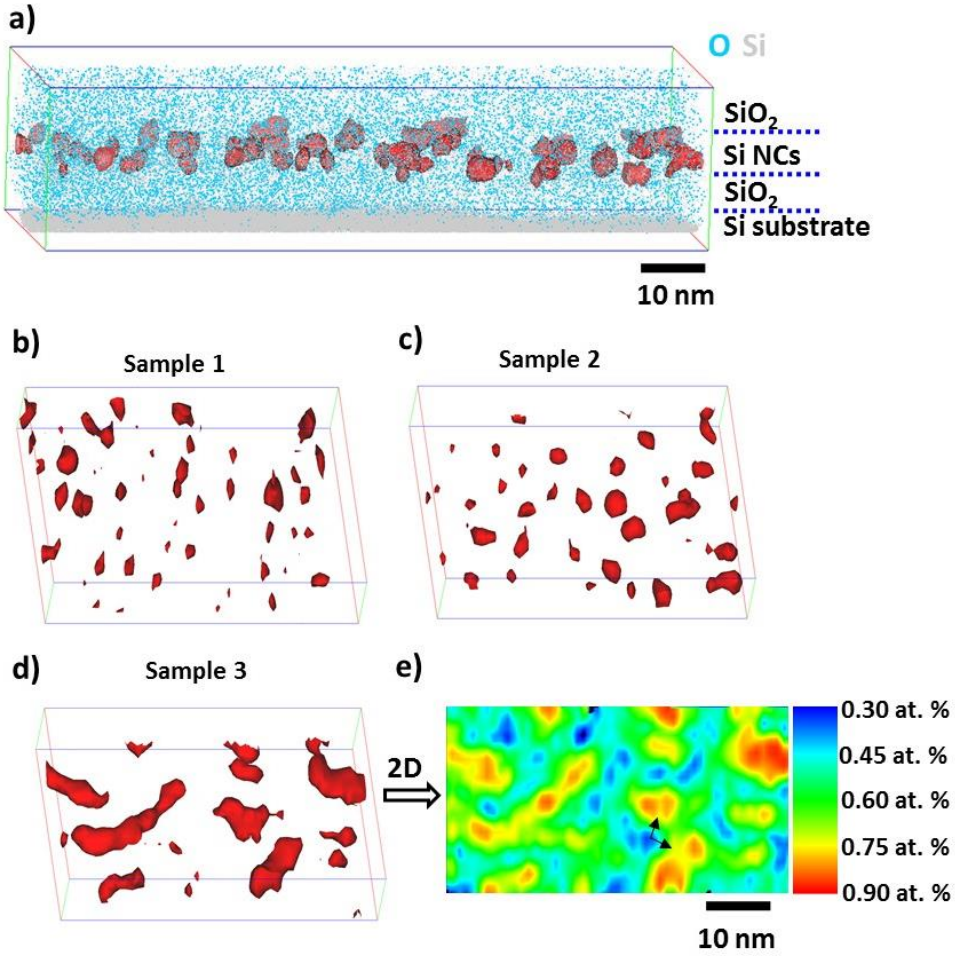

Figure 3.2.4 - a) 3D atom map of sample 2; b) - d) 70 at. %Si iso-concentration surface of samples 1, 2, and 3; e) 2D Si concentration map of sample 3. The connection areas of Si NCs were indicated by black arrows.

Due to the well-known APT artifact, the local magnification effect [203], some SiO_2 was artificially introduced into the Si NCs, which blurred the Si NC/SiO_2 matrix interface. Clear evidence of this effect is shown in the 2D Si concentration map of sample 3, see Figure 3.2.4 e). Same feature are also observed for samples 1 and 2 (data not shown). Therefore, it is difficult to quantitatively evaluate the shape, size, and areal density of Si NCs by using Si iso-concentration surfaces, as the final result is very sensitive to the chosen Si concentration threshold values. In order to quantitatively study these structural characteristics of Si NCs, a cluster identification algorithm has been employed [206][207]. This method is based on the assumption that the distance between solute atoms within a cluster is smaller than that between solute atoms in the matrix. Hence, the solute atoms with distance smaller than a set value (d_{max}) were identified to belong to a same cluster. In addition, a parameter N_{min} is used to determine the minimum cluster size based on the number of solute atoms within a cluster. However, it should be noted that there is no distinct criterion for choosing the proper d_{max} and N_{min}[208][209].

Here the values of d_{max} were determined by comparing the size of Si NCs output from cluster analysis with that roughly estimated from Si iso-concentration surfaces. The d_{max} were finally set as 0.39, 0.39, and 0.43 nm for samples 1, 2, and 3, respectively. The d_{max} values of samples 1 and 2 were approximate to previous report (d_{max} = 0.4 nm)[199], but the d_{max} value of sample 3 was a little higher. That is because in sample 3 many Si NCs were connected with each other, and the Si concentration connection areas is lower than that in the Si NCs as indicated by black arrows in Figure 3.2.4 e). The distances between Si atoms in these low Si concentration areas were larger than that in the Si NCs, so if the d_{max} value is too small, the connected Si NCs will be divided into small ones. To avoid miscounting small clusters and separate clusters from random solid solution, N_{min} were set as 40 atoms for all three kinds of samples by using a size distribution analysis[210]. This N_{min} value corresponding to sphere Si NCs with diameter of about 1 nm which is similar to the lower detection limit of EFTEM.

In the cluster analysis, the Si NCs were fitted as ellipsoids using best-fit ellipsoid method from which the dimension of the semi-axes (s1, s2, and s3) of the best-fit ellipsoid can be determined ($s1 \geq s2 \geq s3$ are the major semi-axes and two minor semi-axes, respectively) [211]. The aspect ratio (s2 / s1) and oblateness (s3 / s2) were used to represent the shape feature of the Si NCs. Figure 3.2.5 a) - c) show the shape distributions in terms of aspect ratio and oblateness. Almost all the Si NCs are distributed in the sphere region in all the three kinds of samples. Compared with sample 2 and 3, Si NCs tend to be more prolate in sample 1 which is consistent with the EFTEM results. Interestingly, in sample 3 there are many rod-shaped Si NCs which were found connected by small Si NCs as what we have observed in Figure 3.2.4 d) and e). The diameters of Si NCs were derived from the volume by treating Si NCs as spheres, and the diameter distributions are shown in Figure 3.2.5 d) - f). The average diameters of Si NCs 2.2 ± 0.8, 3.1 ± 1.2 and 3.5 ± 1.6 nm in sample 1, 2, and 3 respectively. Moreover, there are many very large Si NCs (diameter ≥ 6 nm) in sample 3 and most of them are found to be rod-shaped Si NCs. The areal density of Si NCs were in the order of 10^{12} NCs/cm^2 in all three kinds of samples which is same order with previous reports [212]. In particular the areal densities are 4.0 ± 0.4 × 10^{12}, 4.2 ± 0.4 × 10^{12}, and 1.9 ± 0.3 × 10^{12} NCs/cm^2 in samples 1, 2, and 3, respectively. Both the sizes and areal densities were consistent with the EFTEM results within the error bar as shown in Table 2.3.2.

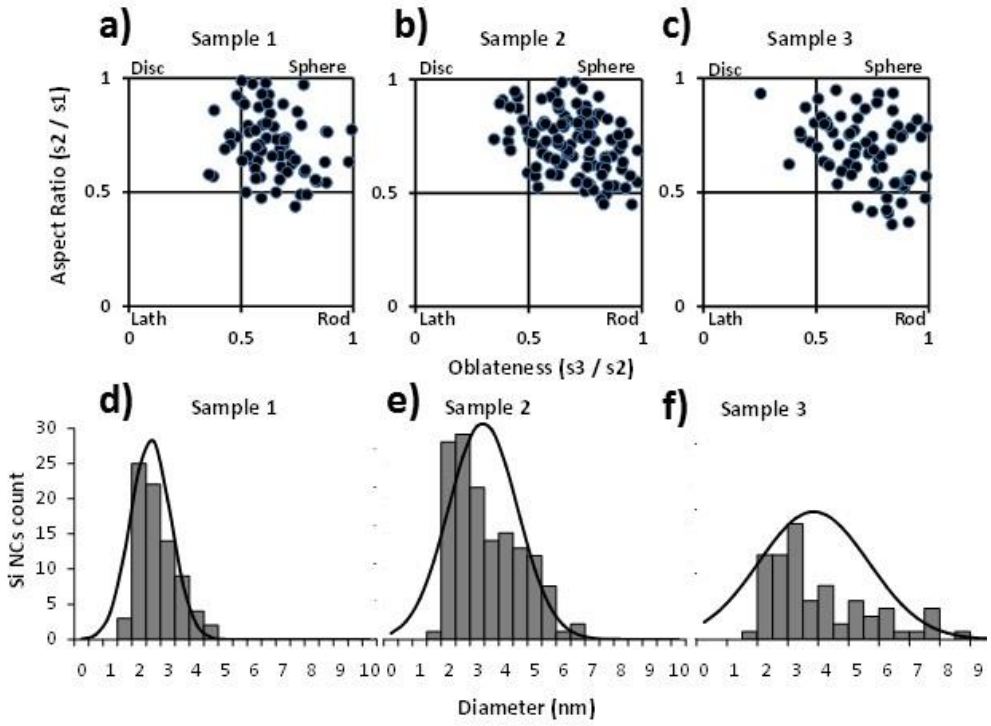

Figure 3.2.5 - Shape [a) - c)] and size [d) - e)] distribution of samples 1, 2, and 3

It should be noted that the areal density in sample 3 is much lower than that in sample 1 and 2. The areal density decrease of Si NCs was often explained by Si NCs coarsening during Ostwald ripening [194][213][214]. However, our results indicated the decrease of areal density is caused by small Si NCs connection. Recently, the kinetic Monte Carlo (KMC) simulation showed that small Si NCs tend to connect with each other when they form~~ed~~ and exist closely [215]. Our APT results are consistent with this KMC simulation.

The proposed combination of APT and TEM analysis provides a complete and exhaustive picture of the system. Previous results demonstrate a very good qualitative agreement between the two techniques [200]. Nevertheless a quantitative analysis of the data was prevented by the structural characteristic of the samples exhibiting a sponge-like Si structure embedded in a SiO_2 matrix. Using a single layer of Si NCs a direct comparison between EFTEM and APT is possible, providing a complete and self-consistent quantitative description of Si NCs morphology. The 3D reconstruction of the Si NCs obtained by APT analysis is validated by EFTEM plan-view and cross-section images. With this methodology the structural characteristics of Si NCs were investigated as a function of the thickness of the initial SiO layer. The experimental results demonstrate that by increasing the SiO layer thickness the Si NCs get progressively bigger with a concomitant evolution of the shape from spheroids to rod shaped nanostructures. Interestingly irrespective of the SiO thickness the Si NCs arrange in a single plane at a well-controlled distance from the Si substrate. In particular, in the sample with the 10 nm thick SiO layer, Si NCs mainly elongate in the in plane direction with limited

effects in the out of plane direction. This result suggests that, in this range of thickness of the SiO layer, the Si NCs formation is strongly constrained by the adjacent SiO_2 barriers, that force the Si NCs to grow in a well defined position inducing the observed shape evolution from spheroid to rod-shape structures.

In conclusion, the dependence of shape, size, and areal density of Si NCs on SiO thickness was investigated by APT which were validated by EFTEM. Three kinds of samples with different thicknesses of SiO layer (t_{SiO} = 4, 6, and 10 nm) were studied. The shape of Si NCs is mainly extended spheroid in all the samples. Si NCs in sample 1 (t_{SiO} = 4 nm) are more prolate than that in sample 2 (t_{SiO} = 6 nm) and 3 (t_{SiO} = 10nm). Moreover, many rod-shaped Si NCs which were connected by small Si NCs formed in sample 3. The increase of the SiO layer thickness triggered the formation of larger Si NCs. The average diameter of Si NCs were 2.2 ± 0.8, 3.1 ± 1.2, and 3.5 ± 1.6 nm in samples 1, 2, and 3, respectively. The areal densities of Si NCs were in the order of 10^{12} NCs/cm^2 in all the samples, but it was much lower in sample 3.

3.3 *Ex situ* doping of Si NCs embedded in SiO_2

This section is dedicated to the results achieved by *ex situ* doping. The main idea behind our approach is the decoupling of Si NCs synthesis from their doping. The incorporation of P atoms is promoted in Si NCs after their formation, by delivering a controlled amount of dopant atoms from a spatially separated diffusion source. In this way, the energetics of trapping/detrapping of P in the NCs are measured at equilibrium and modelled as a function of the annealing temperature and time, avoiding kinetic effects due to NCs formation. Refer to Figure 3.0.1 for a scheme of the entire process.

In section 3.3.1, a systematic study of P doping of Si Ncs with an average diameter of 4 nm is presented. P source for this experiment was synthetize by P-SiO_2 evaporation. In section 3.3.2, results about the effect of Si NCs size on P incorporation is discussed. In this experiment P source was synthetized by MLD.

3.3.1 *Ex situ* doping of 4 nm size Si NCs embedded in SiO_2

Si NCs embedded in thin SiO_2 film were prepared by e-beam evaporation of a SiO_2 (14nm)/SiO (6nm)/SiO_2 (10nm) multilayer structure and subsequent annealing at high temperature (1150°C, 60 min) in a conventional tubular furnace. After annealing, single layer of Si NCs was formed in the SiO_2 matrix. A thin (0.4 nm) layer of P-SiO_2 was then deposited on the top of SiO_2 film and subsequently capped with a 20nm thick SiO_2 layer [216]. To promote P diffusion and trapping in Si NCs without perturbing the equilibrium structure of the Si NCs, thermal treatments were performed at temperature lower than the one used for Si NCs synthesis, *i. e.* from 900° C to 1100° C. A set of similar samples without Si NCs layer was prepared, in order to be used as reference samples for P diffusion in SiO_2.

In order to extract information about the thermodynamic stability of P impurities inside Si NCs different steps were accomplished:

1 – Si NCs characterization: we experimentally verified that the thermal treatment to promote P diffusion didn't affect Si NCs population characteristics, i.e. their average size and their areal density. EFTEM was used to achieve this goal by analysis of the samples before P diffusion and after the higher temperature thermal treatment used to promote P diffusion and incorporation into the Si NCs.

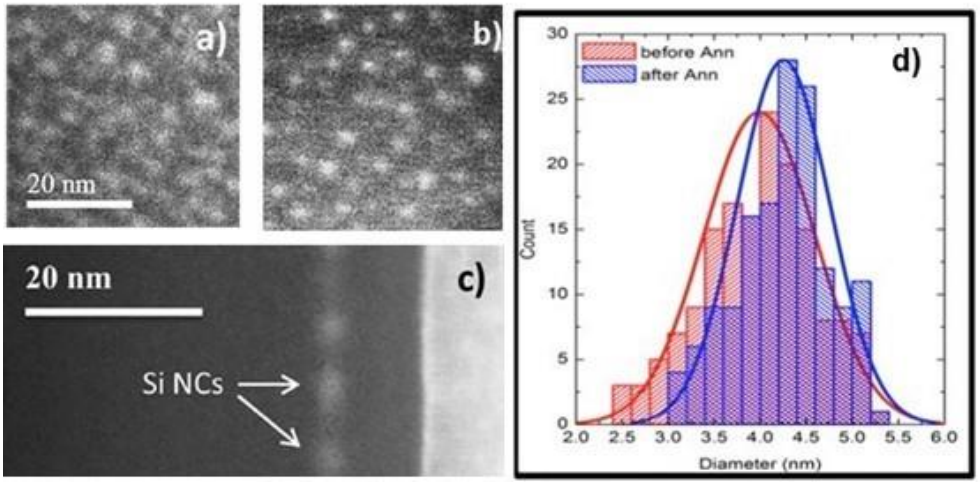

Figure 3.3.1 - a) EFTEM plan view of the as deposited sample and b) of the sample after 1100° C 4h (same scale as a)); c) cross sectional EFTEM image of the sample as deposited; d) NCs size distribution of the as deposited (red) and annealed (blue) sample as obtained from the EFTEM plan view images.

2 – P depth distribution and quantification: different analytical tecniques were combined to achieve information about P diffusion and incorporation into the Si NCs. ToF-SIMS was used to depict P depth distribution inside the matrix. RBS was used to quantify P ToF-SIMS profiles. To achieve this goal, innovative protocol for the quantification of Phosphorous in the Si NCs region was developed. Finally, XPS was used to get information about P chemical environment in the Si NCs regions. XPS data allowed understanding P location of P with respect to the Si NCs.

3 – Modelling of P trapping/detrapping: P depth profiles were modellized using a model based on diffusion Fick's law in one dimension. Energy scheme of the system and P binding energy inside Si NCs were depicted by the comparison between the model and experimental results.

3.3.1.1 Si NCs characterization

Figure 3.3.1 reports the EFTEM plan view (a) and cross sectional view (c) of the sample after the synthesis of Si NCs and the deposition of P layer and SiO_2 capping layer. These samples were named "as deposited". From the plan view images, we measured an average diameter of (4.0 ± 0.6) nm and an average areal density (*N*) of 1.3 x 10^{12} dots/cm^2. The cross sectional image indicates that the Si NCs are aligned in a 2-dimensional layer with thickness of (3.9 ± 0.6) nm and a well controlled distance from the Si substrate. Figure 3.3.1 b) reports the EFTEM plan view of the samples after 1100° C 4h, the scale is the same of Figure 3.3.1 a). From these images, we measured an average diameter of (4.2 ± 0.5) nm and an average areal density (*N*) of 1.5 x 10^{12} dots/cm^2. Figure 3.3.1 d) reports the size distribution corresponding to plan view images of both the samples. As could be appreciate from these data, Si NCs structure was not affected by thermal treatment that promote P diffusion.

3.3.1.2 P depth distribution and quantification

Figure 3.3.2 reports ToF-SIMS $^{30}Si^-$,$^{31}P^-$, $^{28}Si_2^-$ and $^{28}Si^{18}O_3^-$ signals normalized at $^{30}Si^-$ average value in SiO_2 matrix. ToF-SIMS analyses were performed in a dual-beam ION-TOF IV system in negative mode using Cs^+ ions (1 keV, 90 nA, 500 × 500 µm^2 rastering) for sputtering and Ga+ ions (25 keV, 1 pA, 50 × 50 µm^2 rastering) for analysis. The $^{31}P^-$ profile (green line) has a shallow peak at a depth of 22 nm well separated by the NCs zone, with a trailing edge due to residual P atoms in the deposition chamber. The $^{28}Si_2^-$ signal resents a peak at a depth of 22 nm that mark the presence of Si NCs layer.

Figure 3.3.3 a) shows the normalized $^{31}P^-$ intensity depth profiles after thermal annealing for 4 h at 900, 1000, or 1100 °C, compared to the profile measured before annealing already reported in Figure 3.3.3 a). Thanks to thermal treatments, P diffuses in the SiO_2 and accumulates at the Si NCs region, both effects being more pronounced as the temperature is increased. In particular, after 900 °C 4 h all P is still within the SiO_2 matrix, after 1000 °C 4 h a small fraction of P (below 6% of the total integrated intensity) is trapped in Si NCs region, and finally after 1100 °C 4 h a significant fraction of P is trapped at the Si NCs region. No P accumulation in the SiO_2 layer between the Si NCs and the Si substrate is observed. As noted previously, the quantification of the above profiles is quite challenging as P is contained in two different matrices, SiO_2 and Si NCs, which are expected to have quite different relative sensitivity factors (RSF) [17].

In order to develop a quantification protocol, we measured the total P dose in our samples by RBS, that is not affected by matrix effects. A quite straightforward calibration of samples where P is contained only in one matrix is done just by normalizing to the measured dose, as described in section 3.1.1. This has been done, for example, to calibrate the profiles in Figure 3.3.3 b) relative to the sample as deposited and the one after annealing at 900 °C.

For mixed situations, i.e. where P is present both in SiO_2 and also trapped at Si NCs, we need to determine also the RSF in the layer containing NCs. In order to do this, we etched away the

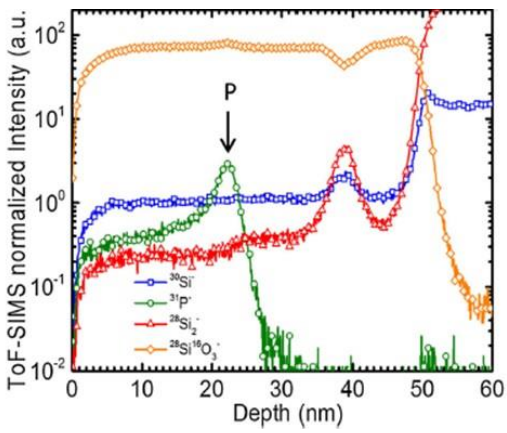

Figure 3.3.2 *- ToF-SIMS depth profile of the sample as deposited. The secondary ion yields have been normalized to the $^{30}Si^-$ yield. The location of the P peak, the silicon nanocrystals, the SiO_2 layers, and the Si substrate have been indicated.*

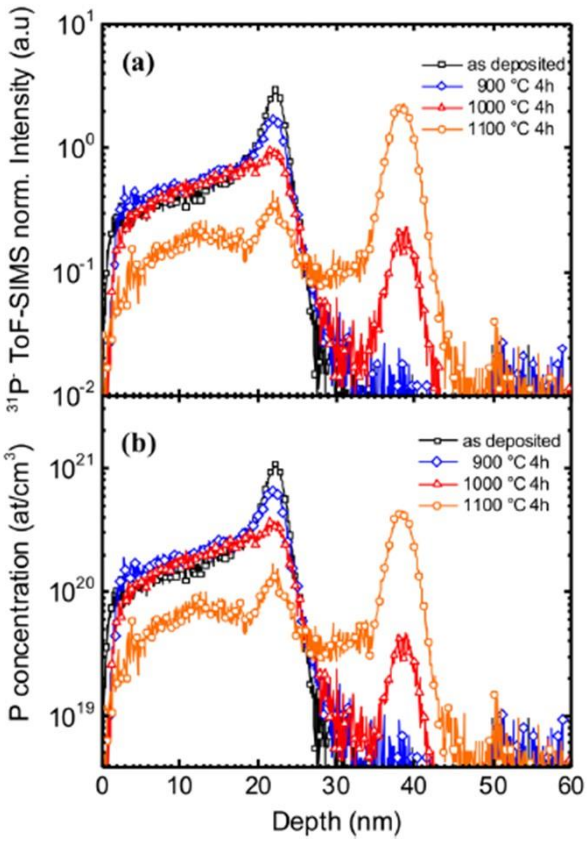

Figure 3.3.3 - ToF-SIMS depth profiles of the samples as deposited and after annealing for 4h at 900 °C, 1000 °C, and 1100 °C both expressed in P normalized intensity (a), and calibrated P concentration (b)

first 32 nm of SiO_2 in the sample annealed at 1100 °C by dipping in a HF solution, i.e. by removing all the P in SiO_2. The resulting sample had only P in NCs, as verified by ToF-SIMS (not shown). It is worth noticing that the P dose estimated by RBS has a higher relative uncertainty with respect to the other samples due to the lower amount of P.

Figure 3.3.4 reports all the P doses measured by RBS as a function of the corresponding depth integrals of the $^{31}P^-$ normalized SIMS intensity profiles of the samples discussed above. The data have been labeled according to annealing temperatures (and of the further etching, in the case of the sample annealed at 1100 °C), or with the label 'AD' for the sample as deposited. The graph also includes an additional data point (labeled as 'AD#2') relative to another sample fabricated with a similar deposition procedure as the 'AD' sample but with a slightly different P profile (not shown). The different symbols in Figure 3.3.4 identify the data with respect to the different matrices where P is located, i.e. filled squares for data relative to P entirely contained in SiO_2, open squares for the data relative to P present both in SiO_2 and in Si NCs, and open triangle for the datum relative to P present only in Si NCs.

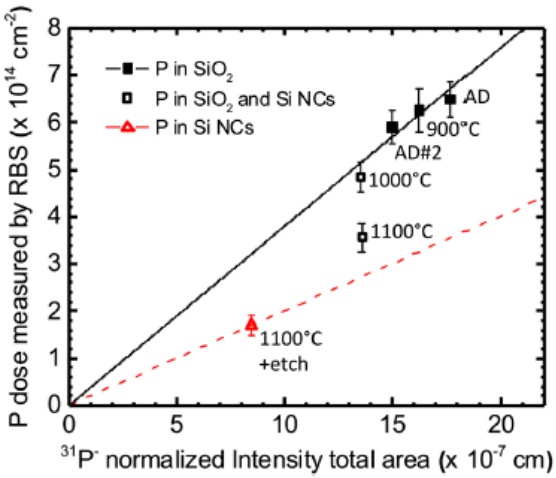

Figure 3.3.4 - P dose estimated by RBS as a function of the corresponding integrated area of the ToF-SIMS $^{31}P^-$ intensity extracted by different samples before and after isochronal annealing at different temperatures for 4 h and after further chemical etching to partially remove SiO_2, as indicated by the labels. Thermal annealings have been done on the as deposited sample referred as 'AD'. Different symbols identify the data with respect to the different matrices where P is located. The continuous line represents the linear fit passing through zero of the P data in SiO_2. The dashed line is to guide the eye and represents the hypothetical line that would be followed by P located in Si NCs at different doses.

It is clear from Figure 3.3.4 that data relative to P only in SiO_2 and P only in the Si NCs layer follow different trends, indicative of a significant matrix effect. The linear fit reported in the figure as a continuous line allows to estimate the RSFs value in SiO_2, whereas the RSF in the layer containing Si NCs is estimated by the single point with P only in the Si NCs ('1100 °C + etch'). The good fit obtained for the P doses in SiO_2 reported in Figure 3.3.4 suggests a linear dependence of the $^{31}P^-$ intensity as a function of the P concentration in SiO_2. The $^{31}P^-$ intensity relative to P trapped in a Si NC layer such is found to be about a factor of two higher than for P in SiO_2 with the same mean concentration, being the ratio of the two RSFs equal to RSF^P_{SiO2} / $RSF^P_{Si\_NCs}$ = 1.9 ± 0.3. It is worth noticing that the data relative to the sample after 1000 °C and the one after 1100 °C with no further etching fall consistently between the two calibration lines, due to the P contained both in SiO_2 and in Si NCs. From the dispersion of the SIMS data in SiO_2 relative to the fitting line, we can conclude that the relative uncertainty of the total area of a single ToF-SIMS measurement is lower than 8%.

The RSF^P_{SiO2} and $RSF^P_{Si\_NCs}$ determined above can be used to fully calibrate a $^{31}P^-$ intensity profile with P both in Si NCs and in the SiO_2 matrix. This has been done for the profiles after 1000 °C and 1100 °C, as reported in Figure 3.3.3 b) and in Figure 3.3.5, where $RSF^P_{Si\_NCs}$ has been used to calibrate P within the 35–44 nm depth interval, and the RSF^P_{SiO2} outside. It is

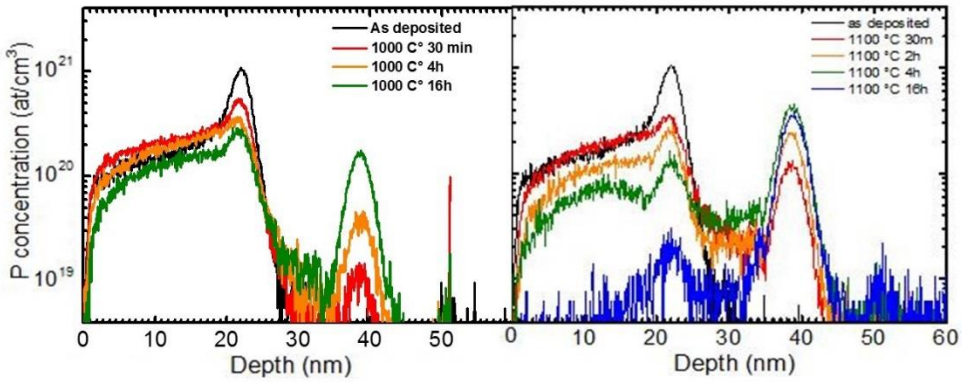

Figure 3.3.5 - ToF-SIMS calibrated P depth profiles of the samples as deposited and after annealing for 30 min, 4h and 16h at 1000 °C and for 30 min, 2h, 4h and 16h at 1100 °C

worth noticing that the total P doses estimated by the two above calibrated SIMS profiles are in agreement within errors with the P doses estimated by RBS.

A further comment is deserved on the origin of the P intensity enhancement at the Si NCs. Figure 3.3.6 shows the ToF-SIMS intensity profile measured with the same conditions as before on a sample obtained by implanting 20 keV P^- ions with a fluence of 5×10^{14} cm^{-2} in a SiO_2(30 nm)/Si layer. The ion energy has been chosen in order to have the projected range approximately at the same depth of the SiO_2/Si interface. It is clear that that the lower $RSF^P_{Si\_NCs}$ with respect to RSF^P_{SiO2} cannot be envisaged as a result of an intermediate average Si concentration in the Si NC layer between the two SiO_2 and pure Si extremes; as in Figure 3.3.5, the P intensity is lower in the Si substrate than in SiO_2. On the contrary, the figure reveals a marked P peak at the SiO_2/Si interface. A similar peak, even if somewhat to a lower extent,

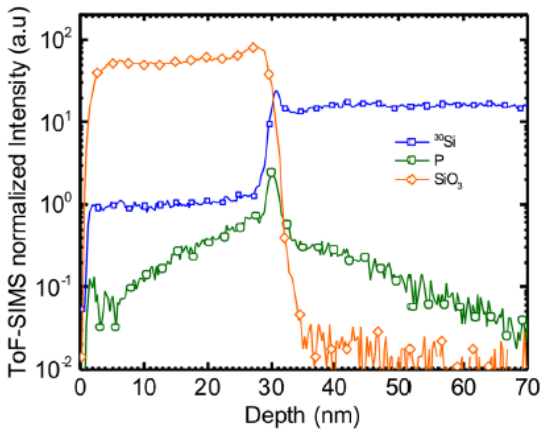

Figure 3.3.6 - ToF-SIMS depth profiles of a SiO_2/Si sample after ion implantation with 20 keV P 5×10^{14} cm^{-2}. The secondary ion intensities have been normalized to the ^{30}Si intensity.

is observed also for $^{30}Si^-$. This suggests that the P intensity enhancement at the Si NCs is related to an interface effect. As shown in ref. [217] the surface Cs concentration during SIMS analysis with a Cs primary beam lowers by passing from SiO_2 to Si. The intensity enhancement observed for $^{31}P^-$ at the NCs can thus be interpreted as a transient effect occurring at the SiO_2/Si interface of the Si NCs where, due to of a transient in establishing the steady-state Cs concentration of Si sputtering when passing from SiO_2 to Si, $^{31}P^-$ ions are formed at a surface rich in Si, but with a Cs concentration still close to the one typical of the steady state of SiO_2 sputtering.

Figure 3.3.7 reports the XPS high-resolution spectrum of the P 2*p* core level signal after subtraction of the Si 2*p* plasmon loss signal, for the sample annealed at 1100 °C for 4 hours. XPS measurements were performed on a PHI 5600 instrument equipped with a monochromatic Al Kα x-ray source (1486.6 eV) and a concentric hemispherical analyzer. The spectra were collected at a take-off angle of 75° with a bandpass energy filter at 11.75 eV. The spectrometer was calibrated using polycrystalline gold, silver, and copper samples. The thickness of the SiO_2 capping layer was reduced to 2 nm by calibrated HF etching before XPS analysis, in order to reducd the distance between the sample surface and the Si NC layer. This allowed detecting photoelectron directly emitted from the Si NCs optimizing the signal to noise ratio in the high resolution XPS spectra. The fitting of the experimental data was performed considering a simple Voigt functions to fit the P 2*p* spectral line above the loss structure of the intense Si 2*p* signal located at 100 eV. A very broad Gaussian profile was used to model the background. According to the literature, P atoms in the SiO_2 matrix correspond to a P 2*p* signal at 135 eV, while P atoms in a Si matrix exhibit a P 2*p* signal centered at 129 eV

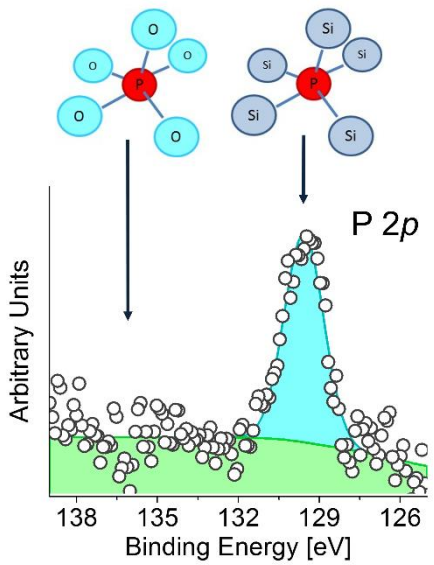

Figure 3.3.7 *- High-resolution XPS spectrum of the P 2p core level signal after subtraction of the Si 2p plasmon loss signal for the sample annealed at 1100 °C for 4 hours upon partial removal of the SiO_2 capping layer by means calibrated HF etching*

[137]. The data reported in Figure 3.3.7 demonstrate that most of P atoms diffusing during the annealing process are trapped in the Si NCs region and are efficiently incorporated in the core of the nanostructure or in a sub-interface region with no bonds with O atoms.

The sensitivity of the XPS measurements does not allow excluding the presence of a residual amount of P in the surrounding SiO_2 matrix. Nevertheless, on the basis of the calibrated ToF-SIMS profiles we can estimate that the concentration of P atoms in the SiO_2 film is of the order of 10^{19} atoms/cm^3, corresponding to a very limited fraction of the total amount of phosphorous trapped in the NCs region.

Assuming that all P is trapped inside Si NCs, the ToF-SIMS P profiles reported in Figure 3.3.5 could be used to provide a clear insight on the dynamics of the trapping process. It is evident from the calibrated diffusion profiles that increasing the annealing time, more P atoms diffuse through the SiO_2 matrix and reach the Si NCs region where they are effectively trapped. On the basis of the calibrated ToF-SIMS profiles, it is possible to measure the amount of P atoms that are trapped in the NCs: the P areal density in the NCs (Φ) can be computed by integrating the concentration profile peak at the NCs. At the same time the EFTEM cross sectional and plan view images provide a direct estimation of the average areal density of the Si NCs (N). The ratio Φ/N gives the average number of P atoms trapped within a single NC structure, while, dividing by the average number of Si atoms per NC we can get the atomic fraction (percentage) of P within Si NCs:

$$c_P^{NCs}(at\%) = \frac{\Phi}{N}\frac{100}{c_{Si}V} \qquad (3.3.1)$$

where c_{Si} is the crystalline Si atomic density and V the average volume of the clusters in the approximation of spherical shape. In Figure 3.3.8 we report the values of Φ/N (left axis) and

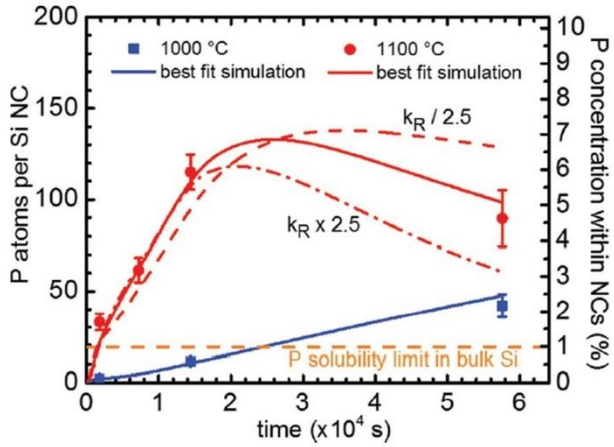

Figure 3.3.8 - Experimental P concentration inside the NCs as a function of time at the same temperature. Data points are deduced by considering the integral of P concentration profiles at NCs (from 35 to 45 nm) and the NCs size as determined by EFTEM. Continuous line comes from the numerical simulations based on rate equation model

of c_P^{NCs}(right axis) as a function of annealing time in the case of isothermal treatments at 1100 °C and at 1000° C. A progressive increase of the P concentration in the Si NCs is observed when rising the annealing time up to 4 hours. The trapping mechanism at 1100 °C allows achieving a very high P concentration within the Si NCs of about 6 %. This value largely exceeds the solid solubility for P in bulk Si [218] .For longer annealing (16 hours), the diffusion source strongly diminishes while the amount of P in NCs slightly reduces. This result demonstrates the strong stability of the P atoms incorporated into the Si NCs.

3.3.1.3 Modelling of P trapping/detrapping

To understand the nature of diffusivity and energetics governing the entire system, a quantitative analysis is fundamental and a correct modeling approach is necessary. Moreover, the complete characterization and calibration of diffusivity in SiO_2 with different thermal history is an essential step because of the determination of P diffusivity in SiO_2 depends on preparation mode and thermal history of oxide.

First of all the P profile of the as deposited sample has to be reconstructed as starting point for simulation. According to the nominal deposition the ideal dose measured by SIMS (and calibrated by RBS) is present in a narrow depth of 0.5 nm. Moreover, two tails were added to reproduce accidental P contamination of the capping and inner oxides. In Figure 3.3.9 the ideal starting profile (red line) is reported. In order to check the reconstruction, the ideal starting profile was convoluted with SIMS resolution that perfectly reproduces the experimental profile (blue line in Figure 3.3.9). The SIMS resolution has a Gaussian component with 1.8 nm FWHM and two symmetric exponential tails with 0.9 nm decay length.

In order to fit the ToF-SIMS profiles and obtain quantitative physical information about the system, a model based on diffusion Fick's law in one dimension was used. We considered also three fluxes that describe the interaction of P with NCs: a capturing flux for the capturing process at NCs, a release flux for the release of P in the SiO_2 matrix from the NCs, and a diffusion flux through the uncovered area, as the first Fick's law, taking into account that P

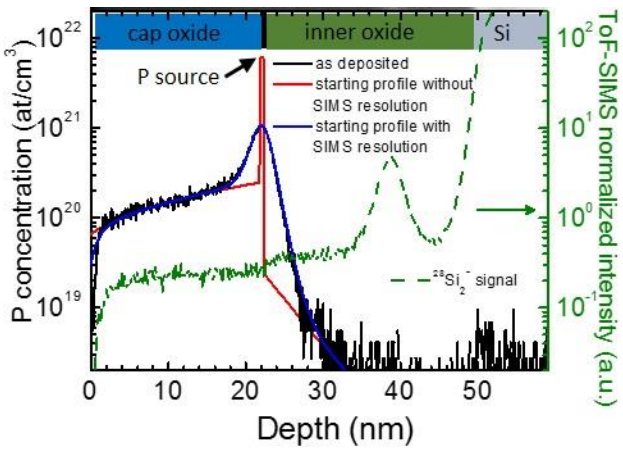

Figure 3.3.9 – P ToF-SIMS profile (black line) of the as deposited sample; ideal starting profile (red line) and convoluted one with SIMS resolution (blue line) are reported as the $^{28}Si_2^-$ signal (green dashed line)

can diffuse only through the fraction of the layer uncovered by NCs. Matching the fluxes by continuity equation allows writing the differential equations that describe the P concentration in the oxide (*C*) and the P doses into the clusters (Φ) as a function of time t and depth x. The presence of NCs causes the equation to be defined in 3 zones: 1) from the sample surface (*x = 0*) to the NCs layer, (*x = B*); 2) the NCs layer of depth d, from *B* to *B + d*; 3) the inner oxide after the NCs layer to the depth of SiO_2/Si substrate interface (*x = L*). the equation that we used are:

$$\frac{\partial C(x,t)}{\partial t} = \frac{\partial}{\partial x}\left(D(x,t)\frac{\partial C(x,t)}{\partial x}\right) \qquad \text{for } 0 < x < B \text{ and } (B+d) < x < L \qquad (3.3.2)$$

$$D(x,t)\frac{\partial C(x,t)}{\partial x} - \frac{D(x,t)}{\lambda}\cdot(C(x,t) - C_0) = 0 \qquad \text{for } x = 0 \text{ or } x = L \qquad (3.3.3)$$

$$\frac{\partial \phi(t)}{\partial t} = k_C \cdot N \cdot A \cdot D_D \cdot (C^+ + C^-) - k_R \cdot \phi(t) \qquad \text{for } B \le x \le (B+d) \qquad (3.3.4)$$

$$\frac{\partial C^-}{\partial t}\delta x = \left(D_D \cdot (1 - N \cdot A)\frac{(C^+ - C^-)}{d} - D_D\left(\frac{\partial C^-}{\partial x}\right)^-\right) - k_C \cdot N \cdot A \cdot D_D \cdot C^- + \frac{k_R}{2}\cdot\phi(t)$$

for $x = B$ (3.3.5)

$$\frac{\partial C^+}{\partial t}\delta x = \left(D_D\left(\frac{\partial C^+}{\partial x}\right)^+ - D_D \cdot (1 - N \cdot A)\frac{(C^+ - C^-)}{d}\right) - k_C \cdot N \cdot A \cdot D_D \cdot C^+ + \frac{k_R}{2}\cdot\phi(t)$$

for $x = (B + d)$ (3.3.6)

The P diffusion into oxides is described by second Fick's law in one dimension (Eq. 3.3.2). *D(x,t)* is the diffusivity and it depends on depth x in order to model diffusion in different zones: the capping SiO_2, the phosphorus rich thin layer and the densified oxide containing the NCs. From now on, the symbol D_D refers to the diffusivity in inner oxide densified during NCs formation. The diffusion coefficient is modulated in the different layers in order to reproduce the source P emission. Diffusivity is modelled as a function of space as polygonal chains and their vertices are characterized by depth position (nodes) and diffusivity values. The values of diffusivity can also evolve linearly with time. In the model the time evolution is reproduced by linear interpolation between fixed values of diffusivity at different experimental times. Practically a function of the code interpolates linearly between vertices in space and time creating a discretized profile for *D(x,t)* at each time step of simulation. The diffusivity in the densified oxide is the most important physical parameter that regulates the P exchange between NCs and their surrounding SiO_2 matrix. Both samples with NCs and reference samples without NCs were analyzed and modeled to help the model calibration. We considered Eq. 3.3.3 as boundary conditions at interfaces. It very generally describes, by means of λ parameter, the efficiency of the surface (*x = 0*) and the SiO_2/Si substrate interface (*x = L*) to sustain a fixed P interface concentrations C_0. Such concentrations are due to external environment (e.g. external atmosphere or contaminants at the surface, or P in the Si substrate at inner interface). Its limit cases correspond to a perfect sink where all dopant falls down in it ($\lambda \rightarrow 0$) or a perfect "mirror" interface ($\lambda \rightarrow \infty$) that reflects all dopant into the sample. The

boundary parameters are fitted on the reference samples without NCs and (λ = 3 nm; C_0 = $5 \cdot 10^{17}$ at/cm^3) and (λ = 10 nm; C_0 = 10^{10} at/cm^3) are respectively obtained at surface and SiO_2/Si substrate interface with small variations with temperature. Eq. 3.3.4 describes the variation with time of the P areal density in NCs, Φ. The balance of the capturing flux, $k_C \cdot D_D \cdot N \cdot A \cdot (C^+ + C^-)$, and release one, $k_R \cdot \Phi$, regulates it. C^- and C^+ are the P concentrations in the oxide just before ($x = B$) and after ($x = B+d$) the nanocrystals along the growth direction x. The capture is regulated by k_C, the capture parameter, D_D, the diffusivity in the densified oxide, and $N \cdot A$, the coverage fraction of the NCs in the layer equal to the product of N, the average areal density of the Si NCs, and A, the average cluster area. The release is proportional to the product of Φ and k_R, the release rate. k_C and k_R are constants that quantify respectively the capturing efficiency of the clusters and the rate at which a single P atom escapes from the clusters.

Eqs. 3.3.5 and 3.3.6 are the diffusion equations at the left and right sides of NCs layer. In particular in Eq. 3.3.5, the C^- concentration variation is the balance of the following fluxes:

- $D_D \cdot (1 - N \cdot A) \frac{(C^+ - C^-)}{d}$ is the flux that crosses the uncovered fraction $(1 - N \cdot A)$ between the clusters. The concentration gradient across the NCs layer is approximated by $\frac{(C^+ - C^-)}{d}$ where d is the NCs layer thickness;
- $-D_D \left(\frac{\partial C^-}{\partial x}\right)^-$ is the flux that comes from the left oxide and depends on the left derivative of C^-;
- $-k_C \cdot N \cdot A \cdot D_D \cdot C^-$ is the flux lost by trapping into NCs; the minus sign means that this flux subtracts P from the SiO_2 matrix and adds it to the NCs;
- $\frac{k_R}{2} \cdot \phi(t)$ is the flux gained by the release of P by clusters on the left size that we considered to be half of the full flux.

If the right derivative of C^+, $\left(\frac{\partial C^+}{\partial x}\right)^+$ is taken into account, Eq. 3.3.6 has a very similar description for C^+. The sum of these fluxes makes to change the areal density of P in the interval δx around C^+ (or C^-). δx is the discretization parameter used for numerical solution; the result does not change for small enough δx.

The full system of differential equations was discretized and solved using the finite difference method of Crank-Nicolson . The algebraic problem was solved with the tri-diagonal matrix algorithm . The semi-implicit algorithm was implemented in an code created *ad-hoc*. We used as depth step δx = 0.01 nm and as time step dt = 30 s in all simulations. The numerical accuracy and stability are guaranteed until $\delta x \leq 0.02$ nm and $dt < 36$ s.

All simulated profiles are calculated starting from the reconstructed (ideal) P profile described before and are convolved with ToF-SIMS resolution before comparison with experimental data. The code also manages the parameters optimization by means of chi-square minimization algorithm applying Simplex Method [219] comparing convolved profiles to experimental ones for the evaluation of chi square. The coverage fraction of the NCs is determined by the experimental EFTEM data [220] ($N \cdot A \approx 0.2$) as the boundary conditions by fitting the ToF-SIMS profiles of the reference samples. Therefore, the diffusivity D, the capture parameter k_C and the release rate k_R are the free fundamental atomistic parameters of the

model. A single set of these free parameters is optimized for all the different annealing times at a given temperature by minimizing a cumulative chi-square function.

In Figure 3.3.10 a) and 3.3.10 b) the best-fit profiles are reported by continuous black lines for samples annealed at 1000 °C and 1100 °C, respectively. A good agreement with experimental ToF-SIMS data (colored lines) is achieved at each temperature. The corresponding diffusivity profiles at time zero and at each annealing time are reported in Figure 3.3.10 c) and 3.3.10 d).

The variation with depth of the diffusivity was obtained under the following assumption: the diffusivity is constant within each oxide matrix (capping layer and densified inner oxide) and its values in the P–SiO_2 source layer could be different due to the high concentration of P. Up to 4 nodes are used in the source region to correctly reproduce the P emission from the source. Moreover, the P–SiO_2 peak does not vanish also after a very long annealing time and therefore a fraction of the peak was assumed to be immobile (clustered) during the process. We considered as free parameters the diffusivity values in these vertices at time zero (as deposited profiles) and at each annealing time.

The diffusivity values in the P-SiO_2 thin layer, together with clustering parameters, describe satisfactorily in a phenomenological way the source features, regulating its emission capability by establishing gradients that favor diffusion in oxides. Their values are orders of magnitude lower than those in capping and densified oxides. Practically, these values are effective

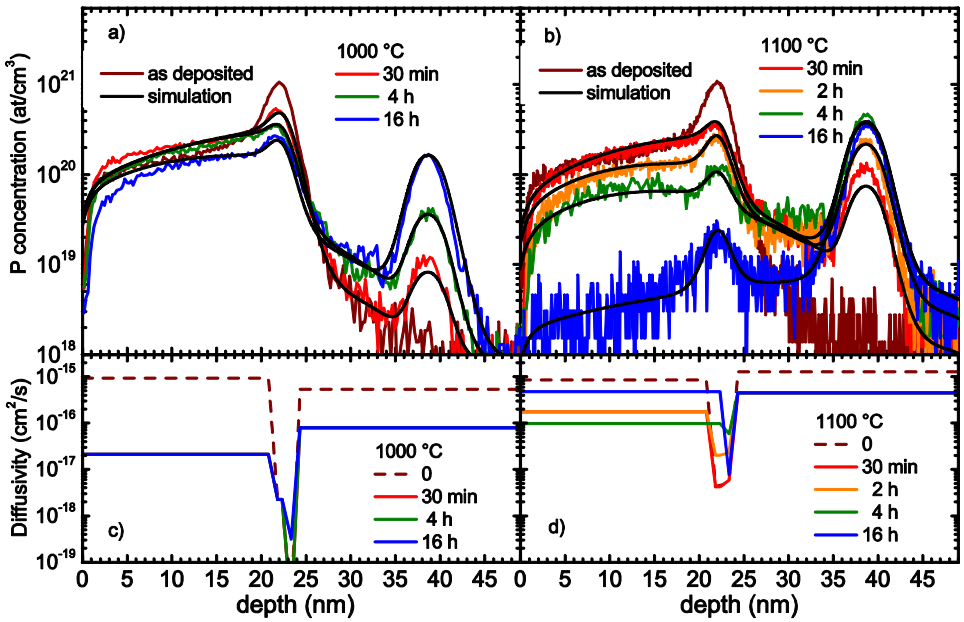

Figure 3.3.10 - (a) and (b) P concentration profiles for different annealing times at 1000 °C and 1100 °C (colored lines), respectively, and corresponding simulation fittings (black lines). (c) and (d) diffusivity vs. depth diagrams for different annealing times at 1000 °C and 1100 °C, respectively.

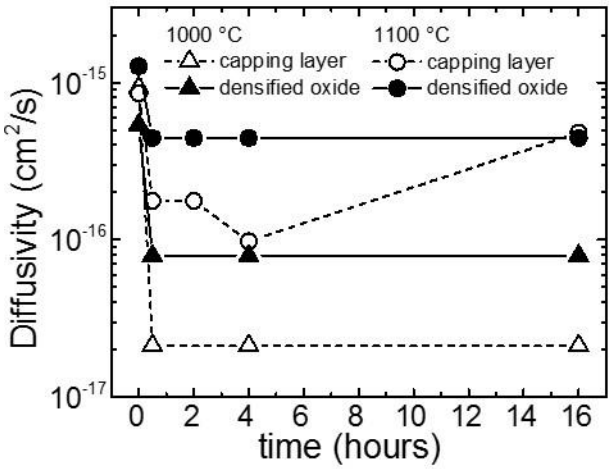

Figure 3.3.11 - Diffusivity values in capping layer (open symbols) and densified oxide (closed symbols) for different annealing times at 1000 °C (triangle symbols) and 1100 °C (circle symbols)

parameters able to reproduce the P fluxes coming from the source. A different choice of the nodes around the source depth produces different effective parameters and similar simulations but, very importantly, it does not change significantly the value of diffusivity in the bulk parts of the oxides. The analysis of diffusivity values in oxides is therefore more interesting and physically meaningful.

In Figure 3.3.11 we reported diffusivities values in capping layer (from sample surface to P-SiO_2 layer) and in densified oxide (from P-SiO_2 layer to the SiO_2/Si substrate interface) as a function of time. A strong decreasing transient diffusivity is evident at the early stage of the annealing. Initial value at time zero is up to 6 times higher than value in densified oxide and it disappears until the first stage of annealing. These higher and transient diffusivity values are requested in order to reproduce the fast dissolution of P peak without a substantial broadening of P profile in densified oxide. The initial diffusivities seem not to strongly depend on temperature or nature of oxide: all values are comparable within a factor of two.

In densified oxide, the diffusivity keeps constant with time at both temperatures after initial transient. The diffusivity is also approximately constant in the capping layer at 1000 °C and its value is lower than the one in the densified oxide, while at 1100 °C it goes back to the densified value for the longer annealing time. The values of P diffusivity in oxide reported in literature strongly depend on annealing conditions, nature of P source and SiO_2 matrix, kind of oxide, methods for determining the diffusivity. The annealing ambient was N_2 gas and the diffusivity was determined with the same methodology in all samples. Therefore, the differences in diffusivity showed in Figure 3.3.11 should depend on P source and/or oxide properties.

Two interesting phenomena concerning diffusivity are revealed by our data: i) the diffusivity has a transient decrease for very short time that does not strongly differs from pre-densified and not-densified oxide ii) the diffusivity in not-densified oxide is lower than one of pre-

densified oxide after the transient: the difference keeps constant in time and disappear only for the higher post annealing thermal budget (1100 °C 16 h).

The first phenomenon suggests that the source injects two P species with different diffusion mechanisms according to their chemical status, independently on the matrix structure and defects. This fact was already suggested in Ref. [221], where a phosphosilicate glass over a thick thermal SiO_2 and annealing in N_2 or O_2 ambient were used. It was shown that P is initially present in the oxide in the form of a free acid of P and then P is incorporated into oxide in the bound form only at higher temperatures and with the assistance of O. This bound P is much less mobile than the initially unbounded species, both present during annealing in N_2, the difference being due to the binding with O[221]. Our data strongly support this interpretation and also demonstrate that the fast P injection by phosphosilicate occurs in evaporated SiO_2 both densified and not. Very likely, the population of faster species in our samples decreases with time causing the transient.

Moreover, the transient seems not to strongly depend on temperature, confirming the very high mobility (low barrier) of the first diffusing species. The convergence at the same diffusivity value at 1100 °C demonstrates that the structural evolution of the matrix toward a stable oxide is obtained both by thermal growth of SiO_2 or by the densification process at high temperature. Furthermore, this diffusivity value is taken into account in the description of the NCs interaction, guaranteeing the generality of its description. From another point of view, the above results indicate that the embedding SiO_2 needs to be well densified with a suitable annealing for an optimal control of the doping of Si nanostructures through diffusion.

In Figure 3.3.12 we report the diffusivity values in the inner densified oxide after the transient at different temperatures for the samples with NCs (closed squares) and for SiO_2 reference without NCs (open squares). An Arrhenius' formula correctly describes the diffusivity considering a as the length of each diffusion step ($a \approx 0.35\ nm$ the average distance between SiO_2 molecules), k_0 as an entropic prefactor and E_D as the enthalpy of diffusion:

$$D(T) = \frac{a^2}{6} \cdot k_0 \cdot exp\left(-\frac{E_D}{k_B \cdot T}\right) \qquad (3.3.7)$$

where k_B is Boltzmann's constant, T is temperature. By fitting of the experimental data we obtain E_D = (3.5 ± 0.5) eV and $k_0 = 1.9 \times 10^{13\pm2}\ s^{-1}$. Keeping k_0 value to the Debye frequency of SiO_2 (~10^{13} Hz) [222], we obtained (3.5 ± 0.1), reducing the error of energy barrier. Interestingly the diffusivity values obtained by Ref. [221] in N_2 ambient for thermal SiO_2 are perfectly compatible with our data for the densified oxide after the first transient exhaustion (closed star in Figure 3.3.12). We define the diffusivity rate k_D, *i.e.* the jumping frequency of P atoms, as:

$$k_D = k_0 \cdot exp\left(-\frac{E_D}{k_B \cdot T}\right) \qquad (3.3.8)$$

The structural status of P in the SiO_2 matrix is still a missing information but some knowledge can be deduced by comparing the obtained diffusivity with Si self-diffusion [223] and Si self-interstitial diffusion in SiO_2 [224]. These data are reported in Figure 3.3.12 with closed circles and open triangles respectively. As can be noted, the Si self-diffusion is much lower than P diffusion suggesting that substitution of Si by P in the structure is very unlikely. A very good agreement instead is present between P diffusion data and Si self-interstitial diffusion. This suggests that P moves like an excess atom in the matrix. The previous reasoning about the

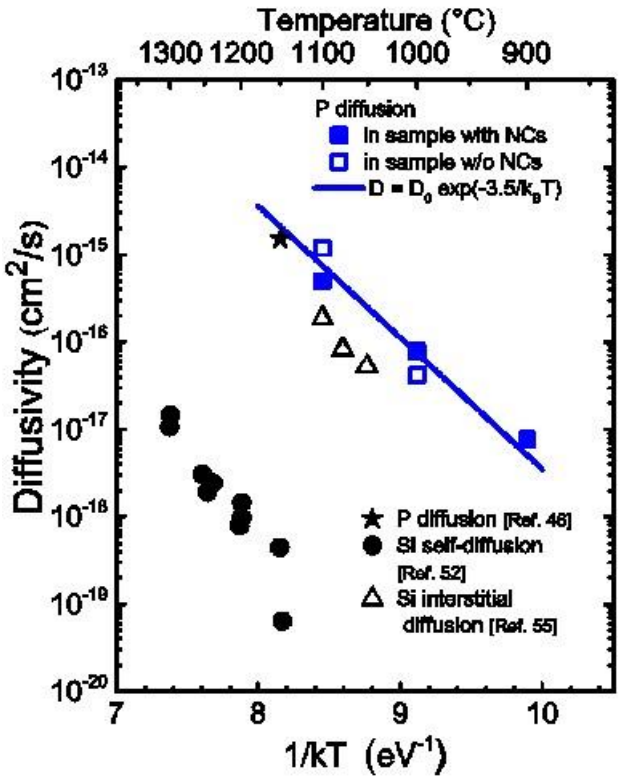

Figure 3.3.12 - : diffusivity values of the samples with NCs (closed blue squares) and reference SiO_2 samples (open blue squares). Literature values of similar system (black star) from Ref. [221]*, Si self-diffusion (closed black circles) from Ref.* [223] *and Si interstitial diffusion (open triangles) from Ref. 55 are also shown for comparison. The Arrhenius fit of experimental diffusivity is reported (solid line).*

bonding with oxygen suggests that the slow diffusing P species could be a P interstitialcy. The reduced diffusivity in the cap SiO_2 is coherent with the interstitialcy hypothesis: the cap undergoes a lower thermal budget and therefore it has a less densified structure with respect to the NCs containing SiO_2. Densification process corresponds to the elimination of interatomic voids so it can be seen as a process of elimination of vacancy like defects. It is reasonable that P interstitialcy can be trapped by vacancy-like defects explaining the reduced diffusivity in SiO_2 with lower thermal budget that we measured.

The description of the diffusivity in all the matrixes surrounding NCs allows obtaining an accurate model of the P flux interaction with the NCs. Since NCs are thermal stable, as confirmed by TEM analysis, and P diffusivity is constant in each bulk oxide, the system is very close to equilibrium conditions. Therefore, the parameters controlling P – NCs interaction (the capture parameter and release rate) can be accurately determined. Figure 3.3.13 reports k_D values at different temperatures for the samples with NCs and for the SiO_2 reference. The same plot reports k_R values as deduced by the $^{31}P^-$ profile fitting. As can be noted, a P atom

leaves the cluster with a much smaller frequency than the one regulating its diffusion jump. Diffusivity (release) rates are well fitted by Arrhenius' formula:

$$k_{D(R)} = k_0 \exp\left(-E_{D(R)}/kT\right) \qquad (3.3.9)$$

using a single $k_0 = 3.2 \cdot 10^{13}$ s^{-1} that is the attempt frequency with no barrier (in the high temperature limit), a diffusion barrier $E_D = 3.5$ eV, and a higher release barrier $E_R = 4.5$ eV.
The inset of Figure 3.3.13 summarizes the energy scheme for P-NCs interaction. P is thermodynamically favored to be trapped at NCs with a binding energy of:

$$E_B = E_R - E_D = (1.0 \pm 0.1)\, eV \qquad (3.3.10)$$

The capturing constant is independent by the annealing temperature and equal to $k_C \approx 25\ nm^{-1}$. The high value of k_C confirms the experimental data: the NCs trapping is extremely efficient preventing P to diffuse across the NCs layer. This happens because the trapping process prevails the diffusion through the uncovered fraction of the NCs layer. The independence of k_C on temperature indicates that no additional capture barrier should be added to the diffusion barrier and thus P trapping by Si NCs is limited only by diffusion.

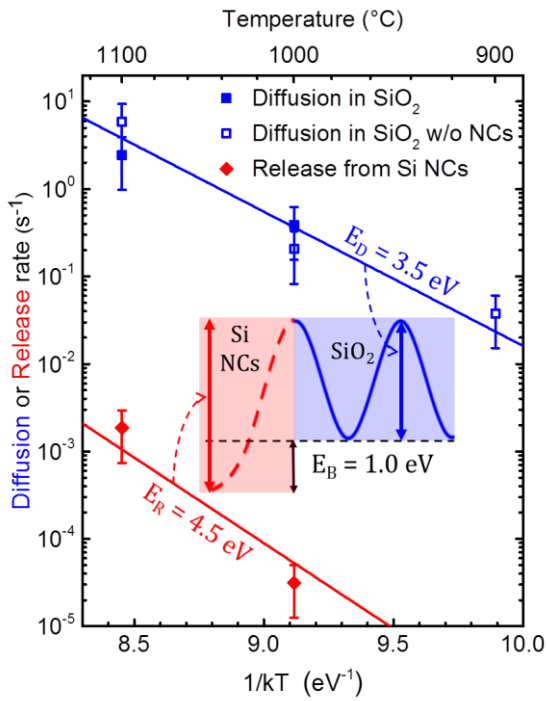

Figure 3.3.13 - Diffusion (release) rates are reported with filled blue squares (red). Data relative to reference SiO_2 samples are reported (blue). The Arrhenius fit of experimental diffusion (release) rates is reported (solid line). The inset depicts the entire energy scheme.

3.3.1.4 Discussion

The results of our experimental and modeling analysis depict an interesting scenario of the system very close to equilibrium, since Si NCs do not evolve during P diffusion and the P trapping process occurs without perturbing the original nanostructures. Consequently, this experimental layout supports a straightforward correlation with the effective configuration of theoretical calculations considering the role of the embedding matrix. Carvalho *et al.*[33] determined a binding energy of about 3 eV using silanol groups to simulate the oxide at the surface of the Si NCs. Similarly, Guerra *et al.*[31] found a value of 4 eV considering a more extended SiO_2 shell. Both data largely exceed our experimental value. Using a more complex model, Ni *et al.*[32] recently pointed out the role of dangling bonds at the Si/SiO_2 interface, suggesting that they may facilitate the incorporation of P in Si NCs embedded in SiO_2 with a binding energy of 1 eV,[32] in perfect agreement with our finding.

Another remarkable result is the very high concentration of P in NCs of 6% obtained, which is significantly higher than the measured P solubility limit in bulk Si (0.4 ÷ 1.0 % at 1100 °C).[218] Nanoscale solubility (for 4 nm clusters) appears thus to be more than 6 times higher than the bulk one. The adopted condition allows asserting that this is a lower level estimate of P solubility in Si NCs: if the model parameters are used to calculate the equilibrium steady state between capture and release with a not exhaustive source, the concentration of P in NCs might in fact increase up to 20%. This result suggests that solubility of dopants may increase by reducing the semiconductor size, at least down to the investigated size of few nanometers, in contrast with theoretical models predicting self-purifications phenomena,[28]–[30], [225], [226] that were suggested or cited by experiments far from equilibrium.[14], [22], [23], [83] In particular, in the light of our findings, it is interesting to reinterpret results by Gnaser *et al.*,[14] showing a decrease, with cluster size, of the P amount incorporated in NCs during their formation. According to our model, the reported trend indicates that, very likely, small clusters (with a smaller capture area A) kinetically trap less P than bigger ones, but this does not demonstrate that at equilibrium smaller cluster can absorb a lower percentage of P.

3.3.2 Effect of Si NCs size on P incorporation

To understand the effect of Si NCs size on the P incorporation into Si NCs, we prepared samples with four different Si NCs size varying the thickness of the SiO layer. The thickness of the SiO layer was progressively increased from 2nm to 10nm by properly adjusting the evaporation parameters. Si NCs layers were synthesized by processing SiO_2(10 nm)/SiO/SiO_2 (10 nm) multilayer at high temperature in a conventional furnace (1150°C, 60 min). After NCs formation, P δ-layers were synthetized by MLD on the topo of SiO_2 film. MLD is performed using diethyl 1-propylphosphonate (DPP, Alfa Aesar, purity 97%) as P-containing molecules and mesitylene (Alfa Aesar, purity 98+%) as a solvent. The samples were immersed in a solution of mesitylene and DPP (25:1) and subsequently thermal processed. Processing time t_p was 3h, while processing temperature T_p was settled at 165 °C. finally, after the δ-layer formation, samples were capped with 10 nm thick SiO_2 film by e-beam deposition. To promote P diffusion and trapping in Si NCs without perturbing the equilibrium structure of the Si NCs, we performed thermal treatments at temperature lower than the one used for Si NCs synthesis, *i. e.* at 1100 °C.

3.3.2.1 Si NCs structure by EFTEM

Figure 3.3.14 reports the EFTEM plan view images of the samples just after the high temperature thermal treatment for synthesis of the Si NCs. Images show the presence of Si NCs with average size that progressively increase when increasing the thickness of the SiO layer. The average diameter measured from the plan view images are reported in Figure 3.3.15 a) – d), together with NCs size distribution and average areal densities. Gaussian like size distributions were obtained with average diameters linearly increasing with the increase of SiO thicknessn, as plotted in Figure 3.3.15 e).

3.3.2.2 P depth distribution and quantification

For the sample with the largest Si NCs (~4,2 nm size) and for the sample with the smallest ones (~2,5 nm size), the P total dose were directly measured by RBS just after the thermal treatment for the synthesis of Si NCs. P total doses in these samples are equal within the experimental error and it have been found to be (6.37 ± 0.72) x 10^{14} atoms/cm^2 and (6.36 ± 0.72) x 10^{14} atoms/cm^2 respectively. P quantified ToF-SIMS profiles of samples just after the thermal treatment for the synthesis of Si NCs are reported in Figure 3.3.16 (these samples are named "as deposited"). ToF-SIMS analyses were performed in a dual-beam ION-TOF IV system in negative mode using Cs^+ ions (1 keV, 70 nA, 250 × 250 µm^2 rastering) for sputtering and Ga+ ions (25 keV, 1 pA, 50 × 50 µm^2 rastering) for analysis. RSF^P_{SiO2} was calculated using RBS data. The P profiles exibit a very sharp peak at a depth of about 12 nm from the surface of the samples The full width at half maximum (FWHM) of this peak is less than 2 nm. This value is comparable with ToF-SIMS depth resolution for this analysis. The P sources are located in a region that is well separated from the NCs region situated at 30 nm depth. The peaks have a

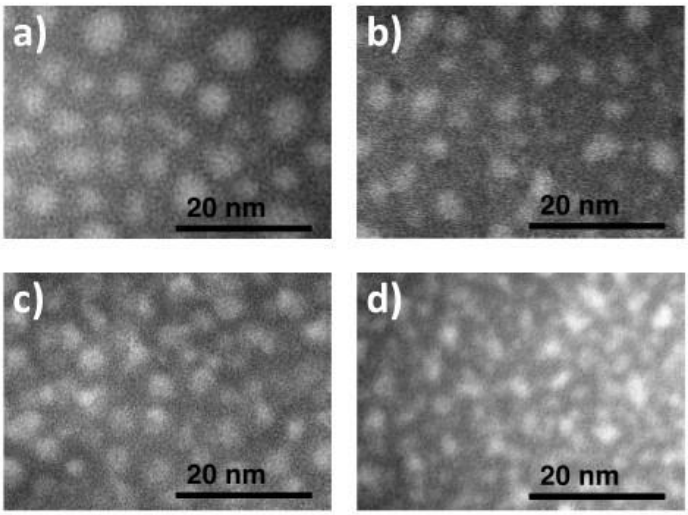

Figure 3.3.14 - EFTEM plan view of the SiO_2/SiO/SiO_2 multilayer structures after annealing (1150 °C, 60 min) in a tubular furnace to form the Si NCs. The images were obtained starting from multilayer structures with SiO thickness corresponding to 10 nm (a), 8 nm (b), 6 nm (c) and 4 nm (d) respectively.

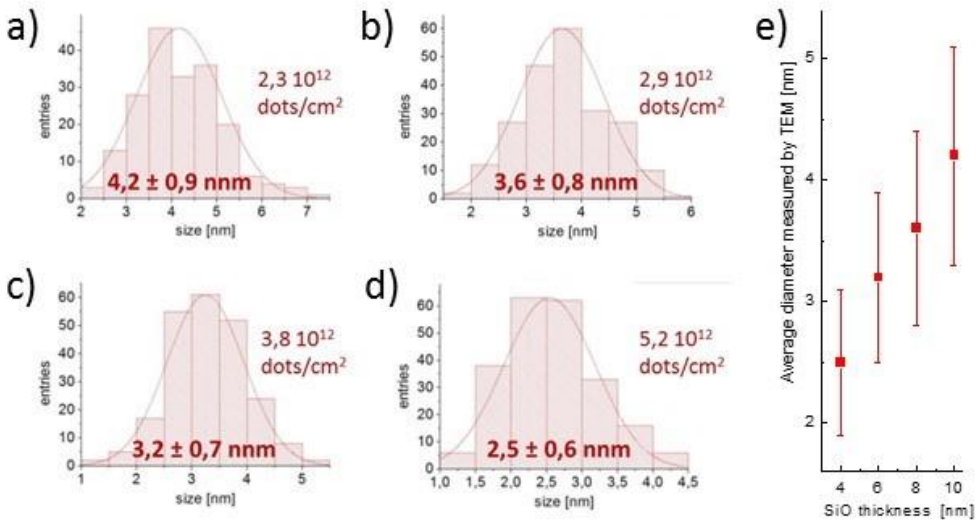

Figure 3.3.15 - Average diameters, NCs size distributions and average areal densities measured from the HRTEM plan view images. The images were obtained starting from multilayer structures with SiO thickness corresponding to 10 nm (a), 8 nm (b), 6 nm (c) and 4 nm (d) respectivel; e) Average diameter measured from the HRTEM plan view images as a function of SiO deposited thickness

trailing edge due to presence of physisorbed component from MLD process. P undesired contamination in Si NCs due to residual contamination from the evaporator chamber was detected to be lower than 10^{13} atoms/cm^2. P profiles were integrated in the P δ-layer region in order to extract P doses. P dose inside the δ-layer result to be the same for each samples as deposited samples within the ToF-SIMS experimental error. The average P dose in δ-layer is equal to 5.7 x 10^{14} atoms/cm^2 with a stand deviation of 0.2 x 10^{14} atoms/cm^2.

The quantification of ToF-SIMS profiles in the samples after P diffusion induced by high temperature thermal treatments is quite challenging. P is contained in two different matrices, namely SiO_2 and Si NCs, which are expected to have quite different relative sensitivity factors (RSF^P_{Sio2} and $RSF^P_{Si\_NCs}$). The RSF^P_{Sio2} has been determined from comparison with RBS data. In this work, we assume no dependence of $RSF^P_{Si\_NCs}$ from NCs size. Thus, knowing RSF^P_{SiO2} , the $RSF^P_{Si\_NCs}$ has been determined from the relation RSF^P_{SiO2} / $RSF^P_{Si\_NCs}$ = 1.9, in agreement with our previous findings for Si NCs with a diameter around 4 nm.

Figure 3.3.16 shows ToF-SIMS calibrated P depth profiles of the of samples before and after annealing for 4h, 9h and 16h at 1100 °C. Upon thermal treatment, P atoms diffuse in the SiO_2 and accumulate at the Si NCs region. P accumulation at Si NCs is quite always more pronounced as the annealing time increases. No P accumulation in the SiO_2 layer between the Si NCs and the Si substrate is observed.

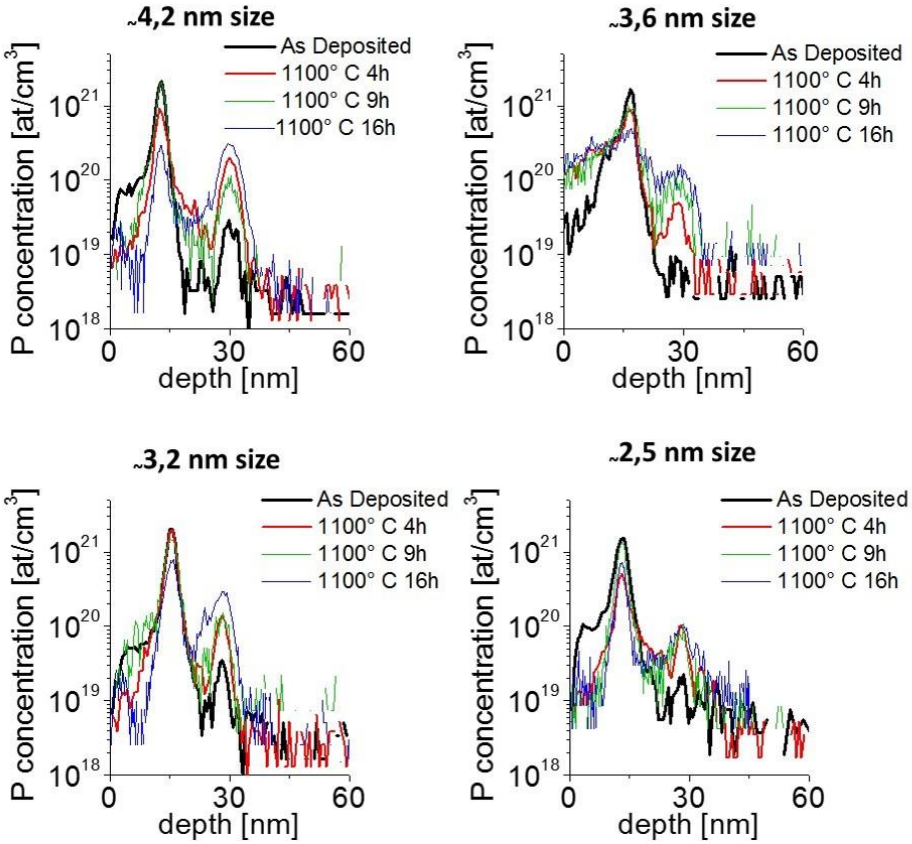

Figure 3.3.16 - ToF-SIMS calibrated P depth profiles of the samples just after the high temperature thermal treatment for synthesis of the Si NCs (as deposited) and after annealing for 4h, 9h and 16h at 1100 °C

In Figure 3.3.17 we report the XPS high-resolution spectrum of the P 2*p* core level signal for the samples with the largest Si NCs (~4,2 nm size) for samples just after the thermal treatment for the synthesis of Si NCs, annealed at 1100 °C for 9 h and annealed at 1100 °C for 16 h. XPS measurements were performed on a PHI 5600 instrument equipped with a monochromatic Al Kα x-ray source (1486.6 eV) and a concentric hemispherical analyzer. The spectra were collected at a take-off angle of 75° with a bandpass energy filter at 11.75 eV. The thickness of the SiO_2 capping layers were reduced to 2 nm by calibrated HF etching before XPS analysis, in order to reduce the distance between the samples surface and the Si NC layers. This allowed detecting photoelectron directly emitted from the Si NCs optimizing the signal to noise ratio in the high resolution XPS spectra. The fitting of the experimental data was performed considering a simple Voigt functions to fit the P 2*p* spectral line and a Gaussian curve for the loss structure of the intense Si 2*p* signal located at 100 eV. FWHM of the Gaussian curve for samples annealed at 1100 °C for 4h and for 9 h was fixed equal to the Gaussian curve's FWHM determined for the as deposited sample. According to the literature, P atoms in the SiO_2 matrix correspond to a P 2*p* signal at 135 eV, while P atoms in a Si matrix exhibit a P 2*p* signal centered at 129 eV [137]. The data reported in Figure 3.3.18 demonstrate that most of P

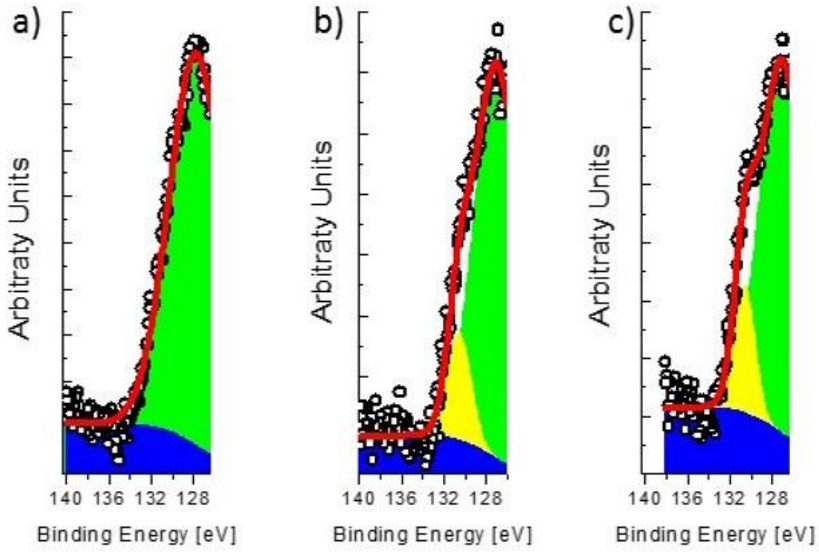

Figure 3.3.17 - XPS high-resolution spectrum of the P 2p core level signal for the samples with the largest Si NCs samples just after the thermal treatment for the synthesis of Si NCs (a), annealed at 1100 °C for 9 h (b) and annealed at 1100 °C for 16 h (c). The Si 2p plasmon loss signals have been fitted with a broad Gaussian (green), while P 2p signals have been fitted with a Voight function (yellow).

atoms diffusing during the annealing process are trapped in the Si NCs region and are efficiently incorporated in the core of the nanostructure or in a sub-interface region with no bonds with O atoms. The sensitivity of the XPS measurements does not allow excluding the presence of a residual amount of P in the surrounding SiO_2 matrix. Nevertheless, on the basis of the calibrated ToF-SIMS profiles we can estimate that the concentration of P atoms in the SiO_2 film is of the order of 10^{19} atoms/cm^3, corresponding to a very limited fraction of the total amount of phosphorous trapped in the NCs region.

Assuming that all P is trapped inside Si NCs also for samples with others size, the ToF-SIMS P profiles reported in Figure 3.3.16 could be used to provide a clear insight on the dynamics of the trapping process. Assuming that NCs are thermal stable and so that Si NCs size and densities doesn't change during thermal treatment, it is possible to measure the percentage amount of P atoms that are trapped in the NCs c_P^{NCs}. In Figure 3.3.18 we report the values of c_P^{NCs}as a function of annealing time. The filled data shown the behavior of P incorporation into Si NCs when P is delivered from P δ-layer source synthetize by MLD. The empty data refers to the previous experiment, where P was delivered from P-SiO_2 evaporated source. The experimental error for each point (not plotted) is estimated to be lower than 10% of the value itself, accordingly to ToF-SIMS experimental error for this system. These results confirm that the P source synthetized by MLD has different behavior from the P-SiO_2 source.

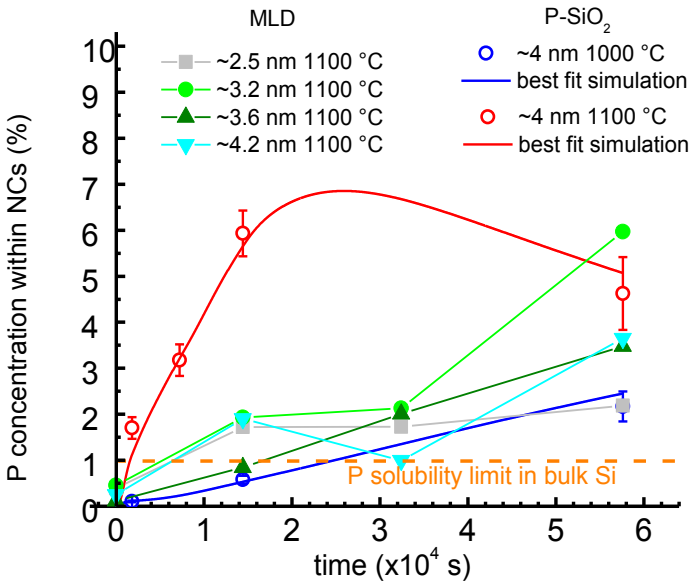

Figure 3.3.18 *- Percentage amount of P atoms trapped in the NCs as a function of annealing time. The filled data shown the behavior of P incorporation into Si NCs when P is delivered from P δ-layer source synthetize by MLD. The experimental error for each point (not plotted) is estimated to be lower than 10%. The empty data refers to the previous experiment, where P was delivered from P-SiO2 evaporated source*

3.3.2.3 Modelling of experimental data

To fit the ToF-SIMS profiles and obtain quantitative physical information about the system, we used the model based on diffusion Fick's law in one dimension that has been extensively presented in section 3.3.1.3. Figure 3.3.19 shows P concentration profiles and correspondent simulated profiles for samples with the largest Si NCs after δ-layer formation (a), annealing at 1100 °C for 4 h (b), 9 h (c), 16 h (d). Diffusivity, capture parameter and release rate were determined basing on modeling of all the experimental data reported in Figure 3.3.16.

Figure 3.3.20 reports k_D values for Si NCs with different size and compares these values with the data obtained for the samples with ~4nm size Si NCs. The same plot reports k_R values as deduced by the P profile fitting. As can be noted, a P atom leaves the cluster with a much smaller frequency than the one regulating its diffusion jump. Assuming that the increment of k_D and k_R as a function of temperature is equal to the increment previously obtained for the sample with ~4nm size Si NCs, E_R and E_D are calculated. In Figure 3.3.21 E_B is plotted as a function of Si NCs size. The value of E_B obtained for the sample with Si NCs having diameter ~4 nm is reported as well. The obtained E_B value prove that, for Si NCs size ranging from 2.5 nm to 4.2 nm, P incorporation inside Si NCs is thermodynamically favored. Absence of self-purification mechanism is suggested. The basic idea of self purification is that, as dopant atoms induce significant stress inside the crystalline core of Si NCs, the ejection of dopant impurities toward Si NCs surface results in a reduction of the total energy of the system. In

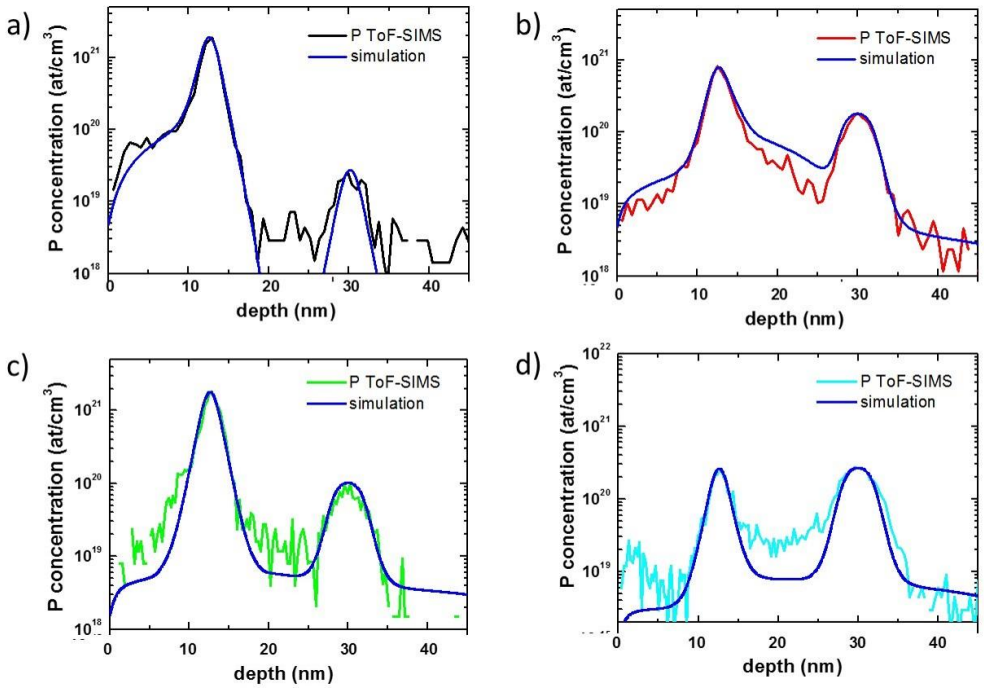

Figure 3.3.19 - P concentration profiles and correspondent simulated profiles for samples with the largest Si NCs after δ-layer formation (a), annealing at 1100 °C 4 h (b), 9 h (c), 16 h (d)

fact, stress induced by dopants at the surface can be accommodated by modification of surface geometry [30][102][103][28][104]. Chan *et al.* using a real-space first-principles pseudo-potential method investigated impurity incorporation in H-terminated Si NCs with diameter up to 6 nm. They found a critical Si NCs size (~2nm) below which the dopant atom is expected to be ejected toward the surface [104]. As our smallest Si NCs have average size of 2.5 nm, the comparison between theoretical prediction and our experimental results is not straightforward. Moreover, these theoretical predictions concern Si NCs H-terminated, while in our system Si NCs are embedded in SiO_2 matrix, depicting a completely different structural stress-induced scheme. Nevertheless, E_B clearly decrease decreasing Si NCs size, showing a linear dependency. This trend suggests that, even if incorporation of P atoms is energetically favored, P impurities are more easily extracted from smaller Si NCs.

3.3.2.4 Si NCs band structure

In the case of very small Si NCs, quantum confinement phenomena play an important role in the definition of their electrical and optical properties. Since Bohr radius of an exciton in silicon is about 5 nm, quantum confinement phenomena have been observed for Si NCs with

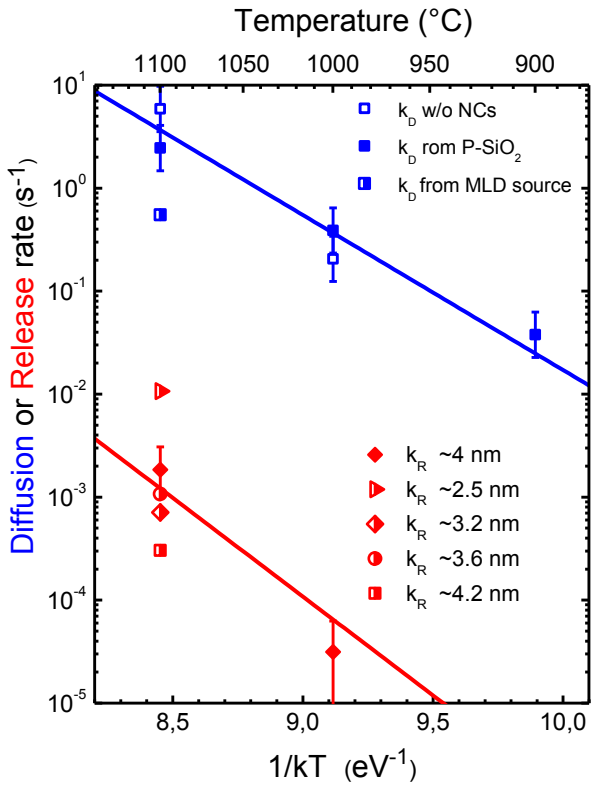

Figure 3.3.20 *- k_D and k_R values for the samples with different size Si NCs included the data previously shown for the sample with 4nm size Si NCs*

diameter smaller than 10 nm as widely reported in the literature [17][71][72][73][74]. The most striking effect is related to the progressive increase of the band gap [11][39][18][49][60]. In this work, the effect of quantum confinement were addressed by XPS.

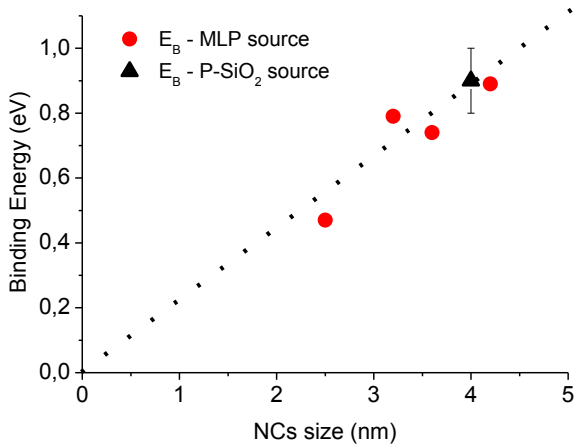

Figure 3.3.201 *– P binding energy inside Si NCs (E_B) in function of Si NCs size*

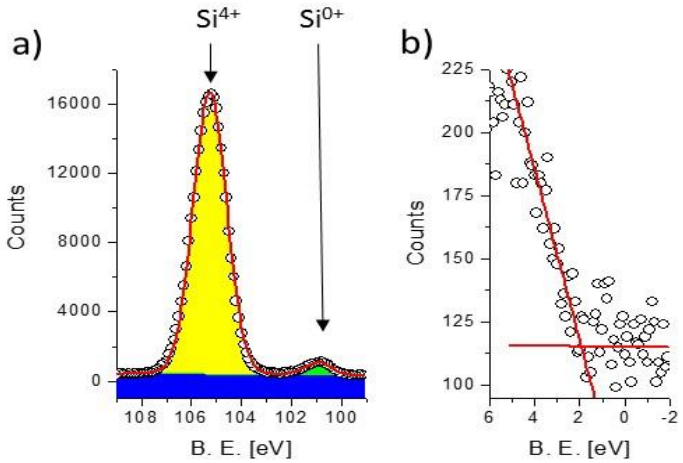

Figure 3.3.21 - High resolution XPS spectra of Si 2p (a) and Valence Band (b) region from the sample with the largest Si NCs (~4.2nm)

XPS analysis provided a characterization of the band structure of Si NCs. In particular,we monitored the energy distance between core level Si^{0+} 2*p* and the valence band maximum (VBM) as a function of Si NCs size. Evolution of the Si^{0+} 2*p* – VBM energy distance is used to detect variation in the band structures of the Si NCs when decreasing their size. Moreover, for the sample with the largest Si NCs, we investigated Si^{0+} 2*p* – VBM energy distance as a function of the atomic fraction of P incorporated in Si NCs (c_P^{NCs}).

Si NCs size ranging from 2.5 to 4.2 nm were studied as well as a reference crystalline bulk silicon covered with native oxide. XPS measurements were performed on a PHI 5600 instrument equipped with a monochromatic Al Kα x-ray source (1486.6 eV) and a concentric hemispherical analyzer. The spectra were collected at a take-off angle of 75° with a bandpass energy filter at 11.75 eV. The thickness of the SiO_2 capping layers was reduced to 2 nm by calibrated HF etching before XPS analysis, in order to reduce the distance between the samples surface and the Si NC layers. This allowed detecting photoelectron directly emitted from the Si NCs optimizing the signal to noise ratio in the high resolution XPS spectra.

In Figure 3.3.22 the high resolution spectrum of Si 2p (a) and Valence Band (b) regions from the sample with the largest Si NCs (~4.2nm) are reported. After Shirley background subtraction, Si 2*p* spectrum was fitted by a single Voigt function for the Si^{4+} signal and a doublet of Voigt functions for the Si^{0+} signal with intensity ratio of 0.5 and splitting of about 0.6 eV as fixed parameters. The Si^{4+} signal is related to the oxidation state of Si in SiO_2 while Si^{0+} signal is related to the oxidation state of Si inside Si matrix. The resulting position and FWHM for both the signals are in good agreement with data available in the literature [227][228]. Si^{0+} peak from Si NCs results to be larger than the one measured from crystalline Si bulk. This effect is related to the broadening of the spectral induced by the worse crystallinity of nanoparticles with respect to crystalline bulk Si [161]. Si^{4+} signal for the samples with Si NCs is shifted with respect to Si bulk value because of differential charging during XPS analysis, the distance between Si^{4+} Sand Si^{0+} is of about 4.5 eV, according to previous work

[227]. The error in peak positioning is estimated to be around 0.05 eV. The valence band maximum (VBM) was determined by the standard procedure based on a simple linear extrapolation [229], as shown in Figure 3.3.22 b).

In Figure 3.3.23 black squares refers to the energy distance between core levels (Si^{0+} 2*p*) and the VBM in function of Si NCs size. Errors bars refer to experimental error of EFTEM size measurements and to experimental error XPS data analyses. The red line indicate the Si^{0+} 2*p* - VBM distance for a bulk Si crystalline that was used as reference red line, the horizontal see-trough area corresponds to error for XPS data analysis. A decrease of Si^{0+} 2*p* - VBM energy distance as a function of Si NCs size is measured, pointing out the expected presence of electronic confinement effects [17][71][72][73][74]. In a recent work Seguini *et al.* [1] investigated the band alignment of Si NCs embedded in a SiO_2 matrix as a function of the average diameter of the Si NCs. Independent measurements of the Si NCs valence band (VB) and conduction band (CB) edge energy positions with respect to the SiO_2 matrix were acquired by means of photo-ionization (PI) and capacitance spectroscopy (C-S), respectively. Three different regimes were identified by progressively shrinking Si NCs diameter; primarily quantum confinement affects the conduction band that is shifted towards high energy values, then surface effects pin the conduction states, and finally quantum confinement modifies the valence band with a shift towards low energy values [1]. Data reported from Seguini *et al*. regarding VB shift with respect to VB of Si bulk are plotted in Figure 3.3.23 (green point, right

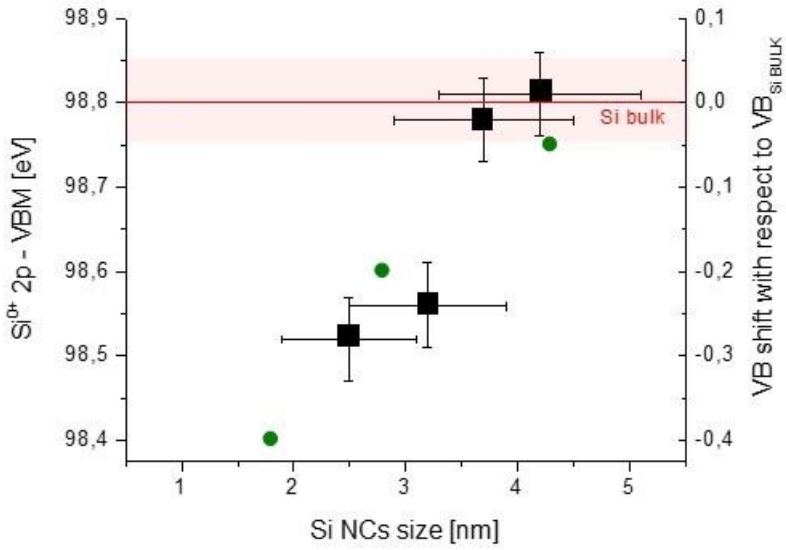

Figure 3.3.22 – Black squares (left axis): Si^{0+} 2p - VBM distance as a function of Si NCs size, errors bars refer to experimental error of EFTEM size measurements and to experimental error XPS data analysis. Red line(left axis): Si^{0+} 2p - VBM distance for Si crystalline bulk, the horizontal see-trough area corresponds to experimental error of XPS data analysis. Green points(right axis): VB shift with respect to Si bulk VB, data from Seguini et al. [1]

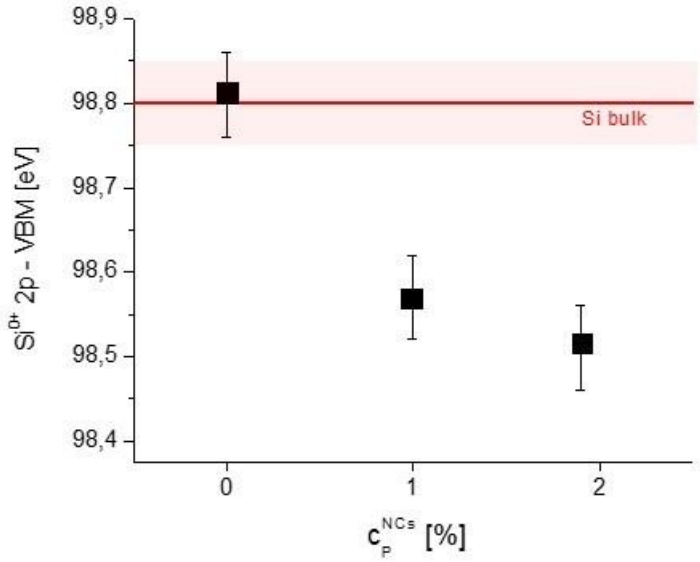

Figure 3.3.23 - Si^{0+} 2p - VBM distance as a function of c_P^{NCs} for Si NCs with average diameter ~4.2 nm

axis) and result to be in perfect agreement with our work. This result validated the use of XPS analysis for the study Si Ns band struture.

The same methodology was applied to investigate band structure evolution in P doped Si NCs with average diameter ~4.2 nm. In Figure 3.3.24, Si^{0+} 2*p* - VBM distance as a function of c_P^{NCs} is plotted. Si^{0+} 2*p* – VBM distance decrease increasing P doses incorporated in Si NCs. Suggesting a progressive shift of the valence band edge towards lower energy value when P impurities are incorporated within the Si NCs. Further experiments are currently running to elucidate this point.

Conclusions

This thesis focuses on the doping of Si NCs embedded in SiO_2 matrix. In particular, P impurities incorporation into Si NCs was promoted in Si NCs after their formation at thermodynamic equilibrium, by delivering a controlled amount of P atoms from a spatially separated diffusion source. The problem was faced using a multi-technique approach, involving TEM, ToF-SIMS, RBS and XPS. A quantification protocol for ToF-SIMS P depth profiles was developed, allowing the quantification of P dose trapped inside Si NCs. Quantitative physical informations about the system were obtained simulating ToF-SIMS depth profiles, by means of a model based on diffusion Fick's law in one dimension. This experimental approach shed a new light on the rich physics of nanostructures, providing the tools to investigate equilibrium phenomena predicted by theoretical works, like self-purification. For Si NCs with 4 nm average size, we demonstrated that P is thermodynamically favored to be trapped at NCs with a binding energy of E_B = 1.0 ± 0.1 eV. As the P trapping occurs at thermodynamic equilibrium, our experimental layout supports a straightforward correlation with theoretical calculations. Ni *et al.*[32] recently pointed out the role of dangling bonds at the Si/SiO_2 interface, suggesting that they may facilitate the incorporation of P in Si NCs embedded in SiO_2 with a binding energy of 1 eV,[32] in perfect agreement with our finding. Another remarkable result is the very high concentration of P in Si NCs of 6% obtained, which is significantly higher than the measured P solubility limit in bulk Si (0.4 ÷ 1.0 % at 1100 °C) [218]. P solubility in 4 nm Si NCs appears thus to be more than 6 times higher than the bulk one. The adopted condition allows asserting that this is a lower level estimate of P solubility in Si NCs: using the model parameters are to calculate the equilibrium steady state between capture and release with a not exhaustive source, the concentration of P in NCs might in fact increase up to 20%. This result suggests that solubility of dopants may increase by reducing the semiconductor size, at least down to the investigated size of few nanometers, in contrast with theoretical models predicting self-purifications phenomena,[28]–[30], [225], [226] that were suggested by experiments far from equilibrium [14], [22], [23], [83]. Moreover, for Si NCs size ranging from 2.5 nm to 4.2 nm, it was found that P is thermodynamically favored to be trapped within the Si NCs. Absence of self-purification mechanism is suggested, unlike theoretical calculation prediction [30][102][103][28][104]. A progressive reduction of P binding energy was observed decreasing Si NCs size, showing a linear dependency.

To define the effective position of impurities in Si NCs embedded in solid matrix, the most promising candidate is APT [14][23] [134]. In this thesis work, structural characterization of Si NCs embedded in SiO_2 was provided by APT and validated by TEM. This advanced characterization open the route to a protocol for the definition of the effective shape and size of the Si NCs, as well as the correct identification of the interface between the Si NCs and the surrounding matrix.

Others significant results were achieved regarding the P diffusion source synthesis. P δ-layers embedded in a SiO_2 matrix were formed by MLD process. The self-limiting behavior of the grafting process on SiO_2 substrate and the possibility to use these P δ-layers as diffusion sources were demonstrated. Moreover, formation of P δ-layers using P-terminated homopolymers was proposed for the first time. The self-limiting behavior of the grafting process on SiO_2 substrate, the capability to finely tune the P dose incorporated in the δ-layers as well as the possibility to use these P δ-layers for the formation of sub-20nm shallow junction in Si were demonstrated.

On the basis of this thesis, several interesting research activities can be envisioned to get further insight on the problem of semiconductor doping at nanoscale. First of all, exhaustive study of the effect of Si NCs size on the P incorporation into Si NCs is highly desirable. In this regards, Si NCs with diameter lower than 2 nm should be taken into account, in order to experimentally verified the occurrence/absence of self-purification mechanism at this small scale. Once completed the energetic scheme of trapping/detrapping, electrically activation of P atoms incorporated into Si NCs need to be addressed. Moreover, the study could be extended to the incorporation and electrically activation of different impurities (B, As, Al…) in Si NCs. *Ex situ* doping procedure could in principle be used also for the doping of nanostructures other than Si NCs, like for example Si nanowires. Finally, future study will address the problem of the electrical activation of P impurities delivered from P δ-layers, to assess their suitability as dopant source and the possibility to create ultra-shallow junctions.

Acknowledgments

First, I should thank Dr. Michele Perego and Prof. Cristina Lenardi for giving me the opportunity to attain this PhD.

Special acknowledgments go to everyone who collaborates in this experimental activity, to Gabriele Seguini and Jacopo Frascaroli from the the Laboratory of the Institute of Microelectronics and Microsystems (CNR) in Agrate Brianza. SpecialtThanks to Mario Alia, for technical assistance during chemical process. Thanks to Prof. Enrico Napolitani, Prof. Davide the Salvador, Dr. Massimo Mastromatteo and Lucia Scapin from the Padova University for RBS measures and for the modelling analysis. Thanks to Prof. Giuseppe Nicotra and Dr. Mario Scuderi from the Laboratory of the Institute of Microelectronics and Microsystems (CNR) in Catania for HRTEM analysis. Thanks to Prof. Yasuo Shimizu and Dr. Han Bin from the Institute for Materials Research (Oarai Center) of the Tohoku University for APT analysis. Thanks to Prof. Sylvie Schamm-Chardon and Prof. Gérard Ben Assayag from CEMES-CNRS, Toulouse University for HRTEM analysis.

…Grazie a Michele per avermi mostrato il gusto e la passione per la scienza e… per avermi iniziata all'attività di ricerca con analisi ToF di campioni (isolanti!!!) spessi 60 nm… È proprio vero che fatto quello si può fare tutto! Grazie a Gabriele per aver cercato di insegnarmi la sistematicità: considerato il livello da cui partivo hai ottenuto ottimi risultati. Grazie a Tommi e a Fabio per la loro quotidiana compagnia, sappiate che vi tengo sotto controllo entrambi. Grazie a Mario per avermi sopportata pazientemente in clean room anche all'ottavo mese di gravidanza. Grazie a Jacopo per aver condiviso da vicino l'inizio della mia esperienza in MDM. Grazie a tutti i tesisti che sono passati di qui: Flotto, Davide, Andrea, Marcello… è stato bello lavorare insieme anche se per poco!

Grazie a MONICA (so che hai aperto la tesi solo per cercare questa pagina) per la pazienza con cui mi accompagna in ogni passo della mia vita più o meno da 6 anni. Grazie ai miei bimbi, che mi hanno fatta diventare grande. E infine…. Grazie a mio marito, Mario, che miracolosamente continua a scommettere tutto su di me e mi fa sentire oggetto di un amore infinito...

Bibliography

[1] G. Seguini, C. Castro, S. Schamm-Chardon, G. Benassayag, P. Pellegrino, and M. Perego, "Scaling size of the interplay between quantum confinement and surface related effects in nanostructured silicon," *Appl. Phys. Lett.*, vol. 103, no. 2, p. 023103, 2013.

[2] M. C. Beard, K. P. Knutsen, P. Yu, J. M. Luther, Q. Song, W. K. Metzger, R. J. Ellingson, and A. J. Nozik, "Multiple exciton generation in colloidal silicon nanocrystals," *Nano Lett.*, vol. 7, no. 8, pp. 2506–2512, 2007.

[3] J. Tang, H. T. Wang, D. H. Lee, M. Fardy, Z. Huo, T. P. Russell, and P. Yang, "Holey silicon as an efficient thermoelectric material," *Nano Lett.*, vol. 10, no. 10, pp. 4279–4283, 2010.

[4] F. Priolo, T. Gregorkiewicz, M. Galli, and T. F. Krauss, "Silicon nanostructures for photonics and photovoltaics," *Nat. Nanotechnol.*, vol. 9, no. 1, pp. 19–32, 2014.

[5] R. Gresback, N. J. Kramer, Y. Ding, T. Chen, U. R. Kortshagen, and T. Nozaki, "Controlled doping of silicon nanocrystals investigated by solution-processed field effect transistors," *ACS Nano*, vol. 8, no. 6, pp. 5650–5656, 2014.

[6] Sze, *Physics of Semiconductor Devices*, vol. 10, no. 1. 1995.

[7] K. E. Moselund, H. Ghoneim, H. Schmid, M. T. Björk, E. Lörtscher, S. Karg, G. Signorello, D. Webb, M. Tschudy, R. Beyeler, and H. Riel, "Solid-state diffusion as an efficient doping method for silicon nanowires and nanowire field effect transistors," *Nanotechnology*, vol. 21, no. 43, p. 435202, 2010.

[8] G. Petretto, A. Debernardi, and M. Fanciulli, "Donor wave functions delocalization in silicon nanowires: The peculiar [011] orientation," *Nano Lett.*, vol. 13, no. 10, pp. 4963–4968, 2013.

[9] N. Fukata, J. Kaminaga, R. Takiguchi, R. Rurali, M. Dutta, and K. Murakami, "Interaction of boron and phosphorus impurities in silicon nanowires during low-temperature ozone oxidation," *J. Phys. Chem. C*, vol. 117, pp. 20300–20307, 2013.

[10] R. Guerra and S. Ossicini, "Preferential positioning of dopants and co-dopants in embedded and freestanding Si nanocrystals," *J. Am. Chem. Soc.*, vol. 136, pp. 4404–4409, 2014.

[11] L. Mangolini, "Synthesis, properties, and applications of silicon nanocrystals," *J. Vac. Sci. Technol. B Microelectron. Nanom. Struct.*, vol. 31, no. 2, p. 020801, 2013.

[12] F. Ruffino, L. Romano, E. Carria, M. Miritello, M. G. Grimaldi, V. Privitera, and F.

Marabelli, "A combined ion implantation/nanosecond laser irradiation approach towards SI nanostructures doping," *J. Nanotechnol.*, vol. 2012, 2012.

[13] M. Fujii, S. Hayashi, and K. Yamamoto, "Photoluminescence from B-doped Si nanocrystals," *J. Appl. Phys.*, vol. 83, no. 1998, pp. 7953–7957, 1998.

[14] H. Gnaser, S. Gutsch, M. Wahl, R. Schiller, M. Kopnarski, D. Hiller, and M. Zacharias, "Phosphorus doping of Si nanocrystals embedded in silicon oxynitride determined by atom probe tomography," *J. Appl. Phys.*, vol. 115, no. 3, p. 034304, 2014.

[15] M. Perego, G. Seguini, E. Arduca, J. Frascaroli, D. De Salvador, M. Mastromatteo, A. Carnera, G. Nicotra, M. Scuderi, C. Spinella, G. Impellizzeri, C. Lenardi, and E. Napolitani, "Thermodynamic stability of high phosphorus concentration in silicon nanostructures.," *Nanoscale*, vol. 7, no. 34, pp. 14469–75, Aug. 2015.

[16] M. Perego, C. Bonafos, and M. Fanciulli, "Phosphorus doping of ultra-small silicon nanocrystals.," *Nanotechnology*, vol. 21, no. 2, p. 025602, 2010.

[17] M. Perego, G. Seguini, and M. Fanciulli, "ToF-SIMS study of phosphorus diffusion in low-dimensional silicon structures," *Surf. Interface Anal.*, vol. 45, no. 1, pp. 386–389, 2013.

[18] M. Fujii, A. Mimura, S. Hayashi, K. Yamamoto, C. Urakawa, and H. Ohta, "Improvement in photoluminescence efficiency of SiO[sub 2] films containing Si nanocrystals by P doping: An electron spin resonance study," *J. Appl. Phys.*, vol. 87, no. 4, p. 1855, 2000.

[19] M. Fujii, A. Mimura, S. Hayashi, Y. Yamamoto, and K. Murakami, "Hyperfine Structure of the Electron Spin Resonance of Phosphorus-Doped Si Nanocrystals P concentration P-doped nc-Si," *Phys. Rev. Lett.*, vol. 89, no. 20, p. 206805, 2002.

[20] M. Fujii, K. Toshikiyo, Y. Takase, Y. Yamaguchi, and S. Hayashi, "Below bulk-band-gap photoluminescence at room temperature from heavily P- and B-doped Si nanocrystals," *J. Appl. Phys.*, vol. 94, no. 3, p. 1990, 2003.

[21] M. Fujii, Y. Yamaguchi, Y. Takase, K. Ninomiya, and S. Hayashi, "Control of photoluminescence properties of Si nanocrystals by simultaneously doping n- and P-type impurities," *Appl. Phys. Lett.*, vol. 85, no. 7, pp. 1158–1160, 2004.

[22] D. J. Rowe, J. S. Jeong, K. A. Mkhoyan, and U. R. Kortshagen, "Phosphorus-Doped Silicon Nanocrystals Exhibiting Mid-Infrared Localized Surface Plasmon Resonance - Supplementary Information," *Nano Lett.*, vol. 13, p. 1317, 2013.

[23] R. Khelifi, D. Mathiot, R. Gupta, D. Muller, M. Roussel, and S. Duguay, "Efficient n-type doping of Si nanocrystals embedded in SiO2 by ion beam synthesis," *Appl. Phys. Lett.*, vol. 102, no. 01, p. 013116, 2013.

[24] G. Kachurin, S. G. Cherkova, V. Volodin, V. G. Kesler, A. K. Gutakovsky, A. G. Cherkov, A. V. Bublikov, and D. I. Tetelbaum, "Implantation of P ions in SiO2 layers with embedded Si nanocrystals," *Nucl. Instruments Methods Phys. Res. Sect. B Beam Interact. with Mater. Atoms*, vol. 222, no. 3–4, pp. 497–504, Aug. 2004.

[25] A. I. Belov, V. A. Belyakov, V. A. Burdov, A. N. Mikhailov, and D. I. Tetelbaum,

"Phosphorus doping as an efficient way to modify the radiative interband recombination in silicon nanocrystals," *J. Surf. Investig. X-ray, Synchrotron Neutron Tech.*, vol. 3, no. 4, pp. 527–533, Aug. 2009.

[26] G. A. Kachurin, S. G. Cherkova, V. A. Volodin, D. M. Marin, D. I. Tetelbaum, and H. Becker, "Effect of boron ion implantation and subsequent anneals on the properties of Si nanocrystals," *Semiconductors*, vol. 40, no. 1, pp. 72–78, Jan. 2006.

[27] A. N. Mikhaylov, D. I. Tetelbaum, V. A. Burdov, O. N. Gorshkov, A. I. Belov, D. A. Kambarov, V. A. Belyakov, V. K. Vasiliev, A. I. Kovalev, and D. M. Gaponova, "Effect of Ion Doping with Donor and Acceptor Impurities on Intensity and Lifetime of Photoluminescence from SiO2 Films with Silicon Quantum Dots," *J. Nanosci. Nanotechnol.*, vol. 8, no. 2, pp. 780–788, 2008.

[28] T.-L. Chan, A. T. Zayak, G. M. Dalpian, and J. R. Chelikowsky, "Role of Confinement on Diffusion Barriers in Semiconductor Nanocrystals," *Phys. Rev. Lett.*, vol. 102, no. 2, p. 025901, 2009.

[29] G. Dalpian and J. Chelikowsky, "Dalpian and Chelikowsky Reply:," *Phys. Rev. Lett.*, vol. 100, no. 17, p. 179703, May 2008.

[30] G. M. Dalpian and J. R. Chelikowsky, "Self-purification in semiconductor nanocrystals," *Phys. Rev. Lett.*, vol. 96, no. 22, p. 226802, 2006.

[31] R. Guerra and S. Ossicini, "Preferential Positioning of Dopants and Co-Dopants in Embedded," *J. Am. Chem. Soc.*, vol. 136, pp. 4404–4409, 2014.

[32] Z. Ni, X. Pi, and D. Yang, "Doping Si nanocrystals embedded in SiO2 with P in the framework of density functional theory," *Phys. Rev. B*, vol. 89, no. 3, p. 035312, 2014.

[33] A. Carvalho, S. Oberg, M. Barroso, M. J. Rayson, and P. Briddon, "P-doping of Si nanoparticles: The effect of oxidation," *Phys. Status Solidi Appl. Mater. Sci.*, vol. 209, no. 10, pp. 1847–1850, 2012.

[34] A. Carvalho, M. J. Rayson, and P. R. Briddon, "Effect of Oxidation on the Doping of Silicon Nanocrystals with Group V Elements," *J. Phys. Chem. C*, vol. 116, p. 8243–8250, 2012.

[35] K. Dohnalová, T. Gregorkiewicz, and K. Kůsová, "Silicon quantum dots: surface matters," *J. Phys. Condens. matter*, vol. 26, no. 17, p. 173201, 2014.

[36] J. Heitmann, F. Müller, M. Zacharias, and U. Gösele, "Silicon nanocrystals: Size matters," *Adv. Mater.*, vol. 17, no. 7, pp. 795–803, 2005.

[37] X. Cheng, S. B. Lowe, P. J. Reece, and J. J. Gooding, "Colloidal silicon quantum dots: from preparation to the modification of self-assembled monolayers (SAMs) for bio-applications," *Chem. Soc. Rev.*, vol. 43, p. 2680, 2014.

[38] I. Dogan and M. C. M. van de Sanden, "Direct characterization of nanocrystal size distribution using Raman spectroscopy," *J. Appl. Phys.*, vol. 114, no. 13, p. 134310, 2013.

[39] T. Shimizu-Iwayama, N. Kurumado, D. E. Hole, and P. D. Townsend, "Optical properties of silicon nanoclusters fabricated by ion implantation," *J. Appl. Phys.*, vol. 83, no. 11, pp. 6018–6022, 1998.

[40] S. Guha, M. D. Pace, D. N. Dunn, and I. L. Singer, "Visible light emission from Si nanocrystals grown by ion implantation and subsequent annealing," *Appl. Phys. Lett.*, vol. 70, no. 10, pp. 1207–1209, 1997.

[41] G. Ghislotti, B. Nielsen, P. A. Kumar, K. G. Lynn, A. Gambhir, L. F. Di Mauro, and C. E. Bottani, "Effect of different preparation conditions on light emission from silicon implanted SiO2 layers," *Jpn. J. Appl. Phys.*, vol. 79, no. 11, p. 8660, 1996.

[42] W. S. Cheong, N. M. Hwang, and D. Y. Yoon, "Observation of nanometer silicon clusters in the hot-filament CVD process," *J. Cryst. Growth*, vol. 204, no. 1, pp. 52–61, 1999.

[43] L. He, T. Inokuma, Y. Kurata, and S. Hasegawa, "Vibrational properties of SiO and SiH in amorphous SiOx:H films ($0 \leq x \leq 2.0$) prepared by plasma-enhanced chemical vapor deposition," *J. Non. Cryst. Solids*, vol. 185, no. 3, pp. 249–261, 1995.

[44] A. J. Kenyon, P. F. Trwoga, C. W. Pitt, and G. Rehm, "Luminescence efficiency measurements of silicon nanoclusters," *Appl. Phys. Lett.*, vol. 73, no. 4, pp. 523–525, 1998.

[45] M. Perego, M. Fanciulli, C. Bonafos, and N. Cherkashin, "Synthesis of mono and bi-layer of Si nanocrystals embedded in a dielectric matrix by e-beam evaporation of SiO/SiO2 thin films," *Mater. Sci. Eng. C*, vol. 26, no. 5–7, pp. 835–839, 2006.

[46] M. Perego, G. Seguini, C. Wiemer, M. Fanciulli, P.-E. Coulon, and C. Bonafos, "Si nanocrystal synthesis in HfO2/SiO/HfO2 multilayer structures.," *Nanotechnology*, vol. 21, no. 5, p. 055606, 2010.

[47] H. Seifarth, R. Grötzschel, A. Markwitz, W. Matz, P. Nitzsche, and L. Rebohle, "Preparation of SiO2 films with embedded Si nanocrystals by reactive r.f. magnetron sputtering," *Thin Solid Films*, vol. 330, no. 2, pp. 202–205, 1998.

[48] M. Zacharias, H. Freistedt, F. Stolze, T. P. Drusedau, M. Rosenbauer, and M. Stutzmann, "Properties of sputtered a-SiOx:H alloys with a visible luminescence," *J. Non. Cryst. Solids*, vol. 164–166, no. 2, pp. 1089–1092, 1993.

[49] S. Furukawa and T. Miyasato, "Quantum size effects on the optical band gap of microcrystalline Si: H," *Phys. Rev. B*, vol. 38, no. 8, pp. 5726–5729, 1988.

[50] J. Valenta, R. Juhasz, and J. Linnros, "Photoluminescence spectroscopy of single silicon quantum dots," *Appl. Phys. Lett.*, vol. 80, no. 6, pp. 1070–1072, 2002.

[51] B. Han, Y. Shimizu, G. Seguini, E. Arduca, C. Castro, G. Ben Assayag, K. Inoue, Y. Nagai, S. Schamm-Chardon, and M. Perego, "Evolution of shape, size, and areal density of a single plane of Si nanocrystals embedded in SiO 2 matrix studied by atom probe tomography," *RSC Adv.*, vol. 6, pp. 3617–3622, 2016.

[52] T. Shimizu-Iwayama, Y. Terao, A. Kamiya, M. Takeda, S. Nakao, and K. Saitoh, "Novel

approach for synthesizing of nanometer-sized Si crystals in SiO2 by ion implantation and their optical characterization," *Nucl. Instruments Methods Phys. Res. Sect. B Beam Interact. with Mater. Atoms*, vol. 112, pp. 214–218, 1996.

[53] P. Dimitrakis, E. Kapetanakis, D. Tsoukalas, D. Skarlatos, C. Bonafos, G. Ben Asssayag, A. Claverie, M. Perego, M. Fanciulli, V. Soncini, R. Sotgiu, A. Agarwal, M. Ameen, C. Sohl, and P. Normand, "Silicon nanocrystal memory devices obtained by ultra-low-energy ion-beam synthesis," *Solid. State. Electron.*, vol. 48, no. 9, pp. 1511–1517, 2004.

[54] N. Cherkashin, C. Bonafos, H. Coffin, M. Carrada, S. Schamm, G. Ben Assayag, D. Chassaing, P. Dimitrakis, P. Normand, M. Perego, M. Fanciulli, T. Muller, K. H. Heinig, and A. Claverie, "Fabrication of nanocrystal memories by ultra low energy ion implantation," *Phys. Status Solidi*, vol. 2, no. 6, pp. 1907–1911, 2005.

[55] A. A. D. T. Adikaari, D. M. N. M. Dissanayake, R. A. Hatton, and S. R. P. Silva, "Efficient laser textured nanocrystalline silicon-polymer bilayer solar cells," *Appl. Phys. Lett.*, vol. 90, no. 20, p. 203514, 2007.

[56] O. M. Nayfeh, S. Rao, A. Smith, J. Therrien, and M. H. Nayfeh, "Thin film silicon nanoparticle UV photodetector," *IEEE Photonics Technol. Lett.*, vol. 16, no. 8, pp. 1927–1929, 2004.

[57] V. Svrcek, I. Pelant, J. Rehspringer, P. Gilliot, D. Ohlmann, and O. Cregut, "Photoluminescence properties of sol – gel derived SiO2 layers doped with porous silicon," *Mater. Sci. Eng. C*, vol. 19, pp. 233–236, 2002.

[58] M. L. Ostraat, J. W. De Blauwe, M. L. Green, L. D. Bell, H. A. Atwater, and R. C. Flagan, "Ultraclean Two-Stage Aerosol Reactor for Production of Oxide-Passivated Silicon Nanoparticles for Novel Memory Devices," *J. Electrochem. Soc.*, vol. 148, no. 5, pp. G265–G270, 2001.

[59] X. Li, Y. He, S. S. Talukdar, and M. T. Swihart, "Process for preparing macroscopic quantities of brightly photoluminescent silicon nanoparticles with emission spanning the visible spectrum," *Langmuir*, vol. 19, pp. 8490–8496, 2003.

[60] L. Mangolini, E. Thimsen, and U. Kortshagen, "High-Yield Plasma Synthesis of Luminescent Silicon Nanocrystals," *Nano Lett.*, vol. 5, no. 4, pp. 655–659, 2005.

[61] R. M. Sankaran, D. Holunga, R. C. Flagan, and K. P. Giapis, "Synthesis of blue luminescent Si nanoparticles using atmospheric-pressure microdischarges," *Nano Lett.*, vol. 5, no. 3, pp. 537–541, 2005.

[62] T. Nozaki, K. Sasaki, T. Ogino, D. Asahi, and K. Okazaki, "Microplasma synthesis of tunable photoluminescent silicon nanocrystals," *Nanotechnology*, vol. 18, p. 235603, 2007.

[63] M. S. Dresselhaus, G. Chen, M. Y. Tang, R. Yang, H. Lee, D. Wang, Z. Ren, J. P. Fleurial, and P. Gogna, "New directions for low-dimensional thermoelectric materials," *Adv. Mater.*, vol. 19, pp. 1043–1053, 2007.

[64] R. Lechner, H. Wiggers, A. Ebbers, J. Steiger, M. S. Brandt, and M. Stutzmann,

"Thermoelectric effect in laser annealed printed nanocrystalline silicon layers," *Phys. Status Solidi - Rapid Res. Lett.*, vol. 1, no. 6, pp. 262–264, 2007.

[65] A. Datta, S. Oda, F. U. Ying, and M. W. Willander, "Electron Transport in Nanocrystalline Si Based Single Electron Transistors," *Jpn. J. Appl. Phys.*, vol. 39, pp. 4647–4650, 2000.

[66] K. Nishiguchi and S. Oda, "Electron transport in a single silicon quantum structure using a vertical silicon probe," *J. Appl. Phys.*, vol. 88, no. 7, p. 4186, 2000.

[67] C.-Y. Liu, Z. C. Holman, and U. R. Kortshagen, "Hybrid Solar Cells from P3HT and Silicon Nanocrystals," *Nano Lett.*, vol. 9, no. 1, p. 449, 2009.

[68] K. Nishiguchi, X. Zhao, and S. Oda, "Nanocrystalline silicon electron emitter with a high efficiency enhanced by a planarization technique," *J. Appl. Phys.*, vol. 92, no. 5, pp. 2748–2757, 2002.

[69] D. Jurbergs, E. Rogojina, L. Mangolini, and U. Kortshagen, "Silicon nanocrystals with ensemble quantum yields exceeding 60%," *Appl. Phys. Lett.*, vol. 88, no. 23, p. 233116, 2006.

[70] K. A. Littau, P. Szajowski, J. Muller, A. Kortan, and L. Brus, "A luminescent Silicon Nanocrystal colloid via a High-Temperature Aereosol Reaction," *J. Phys. Chem.*, vol. 97, no. 69, p. 1224, 1993.

[71] Q. Xu, J. W. Luo, S. S. Li, J. B. Xia, J. Li, and S. H. Wei, "Chemical trends of defect formation in Si quantum dots: The case of group-III and group-V dopants," *Phys. Rev. B - Condens. Matter Mater. Phys.*, vol. 75, no. 23, pp. 1–6, 2007.

[72] M. G. Mavros, D. a. Micha, and D. S. Kilin, "Optical Properties of Doped Silicon Quantum Dots with Crystalline and Amorphous Structures," *J. Phys. Chem. C*, vol. 115, no. 40, pp. 19529–19537, 2011.

[73] A. M. Hartel, D. Hiller, S. Gutsch, P. Löper, S. Estradé, F. Peiró, B. Garrido, and M. Zacharias, "Formation of size-controlled silicon nanocrystals in plasma enhanced chemical vapor deposition grown SiOxNy/SiO2 superlattices," *Thin Solid Films*, vol. 520, pp. 121–125, 2011.

[74] J. H. Warner, A. Hoshino, K. Yamamoto, and R. D. Tilley, "Water-soluble photoluminescent silicon quantum dots," *Angew. Chemie - Int. Ed.*, vol. 44, pp. 4550–4554, 2005.

[75] M. Zacharias, J. Heitmann, R. Scholz, U. Kahler, M. Schmidt, and J. Blasing, "Size-controlled highly luminescent silicon nanocrystals: A SiO/SiO 2 superlattice approach," *Appl. Phys. Lett.*, vol. 80, no. 4, pp. 661–663, 2002.

[76] R. Guerra, E. Degoli, and S. Ossicini, "Size , oxidation , and strain in small Si/SiO2 nanocrystals," *Phys. Rev. B*, vol. 80, no. 15, p. 155332, 2009.

[77] D. König, J. Rudd, M. A. Green, and G. Conibeer, "Role of the interface for the electronic structure of Si quantum dots," *Phys. Rev. B*, vol. 78, no. 3, p. 035339, 2008.

[78] C. Delerue, G. Allan, and M. Lannoo, "Theoretical aspects of the luminescence of porous silicon," *Phys. Rev. B*, vol. 48, no. 15, p. 1124, 1993.

[79] P. Hapala, K. Kusova, I. Pelant, and P. Jelinek, "Theoretical analysis of electronic band structure of 2- to 3-nm Si nanocrystals," *Phys. Rev. B*, vol. 87, no. 19, p. 1954, 2013.

[80] S. Gutsch, J. Laube, D. Hiller, W. Bock, M. Wahl, M. Kopnarski, H. Gnaser, B. Puthen-Veettil, and M. Zacharias, "Electronic properties of phosphorus doped silicon nanocrystals embedded in SiO2," *Appl. Phys. Lett.*, vol. 106, no. 11, p. 113103, 2015.

[81] D. König, S. Gutsch, H. Gnaser, M. Wahl, M. Kopnarski, J. Göttlicher, R. Steininger, M. Zacharias, and D. Hiller, "Location and Electronic Nature of Phosphorus in the Si Nanocrystal--SiO2 System," *Sci. Rep.*, vol. 5, p. 09702, 2015.

[82] E. Arduca and M. Perego, "Doping of silicon nanocrystals," *Mater. Sci. Semicond. Process.*, no. August, pp. 1–15, 2016.

[83] X. D. Pi, R. Gresback, R. W. Liptak, S. A. Campbell, and U. Kortshagen, "Doping efficiency, dopant location, and oxidation of Si nanocrystals," *Appl. Phys. Lett.*, vol. 92, no. 12, pp. 1–4, 2008.

[84] Y. Ma, X. Chen, X. Pi, and D. Yang, "Lightly boron and phosphorus co-doped silicon nanocrystals," *J. Nanoparticle Res.*, vol. 14, p. 802, 2012.

[85] X. Chen, X. Pi, and D. Yang, "Critical role of dopant location for P-doped Si nanocrystals," *J. Phys. Chem. C*, vol. 115, no. 3, pp. 661–666, 2011.

[86] X. Pi, X. Chen, and D. Yang, "First-principles study of 2.2 nm silicon nanocrystals doped with boron," *J. Phys. Chem. C*, vol. 115, no. 20, pp. 9838–9843, 2011.

[87] X. Pi, "Doping silicon nanocrystals with boron and phosphorus," *J. Nanomater.*, vol. 2012, 2012.

[88] A. Mimura, M. Fujii, S. Hayashi, and K. Yamamoto, "Photoluminescence from Si nanocrystals dispersed in phosphosilicate glass thin films," *J. Lumin.*, vol. 87, no. 1999, pp. 429–431, 2000.

[89] G. A. Kachurin, S. G. Yanovskaya, D. I. Tetelbaum, and A. N. Mikhailov, "The Effect of implantation of P Ions on the photoluminescence of Si nanocrystals in a SiO2 layers," *Semiconductors*, vol. 37, no. 6, p. 713, 2003.

[90] Y. Kanzawa, M. Fujii, S. Hayashi, and K. Yamamotob, "Doping of B atoms into Si nanocrystals prepared by RF cosputtering," *Solid State Commun.*, vol. 100, no. 4, pp. 227–230, 1996.

[91] R. Lechner, A. R. Stegner, R. N. Pereira, R. Dietmueller, M. S. Brandt, A. Ebbers, M. Trocha, H. Wiggers, and M. Stutzmann, "Electronic properties of doped silicon nanocrystal films," *J. Appl. Phys.*, vol. 104, no. 5, p. 05370, 2008.

[92] J. H. Eom, T. L. Chan, and J. R. Chelikowsky, "Vacancies and B doping in Si nanocrystals," *Solid State Commun.*, vol. 150, pp. 130–132, 2010.

[93] G. Cantele, E. Degoli, E. Luppi, R. Magri, D. Ninno, G. Iadonisi, and S. Ossicini, "First-

principles study of n- and p-doped silicon nanoclusters," *Phys. Rev. B - Condens. Matter Mater. Phys.*, vol. 72, no. 11, p. 113303, 2005.

[94] F. Iori, E. Degoli, R. Magri, I. Marri, G. Cantele, D. Ninno, F. Trani, O. Pulci, and S. Ossicini, "Engineering silicon nanocrystals: Theoretical study of the effect of codoping with boron and phosphorus," *Phys. Rev. B - Condens. Matter Mater. Phys.*, vol. 76, no. 8, p. 085302, 2007.

[95] J. Ma, S. Wei, N. R. Neale, and A. J. Nozik, "Effect of surface passivation on dopant distribution in Si quantum dots : The case of B and P doping," *Appl. Phys. Lett.*, vol. 98, no. 17, p. 173103, 2011.

[96] A. Carvalho, S. Öberg, M. Barroso, M. J. Rayson, and P. Briddon, "Boron doped Si nanoparticles: the effect of oxidation," *Phys. Status Solidi basic solid state Phys.*, vol. 250, no. 9, pp. 1799–1803, 2013.

[97] A. Carvalho, B. Celikkol, J. Coutinho, and P. R. Briddon, "Surface-phosphorus interaction in Si nanocrystals," *J. Phys. Conf. Ser.*, vol. 281, p. 012027, 2011.

[98] X. D. Pi, R. Gresback, R. W. Liptak, S. A. Campbell, and U. Kortshagen, "Doping efficiency, dopant location, and oxidation of Si nanocrystals," *Appl. Phys. Lett.*, vol. 92, no. 12, pp. 23–25, 2008.

[99] A. R. Stegner, R. N. Pereira, R. Lechner, K. Klein, H. Wiggers, M. Stutzmann, and M. S. Brandt, "Doping efficiency in freestanding silicon nanocrystals from the gas phase: Phosphorus incorporation and defect-induced compensation," *Phys. Rev. B - Condens. Matter Mater. Phys.*, vol. 80, no. 16, pp. 1–10, 2009.

[100] G. Polisski, D. Kovalev, G. Dollinger, T. Sulima, and F. Koch, "Boron in mesoporous Si - where have all the carriers gone?," *Phys. B Condens. Matter*, vol. 273–274, pp. 951–954, 1999.

[101] B. P. Veettil, L. Wu, X. Jia, Z. Lin, T. Zhang, T. Yang, C. Johnson, D. McCamey, G. Conibeer, and I. Perez-würfl, "Passivation effects in B doped self-assembled Si nanocrystals," *Appl. Phys. Lett.*, vol. 105, no. 22, p. 222108, 2014.

[102] J. P. Petropoulos, T. R. Cristiani, P. B. Dongmo, and J. M. O. Zide, "A simple thermodynamic model for the doping and alloying of nanoparticles.," *Nanotechnology*, vol. 22, no. 24, p. 245704, 2011.

[103] T. L. Chan, S. B. Zhang, and J. R. Chelikowsky, "An effective one-particle theory for formation energies in doping Si nanostructures," *Appl. Phys. Lett.*, vol. 98, no. 13, p. 133116, 2011.

[104] T. Chan, M. L. Tiago, E. Kaxiras, and J. R. Chelikowsky, "Size Limits on Doping Phosphorus into Silicon Nanocrystals," *Nano Lett.*, vol. 8, no. 2, pp. 596–600, 2008.

[105] S. C. Erwin, L. Zu, M. I. Haftel, A. L. Efros, T. a Kennedy, and D. J. Norris, "Doping semiconductor nanocrystals," *Nature*, vol. 436, pp. 91–94, 2005.

[106] S. Ossicini, E. Degoli, F. Iori, E. Luppi, R. Magri, G. Cantele, F. Trani, and D. Ninno, "Simultaneously B- and P-doped silicon nanoclusters: Formation energies and

electronic properties," *Appl. Phys. Lett.*, vol. 87, no. 17, pp. 1–3, 2005.

[107] L. Mangolini and U. Kortshagen, "Plasma-assisted synthesis of silicon nanocrystal inks," *Adv. Mater.*, vol. 19, pp. 2513–2519, 2007.

[108] R. Gresback, T. Nozaki, and K. Okazaki, "Synthesis and oxidation of luminescent silicon nanocrystals from silicon tetrachloride by very high frequency nonthermal plasma," *Nanotechnology*, vol. 22, p. 305605, 2011.

[109] N. Garcia-Castello, S. Illera, J. D. Prades, S. Ossicini, A. Cirera, and R. Guerra, "Energetics and carrier transport in doped Si/SiO2 quantum dots," *Nanoscale*, vol. 7, pp. 12564–71, 2015.

[110] R. N. Pereira and a J. Almeida, "Doped semiconductor nanoparticles synthesized in gas-phase plasmas," *J. Phys. D. Appl. Phys.*, vol. 48, no. 31, p. 314005, 2015.

[111] Z. Ni, X. Pi, M. Ali, S. Zhou, T. Nozaki, and D. Yang, "Freestanding doped silicon nanocrystals synthesized by plasma," *J. Phys. D. Appl. Phys.*, vol. 48, no. 31, p. 314006, 2015.

[112] J. Knipping, H. Wiggers, B. Rellinghaus, P. Roth, D. Konjhodzic, and C. Meier, "Synthesis of high purity silicon nanoparticles in a low pressure microwave reactor," *J. Nanosci. Nanotechnol.*, vol. 4, no. 8, pp. 1039–1044, 2004.

[113] S. Zhou, X. Pi, Z. Ni, Q. Luan, Y. Jiang, C. Jin, T. Nozaki, and D. Yang, "Boron- and phosphorus-hyperdoped silicon nanocrystals," *Part. Part. Syst. Charact.*, vol. 32, no. 2, pp. 213–221, 2015.

[114] Borowik, T. Nguyen-Tran, P. Roca I Cabarrocas, and T. Mélin, "Doped semiconductor nanocrystal junctions," *J. Appl. Phys.*, vol. 114, no. 20, p. 204305, 2013.

[115] K. Someno, K. Usami, T. Kodera, Y. Kawano, M. Hatano, and S. Oda, "Photoluminescence of nanocrystalline silicon quantum dots with various sizes and various phosphorus doping concentrations prepared by very high frequency plasma," *Jpn. J. Appl. Phys.*, vol. 51, no. 11, p. 115202, 2012.

[116] A. Becker, G. Schierning, R. Theissmann, M. Meseth, N. Benson, R. Schmechel, D. Schwesig, N. Petermann, H. Wiggers, and P. Ziolkowski, "A sintered nanoparticle p-n junction observed by a Seebeck microscan," *J. Appl. Phys.*, vol. 111, no. 5, p. 054320, 2012.

[117] S. Zhou, Y. Ding, X. Pi, and T. Nozaki, "Doped silicon nanocrystals from organic dopant precursor by a SiCl4-based high frequency nonthermal plasma," *Appl. Phys. Lett.*, vol. 105, no. 18, pp. 2012–2017, 2014.

[118] A. R. Stegner, R. N. Pereira, K. Klein, R. Lechner, R. Dietmueller, M. S. Brandt, M. Stutzmann, and H. Wiggers, "Electronic transport in phosphorus-doped silicon nanocrystal networks," *Phys. Rev. Lett.*, vol. 100, no. 2, pp. 18–21, 2008.

[119] R. Lechner, A. R. Stegner, R. N. Pereira, R. Dietmueller, M. S. Brandt, A. Ebbers, M. Trocha, H. Wiggers, and M. Stutzmann, "Electronic properties of doped silicon nanocrystal films," *J. Appl. Phys.*, vol. 104, no. 5, 2008.

[120] M. Meseth, K. Lamine, M. Dehnen, S. Kayser, W. Brock, D. Behrenberg, H. Orthner, A. Elsukova, N. Hartmann, H. Wiggers, T. Hulser, H. Nienhaus, N. Benson, and R. Schmechel, "Laser-doping of crystalline silicon substrates using doped silicon nanoparticles," *Thin Solid Films*, vol. 548, pp. 437–442, 2013.

[121] A. R. Stegner, R. N. Pereira, K. Klein, H. Wiggers, M. S. Brandt, and M. Stutzmann, "Phosphorus doping of Si nanocrystals: Interface defects and charge compensation," *Phys. B Condens. Matter*, vol. 401–402, pp. 541–545, 2007.

[122] Y. Nakamine, N. Inaba, T. Kodera, K. Uchida, R. N. Pereira, A. R. Stegner, M. S. Brandt, M. Stutzman, and S. Oda, "Size reduction and phosphorus doping of silicon nanocrystals prepared by a very high frequency plasma deposition system," *Jpn. J. Appl. Phys.*, vol. 50, no. 2, pp. 2–7, 2011.

[123] H. Kodera, "Constitutional Supercooling during the Crystal Growth of Germanium and Silicon," *Jpn. J. Appl. Phys.*, vol. 2, no. 9, pp. 527–534, 1963.

[124] R. K. Baldwin, J. Zou, K. a Pettigrew, G. J. Yeagle, R. D. Britt, and S. M. Kauzlarich, "The preparation of a phosphorus doped silicon film from phosphorus containing silicon nanoparticles," *Chem. Commun.*, pp. 658–660, 2006.

[125] K. Fujio, M. Fujii, K. Sumida, S. Hayashi, M. Fujisawa, and H. Ohta, "Electron spin resonance studies of P and B codoped Si nanocrystals," *Appl. Phys. Lett.*, vol. 93, no. 2, p. 021920, 2008.

[126] P. G. Han, Z. Y. Ma, Z. B. Wang, and X. Zhang, "Photoluminescence from intermediate phase silicon structure and nanocrystalline silicon in plasma enhanced chemical vapor deposition grown Si / SiO 2 multilayers," *Nanotechnology*, vol. 19, p. 325708, 2008.

[127] M. Ishii, I. F. Crowe, M. P. Halsall, A. P. Knights, R. M. Gwilliam, and B. Hamilton, "Luminescence quenching of conductive Si nanocrystals via ' Linkage emission ': Hopping-like propagation of infrared-excited Auger electrons," *J. Appl. Phys.*, vol. 116, no. 06, p. 063513, 2014.

[128] I. Sychugov, J. Valenta, K. Mitsuishi, and J. Linnros, "Exciton localization in doped Si nanocrystals from single dot spectroscopy studies," *Phys. Rev. B*, vol. 86, p. 075311, 2012.

[129] M. Fujii, S. Hayashi, K. Yamamoto, M. Fujii, S. Hayashi, and K. Yamamoto, "Photoluminescence from B-doped Si nanocrystals," *J. Appl. Phys.*, vol. 83, no. 12, p. 7953, 1998.

[130] M. Xie, D. Li, L. Chen, F. Wang, X. Zhu, and D. Yang, "The location and doping effect of boron in Si nanocrystals embedded silicon oxide film," *Appl. Phys. Lett.*, vol. 102, p. 123108, 2013.

[131] M. Fujii, A. Mimura, S. Hayashi, and K. Yamamoto, "Photoluminescence from Si nanocrystals dispersed in phosphosilicate glass thin films : Improvement of photoluminescence efficiency," *Appl. Phys. Lett.*, vol. 75, no. 2, p. 184, 1999.

[132] A. Mimura, D. Kovalev, and F. Koch, "Photoluminescence and free-electron absorption in heavily phosphorus-doped Si nanocrystals," *Phys. Rev.*, vol. 62, no. 19,

pp. 625–627, 2000.

[133] M. Fujii, Y. Yamaguchi, Y. Takase, K. Ninomiya, and S. Hayashi, "Control of photoluminescence properties of Si nanocrystals by simultaneously doping n - and p -type impurities," *Appl. Phys. Lett.*, vol. 85, no. 7, p. 1158, 2004.

[134] K. Nomoto, H. Sugimoto, A. Breen, A. V Ceguerra, T. Kanno, S. P. Ringer, I. Perez, G. Conibeer, and M. Fujii, "Atom Probe Tomography Analysis of Boron and/or Phosphorus Distribution in Doped Silicon Nanocrystals," *J. Phys. Chem. C*, vol. 120, pp. 17845–17852, 2016.

[135] S. Gutsch, a. M. Hartel, D. Hiller, N. Zakharov, P. Werner, and M. Zacharias, "Doping efficiency of phosphorus doped silicon nanocrystals embedded in a SiO2 matrix," *Appl. Phys. Lett.*, vol. 100, no. 23, p. 233115, 2012.

[136] C. Eun-Chel, P. Sangwook, H. Xiaojing, S. Dengyuan, C. Gavin, P. Sang-Cheol, and A. G. Martin, "Silicon quantum dot/crystalline silicon solar cells," *Nanotechnology*, vol. 19, no. 24, p. 245201, 2008.

[137] A. I. Kovalev, D. L. Wainstein, D. I. Tetelbaum, W. Hornig, and Y. N. Kucherehko, "Investigation of the electronic structure of the phosphorus-doped Si and SiO2: Si quantum dots by XPS and HREELS methods," *Surf. Interface Anal.*, vol. 36, pp. 959–962, 2004.

[138] K. Murakami, R. Shirakawa, M. Tsujimura, N. Uchida, N. Fukata, and S. I. Hishita, "Phosphorus ion implantation in silicon nanocrystals embedded in SiO2," *J. Appl. Phys.*, vol. 105, no. 5, pp. 1–6, 2009.

[139] A. L. Tchebotareva, M. J. A. De Dood, J. S. Biteen, H. A. Atwater, and A. Polman, "Quenching of Si nanocrystal photoluminescence by doping with gold or phosphorous," *J. Lumin.*, vol. 114, no. 2, pp. 137–144, 2005.

[140] M. Mastromatteo, E. Arduca, E. Napolitani, G. Nicotra, D. De Salvador, L. Bacci, J. Frascaroli, G. Seguini, M. Scuderi, G. Impellizzeri, C. Spinella, M. Perego, and A. Carnera, "Quantification of phosphorus diffusion and incorporation in silicon nanocrystals embedded in silicon oxide," *Surf. Interface Anal.*, vol. 46, pp. 393–396, Nov. 2014.

[141] M. Mastromatteo, E. Arduca, E. Napolitani, G. Nicotra, D. De Salvador, L. Bacci, J. Frascaroli, G. Seguini, M. Scuderi, G. Impellizzeri, C. Spinella, M. Perego, and A. Carnera, "Modeling of phosphorus diffusion in silicon oxide and incorporation in silicon nanocrystals," *J. Mater. Chem. C*, vol. 4, p. 3531, 2016.

[142] U. Fano, "Effects of configuration interaction on intensities and phase shifts," *Phys. Rev.*, vol. 124, no. 6, pp. 1866–1878, 1961.

[143] S. Zhou, X. Pi, Z. Ni, Y. Ding, Y. Jiang, C. Jin, and C. Delerue, "Comparative Study on the Localized Surface Plasmon Resonance Silicon Nanocrystals," *ACS Nano*, vol. 9, no. 1, pp. 378–386, 2015.

[144] A. J. Almeida, H. Sugimoto, M. Fujii, M. S. Brandt, M. Stutzmann, and R. N. Pereira, "Doping efficiency and confinement of donors in embedded and free standing Si

nanocrystals," *Phys. Rev. B - Condens. Matter Mater. Phys.*, vol. 93, no. 11, p. 115425, 2016.

[145] R. N. Pereira, S. Niesar, W. B. You, A. F. Da Cunha, N. Erhard, A. R. Stegner, H. Wiggers, M. G. Willinger, M. Stutzmann, and M. S. Brandt, "Solution-processed networks of silicon nanocrystals: The role of internanocrystal medium on semiconducting behavior," *J. Phys. Chem. C*, vol. 115, no. 41, pp. 20120–20127, 2011.

[146] Y. Lin and X. Chen, "Electron beam Evaporation Deposition," in *Advanced Nano Deposition methods*, 2016, pp. 305–309.

[147] A. K. Cheetham and P. Day, *Solid State Chemistry: Techniques*, vol. 1. 1987.

[148] K. Hinrichs, M. Gensch, and N. Esser, "Analysis of Organic Films and Interfacial Layers by Infrared Spectroscopic Ellipsometry," *Appl. Spectrosc.*, vol. 59, no. 11, p. 272A–282A, 2005.

[149] G. Jellison, G. Irene, and H. Tompkins, *Handbook of ellipsometry*. 2005.

[150] K. Words and W. Sigle, *Analytical Transmission Electron Microscopy*. 2001.

[151] M. Miller and G. Smith, *Atom probe microanalysis: principles and applications to materials problems*. 1989.

[152] S. Nagamachi, M. Ueda, and J. Ishikawa, "Focused ion beam direct deposition and its applications," *J. Vac. Sci. Technol. B Microelectron. Process. Phenom.*, vol. 16, no. 4, pp. 2515–2521, 1998.

[153] T. F. Kelly, D. J. Larson, K. Thompson, R. L. Alvis, J. H. Bunton, J. D. Olson, and B. P. Gorman, "Atom probe tomography of electronic materials," *Annu. Rev. Mater. Res.*, vol. 37, pp. 681–727, 2007.

[154] T. F. Kelly and D. J. Larson, "Atom Probe Tomography 2012," *Annu. Rev. Mater. Res.*, vol. 42, pp. 1–31, 2012.

[155] P. A. W. Van Der Heide, "Caesium enhancement effect observed during SIMS ultra shallow depth profile analysis of SiO2 on Si," *Appl. Surf. Sci.*, vol. 157, no. 3, pp. 191–198, 2000.

[156] P. A. W. Van Der Heide, "Cesium-induced transient e ff ects on the Si + and Si − secondary ion emissions from Si and SiO," *Surf. Sci.*, vol. 447, pp. 62–72, 2000.

[157] K. Iltgen, C. Bendel, A. Benninghoven, and E. Niehuis, "Optimized time-of-flight secondary ion mass spectroscopy depth profiling with a dual beam technique," *J. Vac. Sci. Technol. A Vacuum, Surfaces, Film.*, vol. 15, no. 3, pp. 460–464, 1997.

[158] J. G. M. van Berkum, "Secondary ion mass spectrometry depth profiling of ultralow-energy ion implants: Problems and solutions," *J. Vac. Sci. Technol. B Microelectron. Nanom. Struct.*, vol. 16, no. 1, p. 298, 1998.

[159] M. Perego, S. Ferrari, S. Spiga, E. Bonera, M. Fanciulli, and V. Soncini, "Time of flight secondary ion mass spectrometry study of silicon nanoclusters embedded in thin silicon oxide layers," *Appl. Phys. Lett.*, vol. 82, no. 1, pp. 121–123, 2003.

[160] P. Borgesen, "Rutherford Backscattering Spectrometry (RBS)," in *Analysis of Microelectronics Materials and Devices*, 1991.

[161] D. Briggs and M. P. Seah, *Pratical Surface Analysis. Volume 1: Auger and X-ray Photoelectron Spectroscopy*. 1990.

[162] C. J. Powell, "Measurement of silicon dioxide film thicknesses by X-ray photoelectron spectroscopy," *AIP Conf. Proc.*, vol. 550, pp. 591–595, 2001.

[163] a Jablonski and C. . Powell, "Relationships between electron inelastic mean free paths, effective attenuation lengths, and mean escape depths," *J. Electron Spectros. Relat. Phenomena*, vol. 100, pp. 137–160, 1999.

[164] P. J. Cumpson, "Angle-resolved XPS and AES: Depth-resolution limits and a general comparison of properties of depth-profile reconstruction methods," *J. Electron Spectros. Relat. Phenomena*, vol. 73, no. 1, pp. 25–52, 1995.

[165] P. J. Cumpson, "Angle-resolved XPS depth-profiling strategies," *Appl. Surf. Sci.*, vol. 144–145, pp. 16–20, 1999.

[166] J. C. Ho, R. Yerushalmi, Z. a Jacobson, Z. Fan, R. L. Alley, and A. Javey, "Controlled nanoscale doping of semiconductors via molecular monolayers.," *Nat. Mater.*, vol. 7, no. 1, pp. 62–7, Jan. 2008.

[167] T. Shinada, S. Okamoto, T. Kobayashi, and I. Ohdomari, "Enhancing semiconductor device performance using ordered dopant arrays.," *Nature*, vol. 437, no. 7062, pp. 1128–31, Oct. 2005.

[168] W. P. Voorthuijzen, M. D. Yilmaz, W. J. M. Naber, J. Huskens, and W. G. van der Wiel, "Local doping of silicon using nanoimprint lithography and molecular monolayers.," *Adv. Mater.*, vol. 23, pp. 1346–50, Mar. 2011.

[169] W. P. Voorthuijzen, M. D. Yilmaz, A. Gomez-Casado, P. Jonkheijm, W. G. van der Wiel, and J. Huskens, "Direct patterning of covalent organic monolayers on silicon using nanoimprint lithography.," *Langmuir*, vol. 26, no. 17, pp. 14210–5, Sep. 2010.

[170] R. a. Puglisi, C. Garozzo, C. Bongiorno, S. Di Franco, M. Italia, G. Mannino, S. Scalese, and A. La Magna, "Molecular doping applied to Si nanowires array based solar cells," *Sol. Energy Mater. Sol. Cells*, vol. 132, no. SEPTEMBER, pp. 118–122, Jan. 2015.

[171] B. Long, G. A. Verni, J. O'Connel, and J. Holmes, "Molecular Layer Doping: Non-destructive doping of silicon and germanium," *… (IIT), 2014 20th …*, 2014.

[172] J. Ho, R. Yerushalmi, G. Smith, and P. Majhi, "Wafer-scale, sub-5 nm junction formation by monolayer doping and conventional spike annealing," *Nano Lett.*, vol. 9, no. 2, pp. 725–730, 2009.

[173] A. Ford, J. Ho, Y. Chueh, and A. Javey, "Monolayer doping and diameter-dependent electron mobility assessment of nanowires," *IC Des. Technol. …*, no. 510, pp. 1–5, 2009.

[174] G. Collins, P. Fleming, S. Barth, C. O'Dwyer, J. J. Boland, M. A. Morris, and J. D. Holmes,

"Alkane and alkanethiol passivation of halogenated ge nanowires," *Chem. Mater.*, vol. 22, pp. 6370–6377, 2010.

[175] G. Collins, P. Fleming, C. O'Dwyer, M. A. Morris, and J. D. Holmes, "Organic functionalization of germanium nanowires using arenediazonium salts," *Chem. Mater.*, vol. 23, pp. 1883–1891, 2011.

[176] J. S. Kachian, K. T. Wong, and S. F. Bent, "Periodic trends in organic functionalization of group IV semiconductor surfaces," *Acc. Chem. Res.*, vol. 43, no. 2, pp. 346–355, 2010.

[177] J. H. Yum, H. S. Shin, R. Hill, J. Oh, H. D. Lee, R. M. Mushinski, T. W. Hudnall, C. W. Bielawski, S. K. Banerjee, W. Y. Loh, W. E. Wang, and P. Kirsch, "A study of capping layers for sulfur monolayer doping on III-V junctions," *Appl. Phys. Lett.*, vol. 101, no. 25, p. 253514, 2012.

[178] E. Arduca, M. Mastromatteo, D. De Salvador, G. Seguini, C. Lenardi, and E. Napolitani, "Synthesis and characterization of P δ -layer in SiO 2 by monolayer doping," *Nanotechnology*, vol. 27, no. 7, p. 75606, 2016.

[179] Y. Shimizu, H. Takamizawa, K. Inoue, F. Yano, Y. Nagai, L. Lamagna, G. Mazzeo, M. Perego, and E. Prati, "Behavior of phosphorous and contaminants from molecular doping combined with a conventional spike annealing method.," *Nanoscale*, vol. 6, no. 2, pp. 706–10, Jan. 2014.

[180] O. Hazut, A. Agarwala, I. Amit, and T. Subramani, "Contact doping of silicon wafers and nanostructures with phosphine oxide monolayers," *ACS Nano*, vol. 6, no. 11, pp. 10311–10318, 2012.

[181] L. Ye, S. P. Pujari, H. Zuilhof, T. Kudernac, M. P. de Jong, W. G. van der Wiel, and J. Huskens, "Controlling the dopant dose in silicon by mixed-monolayer doping.," *ACS Appl. Mater. Interfaces*, vol. 7, pp. 3231–6, Feb. 2015.

[182] L. Mathey, T. Alphazan, M. Valla, L. Veyre, H. Fontaine, V. Enyedi, K. Yckache, M. Danielou, S. Kerdiles, J. Guerrero, J.-P. Barnes, M. Veillerot, N. Chevalier, D. Mariolle, F. Bertin, C. Durand, M. Berthe, J. Dendooven, F. Martin, C. Thieuleux, B. Grandidier, and C. Copéret, "Functionalization of Silica Nanoparticles and Native Silicon Oxide with Tailored Boron-Molecular Precursors for Efficient and Predictive p -Doping of Silicon," *J. Phys. Chem. C*, vol. 119, no. 24, pp. 13750–13757, Jun. 2015.

[183] G. Seguini, T. J. Giammaria, F. F. Lupi, K. Sparnacci, D. Antonioli, V. Gianotti, F. Vita, I. F. Placentino, J. Hilhorst, C. Ferrero, O. Francescangeli, M. Laus, and M. Perego, "Thermally induced self-assembly of cylindrical nanodomains in low molecular weight PS-b-PMMA thin films.," *Nanotechnology*, vol. 25, no. 4, p. 045301, 2014.

[184] K. Sparnacci, D. Antonioli, V. Gianotti, M. Laus, F. Ferrarese Lupi, T. J. Giammaria, G. Seguini, and M. Perego, "Ultrathin Random Copolymer-Grafted Layers for Block Copolymer Self-Assembly," *ACS Appl. Mater. Interfaces*, vol. 7, pp. 10944–10951, 2015.

[185] F. Ferrarese Lupi, T. J. Giammaria, M. Ceresoli, G. Seguini, K. Sparnacci, D. Antonioli,

V. Gianotti, M. Laus, and M. Perego, "Rapid thermal processing of self-assembling block copolymer thin films," *Nanotechnology*, vol. 24, pp. 315601–3156, 2013.

[186] V. Gianotti, D. Antonioli, K. Sparnacci, M. Laus, C. Cassino, F. Marsano, G. Seguini, and M. Perego, "TGA-GC-MS Quantitative Analysis of Phosphorus-End Capped Functional Polymers in Bulk and Ultrathin Films," *Submitt. to Anal. Bioanal. Chem.*, 2017.

[187] K. Ang, J. Barnett, W. Loh, J. Huang, B. Min, P. Y. Hung, I. Ok, J. H. Yum, G. Bersuker, M. Rodgers, V. Kaushik, S. Gausepohl, C. Hobbs, P. D. Kirsch, and R. Jammy, "300mm FinFET Results Utilizing Conformal , Damage Free , Ultra Shallow Junctions (X j ~ 5nm) Formed with Molecular Monolayer Doping Technique," *Int. Electron Devices Meet. (Piscataway, NJ IEEE)*, pp. 837–840, 2011.

[188] K. S. Iyer, B. Zdyrko, H. Malz, J. Pionteck, and I. Luzinov, "Polystyrene layers grafted to macromolecular anchoring layer," *Macromolecules*, vol. 36, no. 17, pp. 6519–6526, 2003.

[189] E. Arduca, M. Mastromatteo, D. De Salvador, G. Seguini, C. Lenardi, E. Napolitani, and M. Perego, "Synthesis and characterization of P δ -layer in SiO 2 by monolayer doping," *Nanotechnology*, vol. 27, no. 7, p. 075606, 2016.

[190] D. J. Fisher, *Diffusion in Silicon - 10 Years of Research*. 2000.

[191] C. Bonafos, M. Carrada, N. Cherkashin, H. Coffin, D. Chassaing, G. Ben Assayag, A. Claverie, T. Müller, K. H. Heinig, M. Perego, M. Fanciulli, P. Dimitrakis, and P. Normand, "Manipulation of two-dimensional arrays of Si nanocrystals embedded in thin SiO 2 layers by low energy ion implantation," *J. Appl. Phys.*, vol. 95, no. 10, pp. 5696–5702, 2004.

[192] S. Schamm, C. Bonafos, H. Coffin, N. Cherkashin, M. Carrada, G. Ben Assayag, A. Claverie, M. Tencé, and C. Colliex, "Imaging Si nanoparticles embedded in SiO2 layers by (S)TEM-EELS," *Ultramicroscopy*, vol. 108, pp. 346–357, 2008.

[193] T. Müller, K. H. Heinig, W. Möller, C. Bonafos, H. Coffin, N. Cherkashin, G. Ben Assayag, S. Schamm, Q. Zanchi, A. Claverie, M. Tencé, and C. Colliex, "Multi-dot floating-gates for nonvolatile semiconductor memories: Their ion beam synthesis and morphology," *Appl. Phys. Lett.*, vol. 85, no. 12, pp. 2373–2375, 2004.

[194] B. Garrido Fernandez, M. López, C. García, A. Pérez-Rodríguez, J. R. Morante, C. Bonafos, M. Carrada, and A. Claverie, "Influence of average size and interface passivation on the spectral emission of Si nanocrystals embedded in SiO2," *J. Appl. Phys.*, vol. 91, no. 2, pp. 798–807, 2002.

[195] F. Iacona, G. Franzo, and C. Spinella, "Correlation between luminescence and structural properties of Si nanocrystals," *J. Appl. Phys.*, vol. 87, no. 3, pp. 1295–1303, 2000.

[196] G. Nicotra, S. Lombardo, C. Spinella, and G. Ammendola, "Observation of the nucleation kinetics of Si quantum dots on SiO 2 by energy filtered transmission electron microscopy," *Appl. Surf. Sci.*, vol. 205, pp. 304–308, 2003.

[197] M. Perego, A. Andreozzi, G. Seguini, S. Schamm-Chardon, C. Castro, and G.

BenAssayag, “Silicon crystallization in nanodot arrays organized by block copolymer lithography,” *J. Nanoparticle Res.*, vol. 16, p. 2775, 2014.

[198] A. Yurtsever, M. Weyland, and D. A. Muller, “Three-dimensional imaging of nonspherical silicon nanoparticles embedded in silicon oxide by plasmon tomography,” *Appl. Phys. Lett.*, vol. 89, no. 15, p. 151920, 2006.

[199] M. Roussel, E. Talbot, C. Pareige, R. Pratibha Nalini, F. Gourbilleau, and P. Pareige, “Confined phase separation in SiOx nanometric thin layers,” *Appl. Phys. Lett.*, vol. 103, no. 20, p. 203109, 2013.

[200] L. F. Kourkoutis, X. Hao, S. Huang, B. Puthen-Veettil, G. Conibeer, M. a Green, and I. Perez-Wurfl, “Three-dimensional imaging for precise structural control of Si quantum dot networks for all-Si solar cells,” *Nanoscale*, vol. 5, pp. 7499–7504, 2013.

[201] D. Friedrich, B. Schmidt, K. H. Heinig, B. Liedke, A. Mücklich, R. Hübner, D. Wolf, S. Kölling, and T. Mikolajick, “Sponge-like Si-SiO2 nanocomposite - Morphology studies of spinodally decomposed silicon-rich oxide,” *Appl. Phys. Lett.*, vol. 103, no. 13, p. 131911, 2013.

[202] K. (Tohoku U. . Inoue, H. (Tohoku U. . Takamizawa, Y. (Tohoku U. . Shimizu, F. (Tohoku U. . T. C. U. . Yano, T. (Tohoku U. . Toyama, A. (Renesas E. C. . Nishida, T. (Nec C. . Mogami, K. (Toray R. C. I. . Kitamoto, T. (Toray R. C. I. . Miyagi, J. (Toray R. C. I. . Kato, S. (Toray R. C. I. . Akahori, N. (Toshiba N. C. . Okada, M. (Toshiba N. C. . Kato, H. (Toshiba N. C. . Uchida, and Y. (Tohoku U. . Nagai, “Three-Dimensional Dopant Characterization of Actual Metal-Oxide-Semiconductor Devices of 65 nm Node by Atom Probe Tomography,” *Appl. Phys. Express*, vol. 6, p. 046502, 2013.

[203] B. Han, H. Takamizawa, Y. Shimizu, K. Inoue, Y. Nagai, F. Yano, Y. Kunimune, M. Inoue, and A. Nishida, “Phosphorus and boron diffusion paths in polycrystalline silicon gate of a trench-type three-dimensional metal-oxide-semiconductor field effect transistor investigated by atom probe tomography,” *Appl. Phys. Lett.*, vol. 107, no. 2, p. 023506, 2015.

[204] M. Roussel, E. Talbot, F. Gourbilleau, and P. Pareige, “Atomic characterization of Si nanoclusters embedded in SiO2 by atom probe tomography.,” *Nanoscale Res. Lett.*, vol. 6, no. 1, p. 164, 2011.

[205] M. Roussel, E. Talbot, R. Pratibha Nalini, F. Gourbilleau, and P. Pareige, “Phase transformation in SiOx/SiO2 multilayers for optoelectronics and microelectronics applications,” *Ultramicroscopy*, vol. 132, pp. 290–294, 2013.

[206] F. Vurpillot, B. Gault, B. P. Geiser, and D. J. Larson, “Reconstructing atom probe data: A review,” *Ultramicroscopy*, vol. 132, pp. 19–30, 2013.

[207] L. T. Stephenson, M. P. Moody, P. V. Liddicoat, and S. P. Ringer, “New Techniques for the Analysis of Fine-Scaled Clustering Phenomena within Atom Probe Tomography (APT) Data,” *Microsc. Microanal.*, vol. 13, p. 448, 2007.

[208] M. K. Miller and E. A. Kenik, “Atom Probe Tomography: A Technique for Nanoscale Characterization,” *Microsc. Microanal.*, vol. 10, no. 3, p. 336, 2004.

[209] J. M. Hyde, E. A. Marquis, K. B. Wilford, and T. J. Williams, "A sensitivity analysis of the maximum separation method for the characterisation of solute clusters," *Ultramicroscopy*, vol. 111, pp. 440–447, 2011.

[210] R. K. W. Marceau, L. T. Stephenson, C. R. Hutchinson, and S. P. Ringer, "Quantitative atom probe analysis of nanostructure containing clusters and precipitates with multiple length scales," *Ultramicroscopy*, vol. 111, pp. 738–742, 2011.

[211] E. A. Marquis and J. M. Hyde, "Applications of atom-probe tomography to the characterisation of solute behaviours," *Mater. Sci. Eng. R Reports*, vol. 69, pp. 37–62, 2010.

[212] T. Z. Lu, M. Alexe, R. Scholz, V. Talalaev, R. J. Zhang, and M. Zacharias, "Si nanocrystal based memories: Effect of the nanocrystal density," *J. Appl. Phys.*, vol. 100, no. 1, p. 014310, 2006.

[213] R. A. Karnesky, C. K. Sudbrack, and D. N. Seidman, "Best-fit ellipsoids of atom-probe tomographic data to study coalescence of γ' (L12) precipitates in Ni-Al-Cr," *Scr. Mater.*, vol. 57, pp. 353–356, 2007.

[214] T. Müller, K. H. Heinig, and W. Möller, "Size and location control of Si nanocrystals at ion beam synthesis in thin SiO2 films," *Appl. Phys. Lett.*, vol. 81, no. 16, pp. 3049–3051, 2002.

[215] D. Riabinina, C. Durand, J. Margot, M. Chaker, G. A. Botton, and F. Rosei, "Nucleation and growth of Si nanocrystals in an amorphous SiO2 matrix," *Phys. Rev. B*, vol. 74, no. 7, p. 075334, 2006.

[216] M. Perego, C. Bonafos, and M. Fanciulli, "Phosphorus doping of ultra-small silicon nanocrystals," *Nanotechnology*, vol. 21, p. 025602, 2010.

[217] S. Ferrari, M. Perego, and M. Fanciulli, "Quantitative depth profiling at silicon/silicon oxide interfaces by means of Cs+ sputtering in negative mode by ToF-SIMS: A full spectrum approach," *Appl. Surf. Sci.*, vol. 203–204, pp. 52–55, 2003.

[218] P. Pichler, *Point Defects, Impurities Chapter XX*. Wien: Springer, 2004.

[219] W. Press, S. Teukolsky, W. Vetterling, B. Flannery, E. Ziegel, W. Press, B. Flannery, S. Teukolsky, and W. Vetterling, *Numerical Recipes: The Art of Scientific Computing*, vol. 29, no. 4. 1987.

[220] D. Mocatta, G. Cohen, J. Schattner, O. Millo, E. Rabani, and U. Banin, "Heavily Doped Semiconductor Nanocrystal Quantum Dots," *Science (80-.).*, vol. 332, no. 6025, pp. 77–81, 2011.

[221] M. Kuisl and E. Sasse, "Diffusion of Phosphorus in silicon dioxide from a spin-on source," *Thin Solid Films*, vol. 65, no. 3, pp. 373–380, 1980.

[222] K. E. Goodson, M. I. Flik, and D. A. Antoniadis, "Prediction and Measurement of the Thermal Conductivity of Amorphous Dielectric Layers," *J. Heat Transf.*, vol. 116, no. 2, p. 317, 1994.

[223] T. Takahashi, S. Fukatsu, K. M. Itoh, M. Uematsu, A. Fujiwara, H. Kageshima, Y. Takahashi, and K. Shiraishi, "Self-diffusion of Si in thermally grown SiO2 under equilibrium conditions," *J. Appl. Phys.*, vol. 93, no. 6, pp. 3674–3676, 2003.

[224] D. Tsoukalas, C. Tsamis, and J. Stoemenos, "Investigation of silicon interstitial reactions with insulating films using the silicon wafer bonding technique," *Appl. Phys. Lett.*, vol. 63, no. 23, pp. 3167–3169, 1993.

[225] D. J. Norris, A. L. Efros, and S. C. Erwin, "Doped nanocrystals.," *Science (80-.).*, vol. 319, no. 5871, pp. 1776–9, Mar. 2008.

[226] T.-L. Chan, H. Kwak, J.-H. Eom, S. B. Zhang, and J. R. Chelikowsky, "Self-purification in Si nanocrystals: An energetics study," *Phys. Rev. B*, vol. 82, no. 11, p. 115421, Sep. 2010.

[227] S. Iwata and A. Ishizaka, "Electron spectroscopic analysis of the SiO2/Si system and correlation with metal–oxide–semiconductor device characteristics," *J. Appl. Phys.*, vol. 79, no. 9, pp. 6653–6713, 1996.

[228] A. Dane, U. K. Demirok, A. Aydinli, and S. Suzer, "X-ray photoelectron spectroscopic analysis of Si nanoclusters in SiO2 matrix.," *J. Phys. Chem. B*, vol. 110, no. 3, pp. 1137–40, 2006.

[229] M. Perego, G. Seguini, and M. Fanciulli, "XPS and IPE analysis of HfO2 band alignment with high-mobility semiconductors," *Mater. Sci. Semicond. Process.*, vol. 11, no. 5, pp. 221–225, 2008.